Hao Minh Hoang MSc

Fluorescence Quenching Mechanism in Inter- and Intramolecular Photoinduced Electron Transfer Reactions Studied by Time-Resolved Magnetic Field Effects on Exciplexes

DISSERTATION

zur Erlangung des akademischen Grades
Doktor der Naturwissenschaften
eingereicht an der

Technischen Universität Graz

Betreuer
O. Univ.-Prof. Dipl.-Chem. Dr. Günter Grampp
Institut für Physikalische und Theoretische Chemie

Graz, Dezember 2014

EIDESSTATTLICHE ERKLÄRUNG
AFFIDAVIT

Ich erkläre an Eides statt, dass ich die vorliegende Arbeit selbstständig verfasst, andere als die angegebenen Quellen/Hilfsmittel nicht benutzt, und die den benutzten Quellen wörtlich und inhaltlich entnommenen Stellen als solche kenntlich gemacht habe. Das in TUGRAZonline hochgeladene Textdokument ist mit der vorliegenden Dissertation identisch.

I declare that I have authored this thesis independently, that I have not used other than the declared sources/resources, and that I have explicitly indicated all material which has been quoted either literally or by content from the sources used. The text document uploaded to TUGRAZ online is identical to the present doctoral dissertation.

Datum / Date	Unterschrift / Signature

to Hoàng Minh Đăng

to Hoàng Minh Hà

to my parents

CONTENTS

1. Introduction 1

2. Theoretical background 4

2.1. Photo-induced electron transfer 4

2.1.1. Introduction 4

2.1.2. Diffusion-controlled and electron transfer rate constants 5

2.1.3. Energetics of photo-induced electron transfer 7

2.2. Electron transfer theories 12

2.2.1. Classical theory 12

2.2.2. Reorganization energy 15

2.2.3. Adiabatic versus diabatic electron transfer reaction 16

2.2.4. Inverted region 17

2.2.5. Dynamic solvent effects 18

2.3. Magnetic field effects 20

2.3.1. Radical pair mechanism 20

2.3.2. Magnetic field effects in view of the low viscosity approximation 18

2.3.3. Photo-induced electron transfer reaction scheme and time-resolved magnetic field effect of exciplex emission 28

2.4. Theory of experiments 30

2.4.1. Meaning of the lifetime in Time-correlated single photon-counting (TCSPC) technique 30

2.4.2. Example of TCSPC data 32

3. Experimental 35

3.1. Reactants 35

3.1.1. Inter-molecular photo-induced electron transfer systems 35

3.1.1.1. Acceptors (Fluorophores) 35

3.1.1.2. Donors (Quenchers) 35

3.1.2. Intra-molecular photo-induced electron transfer systems 36

3.2. Solvents 39

3.3. Sample preparation 41

3.4. Apparatuses and measurements 41

3.4.1. Absorption and fluorescence spectroscopy 41

3.4.2. Steady-state measurements 42
3.4.3. Time-resolved magnetic field effect measurements 43
4. Simulations 45
5. Results and discussion 51
5.1. Magnetic field effect dependence on the static dielectric constant and chain length 51
5.2. Magnetic field effects on the locally excited fluorophore in intra-molecular photo-induced electron transfer reactions 55
5.3. Exciplex emission bands and Stokes shifts in binary solvent mixtures 57
5.4. The initial quenching products: Exciplexes vs loose ion pairs. Their dependence on solvent dielectric constant and electron transfer driving force in inter-molecular photo-induced electron transfer reactions 60
5.5. The initial quenching products: Exciplexes vs loose ion pairs. Their dependence on solvent dielectric constant and chain length of Mant-*n*-O-2-DMA systems 65
6. Conclusions and outlooks 66
6.1. Conclusions 66
6.2. Outlooks 67
A. Appendix 68
A1. Unit conversion 68
A2. ^{1}H, ^{13}C-NMR and mass spectra of Mant-*n*-O-2-DMA compounds 69
A3. Absorption and fluorescence spectra of inter-systems and Mant-*n*-O-2-DMA compounds 75
A4. Time-resolved magnetic field effects of the exciplexes of inter-systems and Mant-*n*-O-2-DMA compounds 76
A5. Formation of the exciplex dissociation quantum yield, ϕ_d 78

Acronyms 79
References 81

LIST OF FIGURES

2.1. The change of the ionization potential (IP) and electron affinity (EA) of an excited state. The IP is decreased while the EA is released greater, as compared with the ground state 9

2.2. The enthalpy changes for formation of D^+ from D and D* and for formation of A^- from A and A*..... 10

2.3. An energy diagram for photo-induced electron transfer 11

2.4. The progress of the electron transfer process expressed along the reaction coordinate through the multidimensional potential surface of the Reactant state (R) and that of the Product state (P). A and C give the equilibrium nuclear configurations of reactant and product, B is the configuration at the intersection (transition state) of the reactant and product potential energy surfaces 13

2.5. The intersections of the Gibbs energy surfaces of the reactant (R) state, [D...A], and the product (P) state, $[D^+...A^-]$. (a): an electron transfer reaction with the driving force, $-\Delta G^0 = 0$; (b): the normal region where $-\Delta G^0 \leq \lambda$; (c): the condition of maximum rate constant where $-\Delta G^0 = \lambda$ and (d): the inverted region where $-\Delta G^0 > \lambda$..... 14

2.6. The electron transfer is said to be adiabatic (a) and diabatic (b). H_{rp} refers to the electronic coupling energy defined by eq. (2.40)..... 17

2.7. The $\log(k_{ET})$ is a function of the driving force ($-\Delta G^0$) of the ET reaction. At $-\Delta G^0 = \lambda$, the rate constant reaches its maximum value..... 18

2.8. The parabolic curves: The top is a plot of ΔG^* *vs.* $-\Delta G^0$. The energy potential surfaces of the reactant and product shown in the bottom describe the relationships between the driving forces ($-\Delta G^0$) and reorganization energy (λ). The normal region ($-\Delta G^0 < \lambda$) is shown on the left, ΔG^* decreases with decreasing λ or as ΔG^0 becomes more negative. The inverted region ($-\Delta G^0 > \lambda$) is on the right, ΔG^* increases with decreasing or as ΔG^0 becomes more negative. When $\Delta G^* = 0$, the rate is maximum ($-\Delta G^0 = \lambda$) and this case is shown in the center 20

2.9. Vector presentation for the two electron spins of the spin correlated radical ion pair in the presence of an external magnetic field. The precession of the electron spin angular momentum vectors, S_i, about the external magnetic field, B_z, is included 23

2.10. The dependence of the energy difference between singlet and triplet states of the radical ion pair in the absence (a) and presence (b) of an external magnetic field for the case of a negative exchange integral J 24

2.11. Energy levels of singlet and triplet states of a radical ion pair in the absence and presence of an external magnetic field 24

2.12. Vector model of the S-T_0 conversion in a radical pair. The dephasing of the S_1 and S_2 spins which gives rise to the oscillatory S-T_0 transition may be caused by different g-value of the two radicals (Δg-mechanism) or by hyperfine interaction 25

2.13. S-T conversion by Δg mechanism (a) and the dependence of the singlet probability, ρ_S, on an external magnetic field (b) 26

2.14. Vector model of HFI induced S-T_+ transition at zero magnetic field. The electron spin, S_1, and total nuclear spin, I, precess about their resultant and thereby change their projections onto the z-axis 27

2.15. S-T transition by the HFI-mechanism. At high field, the mixing occurs between $|S\rangle$ and $|T_0\rangle$ since the $|T_{+1}\rangle$ and $|T_{-1}\rangle$ states are energetically split due to the Zeeman interaction (here expressed in terms of the angular frequency $\omega = g_i \mu_B \hbar^{-1} B$). At low and zero external magnetic field the smaller energy gap between $|S\rangle$ and $|T_{+1}\rangle$ and $|T_{-1}\rangle$ allows for transitions between singlet and all three triplet states 27

2.16. Schematic representation of the species involved in the process of the magnetic field effect on the exciplex of free acceptor/donor (a) and chain-linked acceptor/donor (b) pairs: photoexcitation (1), exciplex formation (1A), direct formation of the RIP via remote electron transfer (1B), exciplex dissociation into RIP (2), spin evolution by hyperfine interaction (HFI), the singlet RIP re-forms the exciplex (3) and exciplex emission (4). The red and blue arrows denote the fluorescent decay process of either the photo-excited acceptor (magneto-insensitive) or the exciplex (magneto-sensitive) that are observed in the experiment. The magnetically sensitive species are enclosed in the frame. Spin multiplicities are indicated by superscripts 29

2.17. The lifetime of sample is calculated from the slope of a plot of ln I(t) versus time, t.....31
2.18. TCSPC data for 1-bromo-8-[9-(10-methyl)anthryl]octane (MAnt-8-Br) in propyl acetate. The green curve, $L(t_k)$, denotes the instrument response function. The blue curve, $N(t_k)$, gives the measured data and the red curve, $N_c(t_k)$ is called the fitted function. The lifetime of the fluorophore, τ, determined after fitting is 13 ns. The upper panel shows some minor systematic error 33
3.1. Chemical structures of electron acceptors used in time-resolved magnetic field effect studies.....35
3.2. Chemical structures of electron donors used in experiments.....36
3.3. Absorption and fluorescence spectra of Mant-10-O-2-DMA in a mixture of propyl acetate/butyronitrile at ε_s = 12. The fluorescence of the locally excited states and the exciplex are shaded in blue and red, respectively 43
3.4. (Upper panel) Emission time trace of the Mant-16-O-2-DMA exciplex in butyronitrile (ε_s = 24.7) in the absence (gray plot) and presence (red plot) of an external magnetic field monitored with a 550 nm long-pass filter after excitation with a laser pulse at 374 nm. Time-resolved magnetic field effect of the exciplex extracted from the experimental data was shown in lower panel (blue plot).....44
3.5. Scheme of the time-resolved magnetic field effect setup.....45
4.1. The graphic visualization of the exciplex kinetics of inter-systems (left panel) and Mant-*n*-O-2-DMA systems (right panel): ϕ_I gives the probability of the initial singlet radical ion pair (SRIP) formation while $\phi_E = 1-\phi_I$ denotes the probability of the initial exciplex formation. The exciplex dissociates into the singlet radical ion pair with the rate constant, k_d, the SRIP associates into the exciplex with the rate constant, k_a and the radiative/non-radiative exciplex decay to the ground-state (GS) with the rate constant, τ_E^{-1}. LE refers to the locally-excited acceptor.....46
4.2. Calculated singlet probability as a function of time for anthracene/*N*,*N*-diethylaniline at zero field and high field limit. The solid lines denote $p_S(t)$ when the electron self-exchange taken into account with τ_{ex} = 8 ns whereas the dash lines show $p_S(t)$ with neglecting the electron self-exchange.....50
5.1. The magnetic field effects on the inter-systems (a-c) and Mant-*n*-O-2-DMA exciplexes (d-f) determined from TR-MFE using eq. (3.3) (filled circle with error bars) and from steady-state measurements using eq (3.1) (open circles with error bars) in propyl acetate/butyronitrile mixtures with varying the dielectric constant,

ε_s. For intra-acceptor/donor systems, propionitrile (EtCN) and acetonitrile (ACN) are used to extend the range of the solvent polarity 52
5.2. Magnetic field dependence of the exciplex fluorescence of polymethylene-linked compounds (Mant-*n*-O-2-DMA) in neat butyronitrile. The MFEs on systems were obtained in steady-state measurements by detecting the exciplex emission intensity at 550 nm for 60 s, using a spectrometer time constant of 1 s. For each χ_E value, fluorescence intensities were acquired alternating three times between zero and an external magnetic field. The data were analysed to extract the χ_E values by using eq. (3.1) 53
5.3. Graphic visualization of S-T conversion in the zero field and an external field (B_0 < 22 mT) for the linked-system of Mant-6-O-2-DMA 54
5.4. Wavelength-resolved magnetic field effects of the Mant-*n*-O-2-DMA (*n* = 8, 10, 16) systems in butyronitrile. χ_F and χ_E denote the magnetic field effects on the locally-excited fluorophore and the exciplex, respectively 56
5.5. The exciplex emission bands of the studied inter-systems in propyl acetate/butyronitrile mixture at ε_s = 13 57
5.6. Exciplex fluorescence spectra of inter-systems (a-b) and Mant-*n*-O-2-DMA systems (c-d) in neat propyl acetate (PA), butyronitrile (BN) and mixtures of propyl acetate/butyronitrile (PA/BN) at different dielectric constants 59
5.7. Experimental (grey scatter plots) and simulated (red solid lines) time-dependent magnetic field effects. The left column shows data for the anthracene/*N*,*N*-diethylanline system at different ε_s in propyl acetate/butyronitrile mixtures. The right column illustrates for the 9-methylanthracene/*N*,*N*-diethylaniline system 61
5.8. The driving force dependence of the TR-MFEs observed for the systems 9,10-dimethylanthracene/*N*,*N*-dimethylaniline ($-\Delta G^0 \approx 0.28$ eV), 9-methylanthracene/*N*,*N*-diethylaniline ($-\Delta G^0 \approx 0.47$ eV), and anthracene/*N*,*N*-diethylaniline ($-\Delta G^0 \approx 0.58$ eV) at ε_s = 13 . The grey scatter plots denote the experimentally time-resolved magnetic field effect data and their simulations are given in the red solid lines 62
5.9. Solvent polarity dependence of the exciplex lifetimes for the studied inter-systems .. 63
5.10. Solvent dependence of the dissociation rate constants for the studied inter-systems 63

5.11. Solvent dependence of the initial probability of the loose ion pair state, ϕ_I, (upper panel) and the dissociation quantum yield of the exciplex, ϕ_D, (lower panel) of the systems 9,10-dimethylanthracene/*N*,*N*-dimethylaniline (red filled squares), 9-methylanthracene/*N*,*N*-diethylaniline (grey filled triangles), and anthracene/*N*,*N*-diethylaniline (blue filled circles) in propyl acetate/butyronitrile mixtures. The sole purpose of the solid lines is to guide the eye; no physical model is implied 64

A1. ^{1}H, ^{13}C-NMR and mass spectra of Mant-*n*-O-2-DMA compounds 74

A2. Absorption and fluorescence spectra of inter-systems and Mant-*n*-O-2-DMA compounds in propyl acetate/butyronitrile mixture at ε_s = 12 75

A3. From right to left of upper panels: The exciplex emission decays of the DMAnt (2.10^{-5} M)/DMA (0.06 M) and MAnt (2.10^{-5} M)/DEA (0.06 M) in the absence and presence of an external magnetic field, respectively. Lower panels: Time-resolved magnetic field effects of the exciplexes extracted from the experimental data (gray scatters) and simulations (red lines). Propyl acetate/butyronitrile mixture at ε_s = 18 used as a solvent 76

A4. Upper panels of (a) and (b): The exciplex emission decays of the Mant-8-O-2-DMA (2.10^{-5} M) and Mant-10-O-2-DMA (2.10^{-5} M) in the absence and presence of an external magnetic field, respectively. Lower panels of (a) and (b): Time-resolved magnetic field effects of the exciplexes extracted from the experimental data (gray lines). Neat butyronitrile (ε_s = 24.7) used as a solvent 77

LIST OF TABLES

3.1. Physical parameters of the used acceptors and donors: The 0,0-energy E_{00}, lifetime of acceptors (A), τ_A, and donors (D), τ_D, reduction and oxidation potentials, $\boldsymbol{E_{1/2}^{red}}$ and $\boldsymbol{E_{1/2}^{ox}}$, respectively. The free energy difference of electron transfer $-\Delta G^0$ was calculated at ε_s = 13 in propyl acetate/butyronitrile mixture, using the Rehm-Weller equation with Born correction assuming an inter-particle distance of 6.5 Å and an ion radius of 3.25 Å. 37

3.2. Chemicals were used in the synthetic steps of the polymethylene-linked acceptor/donor systems. Abbreviations: Mant: 9-methylanthracene, 1,6-DBH: 1,6-dibromohexane, 1,8-DBO: 1,8-dibromooctane, 1,10-DBD: 1,10-dibromodecane, 1,16-HDDO: 1,16-hexadecanediol, DMAPE: 2-[(4-dimethylamino)phenyl]ethanol. Supplier and purification are indicated 39

3.3. Macroscopic solvent properties are given at 25 ^{0}C: density (ρ), dielectric constant (ε_s), dynamic viscosity (η), refractive index (n). Additionally the solvent supplier and the purification methods are given. Abbreviations: PA: propyl acetate, BN: butyronitrile, ACN: acetonitrile, EtCN: propionitrile 40

3.4. The dielectric constant mixture ($\varepsilon_{s,\ mix}$), mole fraction of butyronitrile (x_{BN}), viscosity (η), refractive index (n) and Pekar factor ($\gamma = (1/n^2 - 1/\varepsilon_s)$ of PA/BN mixtures 41

4.1. Used hyperfine coupling constants, a_-^H, for anthracene$^{-\cdot}$ 48

4.2. Used hyperfine coupling constants, $\left|a_-^H\right|$, for 9-methylanthracene$^{-\cdot}$ 48

4.3. Used hyperfine coupling constants, a_-^H, for 9,10-dimethylanthracene$^{-\cdot}$ 48

4.4. Used hyperfine coupling constants, a_+^H, for the radical cation of *N*,*N*-diethylaninline$^{+\cdot}$. No experimental values are available, the values below have been calculated using DFT (UB3LYB/EPRII) 48

4.5. Used hyperfine coupling constants, a_+^H, for *N*,*N*-dimethylaniline$^{+\cdot}$. No experimental values are available, the values below have been calculated using DFT (UB3LYB/EPRII) 48

5.1. Some parameters of the studied A/D pairs at ε_s = 13 in propyl acetate/butyronitrile mixture. E_{00} is the 0-0 transition energy of acceptor; $-\Delta G_{Ex}$ refers to the free energy of exciplex formation; $-\Delta G_R$ gives the free energy of back-electron transfer; λ_{max} denotes the maximum wavelength of the exciplex emission band. 58

ABSTRACT

This work is an approach based on the time-resolved magnetic field effect (TR-MFE) of the delayed exciplex luminescence to distinguish the initial quenching products in fluorescence quenching reactions via inter-and intra-molecular photo-induced electron transfer (ET) between an electron excited acceptor (A*) and an electron donor (D). TR-MFEs based on the Time-Correlated Single Photon-Counting (TCSPC) method of inter-and intra-acceptor/donor exciplex emissions are measured in micro-homogeneous binary solvent mixtures of propyl acetate/butyronitrile by varying the static dielectric constant, ε_s, in a range from 6 to 24.7. For free acceptor/donor pairs, the study focuses on the effects of the driving force of ET, $-\Delta G^0$, and the solvent polarity, ε_s. In order to change $-\Delta G^0$, the different free acceptor/donor pairs are used with the $-\Delta G^0$ varied in the range from 0.28 to 0.58 eV. Chain-linked acceptor/donor pairs have been synthesized with varying the chain length to clarify the mechanism of fluorescence quenching via intra-molecular photo-induced ET. All experimental data have been analysed by using a model in which the reversibility of the exciplex and radical ion pair (RIP) is taken into account.

ZUSAMMENFASSUNG

Im Ramen dieser Arbeit wurden versucht die primären Quenching-Produkte von Fluoreszenz-Quenching Reaktionen auf Basis eines inter- oder intramoleklaren photoinduzierten Elektronentransfers zwischen einem angeregten Elektronenakzeptor (A*) und einem Elektronendonor (D) bestimmt. Dafür wurde mittels Time-Correlated-Single-Photon-Counting (TCSPC) der zeitaufgelöste Magnet-Feld-Effekt (TR-MFE) der Lumineszenz des Exiplex untersucht. Im Zentrum steht der Einfluss der Polarität des Lösungsmittel, repräsentiert durch ε_s. Die Polarität des Lösungsmittels wurde mittels micro-heterogenen binären Lösungsgemischen aus Propylacetat/Butyronitril variiert, wobei ein Bereich von 6–24,7 für ε_s abgedeckt wurde. Als freie Akzeptor/Donor Paare wurde verschiedene Systeme gewählt, sodass zusätzlich der Einfluss der Triebkraft der Reaktion $-\Delta G^0$ untersucht werden konnte. Es wurde ein Bereich von 0,28-0,58 eV abgedeckt. Um intramolektularen photoinduzierten Elektronentransfer zu beobachten, wurden kovalent verbundene Akzeptor/Donor Systeme synthetisiert, wobei die Länge der Verbrückung variiert wurde, um den Einfluss dieser zu untersuchen. Alle Daten wurden mit einem Model analysiert, welches Exiplex und Radikal Ionen Paar (RIP) als reversibel animmt.

ACKNOWLEDGEMENTS

I would like to thank many people for their patience and contribution to my thesis. I would not finish without their help. The length of these acknowledgements is not enough to express my gratitude and appreciation to them.

First, I'm deeply indebted to Dr. DANIEL KATTNIG who was, although not officially, my second advisor. I'm astonished at his patience. He taught me everything concerning magnetic field effect theory. With wide knowledge of literature, chemistry, numerical methods and capability of explaining complex theory, he could always give detailed answers for all my questions. Without his guidance and help to analyse the experimental data, I would not definitely accomplish my dissertation. DANIEL! Thank you so much, my gratitude to you will last forever.

I'm thankful to Prof. Dr. GÜNTER GRAMPP, my supervisor, who gave me the opportunity to come to Austria. From whom, I learnt much about electron transfer and photochemistry theories. His enthusiasm and the way of thinking are stimulating, which makes me more confident in scientific discussion.

It is a pleasure to thank Assoc. Prof. Dr. Stephan Landgraf, who was willing to help me adjusting and fixing the Single Photon Counting apparatus. I have gained the knowledge on fast and modern kinetics from his lectures. Thanks for personal communication in magnetic field effect results.

Many thanks to Dr. Kenneth Rasmussen, Dr. Boryana Mladenova Katting, who were abundantly helpful in science for my work. Furthermore, you are my good friends for sharing and helping.

I would like to thank all members of the Institute of Physical and Theoretical Chemistry, Graz University of Technology. Special thanks to Eisenkölbl, Freißmuth, Ines, Hofmeister and Lang. Thank you for solving apparatus problems and keeping things running.

I wish to thank my friends and colleagues at Prof. Grampp's group. They gave me a great atmosphere. Thanks for all the emotional support and entertainment.

Financial supports given by Vietnam International Education Development (VIED) and Austrian Science Foundation, FWF-Project P 21518-N19 for my study are acknowledged.

Last but not at all least, Vân, Đăng and my family! Their supports help me to overcome difficulties. Thank you so much for their endless love.

1. INTRODUCTION

Photo-induced electron transfer (ET) reactions have been extensively studied for many years. This surge is motivated by the fact that ET is one the most fundamental, omnipresent elementary reactions in chemistry, physics, and biochemistry [1-4]. However, questions about the microscopic details of the quenching still remain, in particular in solvents of low permittivity. In these media a photo-excited acceptor (A*) or a fluorophore (F*) diffusively approaching a suitable electron donor (D) or a quencher (Q); or vice-versa, i.e. D could be photo-excited, can be deactivated in a charge separation reaction either by forming a solvent-separated, loose ion pair (LIP) or by the formation of an excited-state charge-transfer complex (exciplex), which in the absence of intrinsic fluorescence emission is also referred to as a contact ion pair (CIP). While the LIP is formed at distances longer than or equal to the contact distance of A* and D, the exciplex formation typically involves tight stacking and a well-defined relative orientation [5-9], which can be inferred from the correlated motion of the quencher and the fluorophore in the complex [10]. The solvent permittivity strongly affects the quenching mechanism. In polar solvents, quenching occurs predominantly by distant ET, i.e. by an ET process yielding directly the LIP. However, in non-polar solvents (i.e., low permittivity), exciplex fluorescence is often observed, suggesting the contribution of the exciplex formation in the ET deactivation (the exciplexes can also result from secondary recombination of initially formed ion-pairs; this question is addressed in the result discussion section) [11-18]. Only a few exceptions to this empirical rule are known in the literature. E.g., a CIP is dominantly formed by diffusive ET quenching of 9,10-dicyanoanthracene (DCA) by durene even in acetonitrile (quantum yield: 0.8) [19].

The primary quenching products are strongly affected by energetic parameters. The direct formation of free ions, partly at distances exceeding the contact distance, is expected to be significant for systems with larger driving force [10, 14, 20, 21]. The experimental results for the DCA/durene system in acetonitrile indicated that with a free energy change of ion formation of $-\Delta G^0 = 0.25$ eV, exciplexes are formed efficiently in the bimolecular quenching reaction from AD* state, whereas in the case of 2,6,9,10-tetracyanoanthracene (TCA)/pentamethylbenzene (PMB) with $-\Delta G^0 = 0.75$ eV, an exciplex could not be detected [22, 23]. Exciplex fluorescence was observed for several systems in acetonitrile when

the $-\Delta G^0$ is in the range from -0.28 to +0.20 eV [7, 8]. Yet, full electron transfer is observed for the vast majority of donor-acceptor system in acetonitrile [7, 8, 13, 23, 24].

In general, exciplexes can be observed by their emission, which are, in the most favourable cases, spectrally well separated from the locally excited fluorescence [11, 19, 23]. Furthermore, under suitable conditions, this exciplex emission is sensitive to an external magnetic field [25-36].

In the literature dealing with MFE it is generally assumed that a LIP is formed initially and re-combine irreversibly to an exciplex [32, 37-38]. Or the exciplex is an initial quenching product even in polar environment [34, 39]. Unfortunately, no details about the mechanism of fluorescence quenching reaction are known. In order to clarify the quenching mechanism via ET, a model has been introduced in ref. 36. There, by systematically varying the bulk dielectric constant, ε_S, of micro-homogeneous binary solvents and using the model with the reversibility between the exciplex and the LIP to simulate the experimental data. The initial states of quenching, i.e., LIP (or radical ion pair-RIP) and exciplex based on the TR-MFEs of the exciplex, have been discriminated.

All studies mentioned above depict the picture of the mechanism of fluorescence quenching reaction via inter-molecular ET by bimolecular process. Intra-molecular photo-induced ET in which acceptor/donor pair attached via a flexible chain is more complicated since, this process relates to the dynamics of chain conformations. The competition between distant ET and exciplex formation is dependent on solvent characteristics such as dielectric constant and viscosity as well as structural features of the acceptor-spacer-donor system [40-43]. MFE studies on intra-molecular exciplex fluorescence have been investigated. However, most of these studies are generally mixing. The experimental data were discussed under the assumption that the singlet radical ion pair (SRIP) is an initial quenching product and the singlet exciplex (SE) is generated from SRIP recombination [33, 44-45] or focusing on the dependence of the MFE on chain length [45].

This thesis contributes to a deeper and better understanding of the fluorescence quenching mechanism via inter- and intra-molecular photo-induced ET. To investigate the effect of the ET driving force ($-\Delta G^0$) on the initial quenching products, the $-\Delta G^0$ was varied in the range from 0.28 to 0.58 eV by using different free acceptor/donor pairs. The polymethylene-linked 9-methylanthracene and *N*,*N*-dimethylaniline were synthesized to distinguish the primary quenching products via intra-molecular photo-induced ET. Time-resolved magnetic field effects of the exciplexes based on the time-correlated single photon-counting (TCSPC) method have been measured in micro-homogeneous binary solvent of propyl

acetate/butyronitrile mixtures with the dielectric constant, ε_s, varying from 6 to 24.7. The experimental data have been simulated by the model in which the exciplex dissociation is taken into account [36].

This thesis is organized as follows:

- Theoretical considerations including theories of photo-induced electron transfer (PET) reaction, magnetic field effects (MFE) of the exciplexes (time-resolved and steady-state foundations), and Time-Correlated Single Photon Counting (TCSPC) technique are summarized in chapter 2.
- Time-resolved MFE measurements by using TCSPC technique, steady-state measurements, the simulation model and the details in the solvent and sample preparations are presented in chapter 3 and 4.
- Chapter 5 presents the experimental data and their analysis.
- Finally, some conclusions and outlooks to possible future work are presented in chapter 6.

2. THEORETICAL BACKGROUND

2.1. Photo-induced electron transfer

2.1.1. Introduction

The relation between the rate constant of a chemical reaction, the activation energy and thermal energy was introduced in 1889 by Svante Arrhenius [46] by an equation:

$$k = A\exp(\frac{-E_a}{RT}) \tag{2.1}$$

Where R is the gas constant, A is the pre-exponential factor or the frequency factor, and E_a refers to the activation energy of the reaction. Both A and E_a are temperature dependent. The reaction rate depends on the driving force and the activation energy. A transition state was involved in Arrhenius equation. The aim of the transition state theory is to determine the principal features governing the magnitude of a rate constant in terms of a model of the steps that take place during the reaction. There are several approaches to the determination and calculation, the simplest approach was introduced by Erying [47-49]. The final product was generated via the formation of an activated complex, $C^{\neq}$, in a rapid pre-equilibrium with A, B reactants.

$$A + B \rightleftharpoons C^{\neq} \rightarrow \text{Product} \tag{2.2}$$

The mostly used theory dealing with electron transfer (ET) is developed by Marcus [1-4]. The detailed Marcus theory and the important expression will consider in the next section. Marcus theory is used for the ET reaction between an excited electron acceptor (A*) and an electron donor (D), called as the photo-induced electron transfer (PET) reaction. The ET process of the acceptor/donor pair can proceed in three steps

Formation of the precursor complex: In the first step, the reactants diffusively approach each other to form a precursor complex (the rate of formation of precursor complex usually approaches diffusion-controlled limit).

$$A^* + D \underset{-k_{diff}}{\overset{k_{diff}}{\rightleftharpoons}} [A^*...D] \tag{2.3}$$

Formation of the successor complex: In the second step, the electron transfer takes place at transition state to generate a successor complex $[A^-\ldots D^+]^*$ after the precursor complex $[A^*\ldots D]$ underwent reorganization towards a transition state.

$$[A^{*}...D] \underset{k_{-ET}}{\overset{k_{ET}}{\rightleftharpoons}} [A^{-}...D^{+}]^{*} \tag{2.4}$$

Formation of free ions: In the final step, the successor complex dissociates to form the free ions A^- and D^+.

$$[A^{-}...D^{+}]^{*} \underset{k_{-d}}{\overset{k_{d}}{\rightleftharpoons}} A^{-} + D^{+} \tag{2.5}$$

A steady-state treatment of equations (2.3) to (2.5) leads to the following kinetic expression of the observed bimolecular electron transfer rate constant.

$$\frac{1}{k_q} = \frac{1}{k_{diff}} + \frac{1}{K_{eq} k_{ET}} \left[1 + \frac{k_{-ET}}{k_d} \right] \tag{2.6}$$

Where $K_{eq} = \frac{k_{diff}}{k_{-diff}}$. If $k_d \gg k_{-ET}$

$$\frac{1}{k_q} = \frac{1}{k_{diff}} + \frac{1}{K_{eq} k_{ET}} = \frac{1}{k_{diff}} \left[1 + \frac{k_{-diff}}{k_{ET}} \right] \tag{2.7}$$

If the electron transfer rate is slow as compared to k_{-diff} ($k_{ET} \ll k_{-diff}$) then $k_q \approx K_{eq} k_{ET}$. When $k_{ET} \gg k_{-diff}$ we see that $k_q \approx k_{diff}$ and the rate of product formation is controlled by diffusion of A* and D in solution.

2.1.2. Diffusion-controlled and electron transfer rate constants

The analysis is started with Scheme (2.8) with an assumption that the excited species is an electron donor:

$$A^{*} + D \underset{k_{-diff}}{\overset{k_{diff}}{\rightleftharpoons}} [A^{*}...D] \underset{k_{-ET}}{\overset{k_{ET}}{\rightleftharpoons}} [A^{-}...D^{+}]^{*} \xrightarrow{k_d} A^{-} + D^{+} \tag{2.8}$$

k_{diff} is the diffusion rate constant between reactants, k_{-diff} denotes the rate of separation of the encounter complex, $[A^{*}...D]$, k_{ET} is the first-order rate constant of electron transfer step. The reverse step is designated by the rate constant k_{-ET}. The encounter complex lifetime is about 10^{-9} to 10^{-10}s. During this time two molecules may undergo numerous collisions before they react or separate from the encounter complex into the bulk of solvent molecules. In PET, an encounter complex can be visualized as an ensemble consisting of a sensitizer and quencher surrounded by solvents molecules (solvent shell). The sensitizer and quencher are said to be contained within a solvent cage. For the spherical reactants within the solvent cage, the center-to-center distance (d_{cc}) is usually approximated around 7 Å. After the encounter

complex is formed, the sensitizer and quencher may undergo reaction or eventually escape from the cage. If reaction takes place within the solvent cage, the ET products may revert back to starting reactants, undergo irreversible chemical reaction, or leave the solvent cage by ion dissociation. The rate of diffusion of two spherical reactants to an encounter distance (assuming that d_{cc} equals the sum of the reactant molecules' radii) can be calculated from eq. (2.9).

$$k_{diff} = 4\pi D_{AD} d_{cc} \tag{2.9}$$

Where D_{AD} is the combined diffusion constant for approach of A and D. d_{cc} is the center-to-center distance. It suggests that the diffusion rate constant is the combined diffusion constant and separation distance dependent. The Stokes-Einstein equation was used to calculate the diffusion constant for one reactant.

$$D = \frac{k_B T}{6\pi\eta r} \tag{2.10}$$

Where k_B is the Boltzmann constant, η is the solution viscosity of the solution, and r is the radius of the reactant. Introduction of eq. (2.10) into eq. (2.9) yields.

$$k_{diff} = \frac{8k_B T}{3\eta} \tag{2.11}$$

Finally, using molar unit in eq. (2.11) gives a well-known version of the Smoluchowski equation.

$$k_{diff} = \frac{8RT}{3000\eta} \tag{2.12}$$

For the fast ET reaction, i.e., reaction occurs at every collision after the reactants have already been at encounter distance by diffusion. Thus $k_{ET} \gg k_{-diff}$ and $k_q \approx k_{diff}$ (where k_q is the rate of quenching). Such reactions are diffusion controlled. According to eq. (2.12), a diffusion controlled reaction (a fast quenching process) should depend on the temperature and the viscosity of the solvent.

The bimolecular rate constant for the activated rate of electron transfer is defined as k_a.

$$k_a = K_{eq} k_{ET} \tag{2.13}$$

From eqs. (2.13) and (2.7) gives.

$$\frac{1}{k_q} = \frac{1}{k_{diff}} + \frac{1}{k_a} \tag{2.14}$$

k_q is determined from Stern-Volmer measurements and k_{diff} can be calculated from eq. (2.12). From these two values, k_a can easily be determined from eq. (2.14). In addition, the equilibrium constant for the formation of the precursor complex, K_{eq} can be expressed by Norman Sutin [50].

$$K_A = 4\pi N_A d^2 \delta d \exp\left(\frac{-w_r}{RT}\right) \tag{2.15}$$

With the Coulombic work term given by

$$w_r = \frac{z_A z_D e_0^2 N_A}{4\pi\varepsilon_0\varepsilon_s d(1+\beta d\sqrt{I})} \text{ with } \beta = \sqrt{\frac{2N_A e_0^2}{\varepsilon_0\varepsilon_s k_B T}}$$

Where N_A is the Avogadro constant, $d = r_A + r_b$ is the contact radius of the acceptor and donor molecules, r_A and r_b are the mean molecular radii of acceptor and donor, δd is reaction zone thickness of roughly 0.8 Å, e_0 id the elementary charge, I is the ionic strength of the solution, z_A and z_D are the charges of the acceptor and donor molecules, ε_0 is the vacuum permittivity (or electric constant) and ε_s is the static dielectric constant of the solvent.

With knowledge of k_a, we can deduce a value for k_{ET} from eq. (2.13).

If the radii and charges of the acceptor and the donor are different, the diffusion rate constant is determined from the Debye equation [51].

$$k_{diff} = 4\pi(D_A + D_D)d_{cc}\left[\frac{\frac{z_A z_D e_0^2}{4\pi\varepsilon_0\varepsilon_s d_{cc} k_B T}}{\left[\exp\left(\frac{z_A z_D e_0^2}{4\pi\varepsilon_0\varepsilon_s d_{cc} k_B T}\right)\right]-1}\right]N_A \tag{2.16}$$

$$\text{and } D_A + D_D = \frac{k_B T}{6\pi\eta}\left(\frac{1}{r_A}+\frac{1}{r_D}\right) \tag{2.17}$$

2.1.3. Energetics of photo-induced electron transfer

Photo-induced electron transfer was discussed in many literatures [52-55]. PET is a process where an electron acceptor or an electron donor absorbs light to become an excited state. Due to light absorption, some excited states act as strong electron acceptors and/or electron donors

depending on thermodynamic factors. The energetics is a crucial factor that determines the feasibility of PET.

Ionization potentials and electron affinities of the excited state

The excited species containing a higher energy, have an important role on the donating or accepting ability. Figure 2.1 shows the feasibility of the electron donating and electron accepting processes of a ground state and an excited state. If the bound electron is expelled from the orbital to an orbital within the continuum (E_∞), the energy change associated with this ejection is known as the ionization potential or IP which is the difference between the orbital energy at infinite distances (E_∞) and the energy of the lowest orbital (E_1): ($IP = E_\infty - E_1$). The magnitude of IP is the energy required to ionize an atom or molecule (to remove an electron from a molecule). The donating species is called an electron donor (D) ($D \rightarrow D^+ + e^- + IP_D$). In the excited state, the excited electron placed a position in which the energy required to eject it to the infinite distance is easier than the ground electron, i.e., the IP of an excited state is less than the one of the ground state: $IP_{D^*} = IP_D - E_{00}$ where E_{00} is *0-0* transition energy of donor. The energy released when the electron moves from the infinite distance to a vacant orbital near nucleus is called the electron affinity or EA ($A + e^- \rightarrow A^- - EA_A$). The accepting species is called an electron acceptor. In the excited state, there is a vacant orbital which generated by light absorption, lying in lower energy level. Hence, the excited state accepts an electron ($A^* + e^- \rightarrow A^- - EA_{A^*}$), the electron affinity (EA_{A^*}) of excited state is greater than the one of the ground state EA_A, ($EA_{A^*} = EA_A + E_{00}$). This model explains that the ability of excited states act as better electron donor or acceptor.

Redox potentials of the excited state

The change enthalpy of the ionization of an electron donor in ground and excited states is shown in the Figure 2.2. $\Delta H_{D \rightarrow D^+}$ is positive quantity since it refers to an endothermic process. While $\Delta H_{D^* \rightarrow D^+}$ is more negative than $\Delta H_{D \rightarrow D^+}$ by an amount equal to the energy of the excited state ($-\Delta H_{D^* \rightarrow D^+} + \Delta H_{D \rightarrow D^+} = E_{00}$). The free energy change accompanying a chemical process is $\Delta G = \Delta H - T\Delta S$. Where ΔG is the free energy change between the thermodynamic reactant and product states, ΔS is the entropy of reaction and T is the absolute temperature. The enthalpy change will be:

$$-\Delta G_{D^* \rightarrow D^+} - T\Delta S_{D^* \rightarrow D^+} + \Delta G_{D \rightarrow D^+} + T\Delta S_{D \rightarrow D^+} = E_{00} \quad (2.18)$$

If assume that the structure of D and D^+ and of D* and D^+ are approximately the same, the change in entropy is negligible. Thus, the free energy difference is $\Delta G = \Delta H$ and $\Delta G_{D^* \to D^+} = \Delta G_{D \to D^+} - E_{00}$.

The same arguments can be applied to evaluate the free energy changes for reduction of an acceptor and its excited state with $\Delta G_{A^* \to A^-} = \Delta G_{A \to A^-} - E_{00}$. The potential of a half reaction, E_{redox}, is related to the free energy change by:

$$\Delta G = -nFE_{redox} \tag{2.19}$$

Where n gives the number of electron transfer, and F is a unit known as the Faraday constant. Since E_{redox} is sensitive to the direction of the reaction, E_{redox} is sign dependent. A positive E_{redox} implies an exothermic, spontaneous reaction and a negative value suggest an endothermic process. In practice, when using E_{redox} whether it is oxidation or reduction, is usually written as a reduction process.

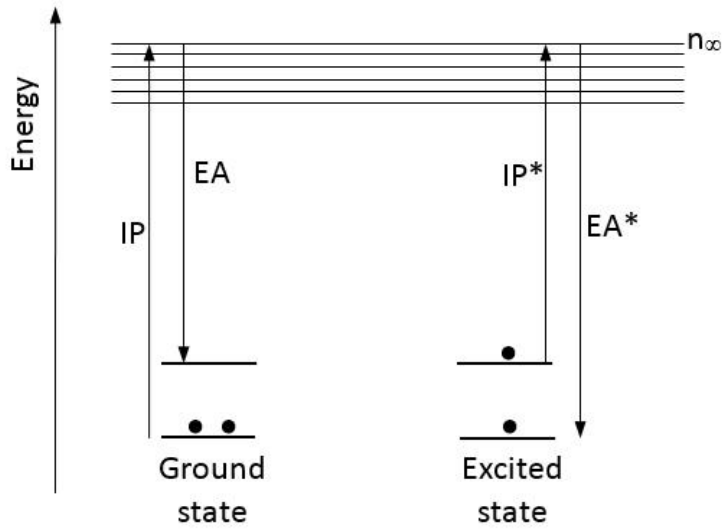

Figure 2.1. The change of the ionization potential (IP) and electron affinity (EA) of an excited state. The IP is decreased while the EA is released greater, as compared with the ground state.

By convention $E^0(D^+ / D) = -E_{D \to D^+}$ and $E^0(D^+ / D^*) = -E_{D^* \to D^+}$, we write

$$E^0(D^+ / D^*) = E^0(D^+ / D) - E_{00} \tag{2.20}$$

According to eq. (2.20), the magnitude of $E^0(D^+/D^*)$ is now smaller than $E^0(D^+/D)$, This implies that the excited state is a better electron donor than the ground state. A similar treatment can be applied to the reduction of A.

$$E^0(A^*/A^-) = E^0(A/A^-) + E_{00} \tag{2.21}$$

In this case, since its redox potential is more positive, the excited state is a better electron acceptor than its ground state.

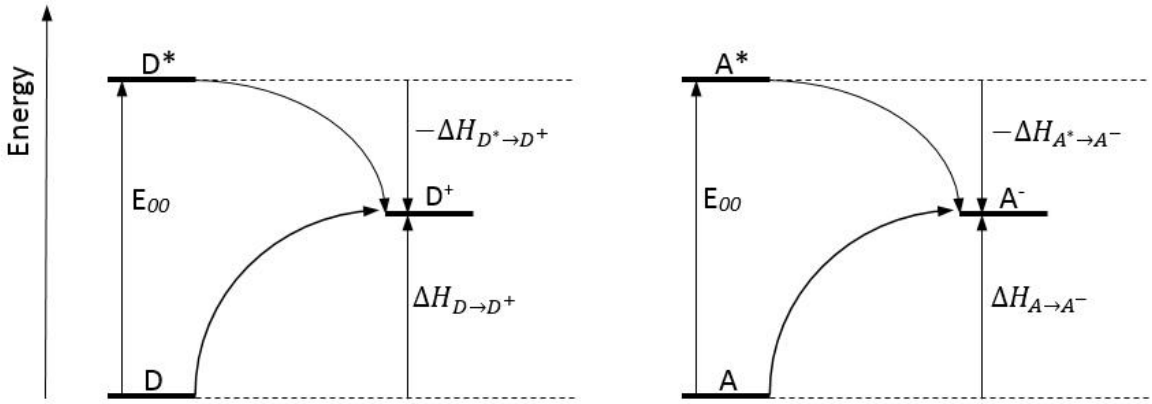

Figure 2.2. The enthalpy changes for formation of D^+ from D and D* and for formation of A^- from A and A*.

Rehm-Weller equation

Having established thermodynamic relationships for deriving the redox potentials of reductions and oxidations of excited state donor and acceptor molecules. A useful expression for calculating the free energy change accompanying excited state electron transfer should be derived. In Figure 2.3 depicts a thermodynamically uphill pathway involving D and A and a downhill pathway from D* and A.

The overall free energy change for the uphill process is equal to the sum of the free energy changes for oxidation of the donor and reduction of the acceptor.

$$\Delta G_{el} = \Delta G_{D\to D^+} + \Delta G_{A\to A^-} \tag{2.22}$$

Where ΔG_{el} gives the standard free energy change. Using eqs. (2.19) and (2.22) gives

$$\Delta G_{el} = nF(-E_{D\to D^+} - E_{A\to A^-}) \tag{2.23}$$

Using redox potentials.

$$\Delta G_{el}(eV) = nF[E^0(D^+/D) - E^0(A/A^-)] \tag{2.24}$$

A similar treatment for the ET between an excited donor and ground state acceptor, the free energy change for this process is given by:

$$\Delta G_{el}(eV) = nF[E^0(D^+/D^*) - E^0(A/A^-)] \tag{2.25}$$

Substitution of eq. (2.20) into eq. (2.25) gives

$$\Delta G_{el}(eV) = nF[E^0(D^+/D) - E^0(A/A^-) - \Delta G_{00}] \quad (2.26)$$

Where ΔG_{00} (eV) is the free energy corresponding to E_{00}. For most one electron transfers, $nF \sim 1$, so that we can write

$$\Delta G_{el}(eV) = E^0(D^+/D) - E^0(A/A^-) - \Delta G_{00} \quad (2.27)$$

If we express the excited state in kilocalories per mole and redox potentials in volts, eq. (2.27) becomes, for $n = 1$.

$$\Delta G_{el}(kcal/mol) = 23.06[E^0(D^+/D) - E^0(A/A^-) - \Delta G_{00}] \quad (2.28)$$

If an electron acceptor is in an excited state (A*) and ET occurs between A* and D. A similar treatment applied to this process also leads to eq. (2.28).

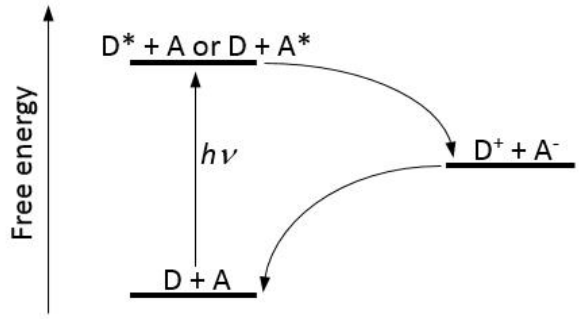

Figure 2.3. An energy diagram for photo-induced electron transfer.

The above expressions applied to the ET process between neutral acceptor and neutral donor. The products are two charge species D^+ and A^-. When these ions formed, attractive Coulombic forces will draw the two ions closer together and result in a release of energy. This attraction is given by a work term, w_p, derived from Coulomb's law.

$$w_p(kcal/mol) = \frac{(z_{D^+} z_{A^-})e^2}{d_{cc}\varepsilon_s} = \frac{332(z_{D^+} z_{A^-})}{d_{cc}\varepsilon_s} \quad (2.29)$$

Where z_{D^+} and z_{A^-} are the charges on the molecules, ε_s is the static dielectric constant of the solvent, and d_{cc} is the center-to-center separation distance (Å) between the two ions. Combining eqs. (2.28) and (2.29) yields:

$$\Delta G_{el}(kcal/mol) = 23.06[E^0(D^+/D) - E^0(A/A^-)] - w_p - \Delta G_{00} \quad (2.30)$$

Equation (2.30) is called the Rehm-Weller equation [55]. According to the work term in Eq. (2.30), the presence of electrostatic interaction between two ions should influence the free energy change accompanying electron transfer. At the heart of electron transfer

photochemistry eq. (2.30) states concisely the fundamental thermodynamic condition for spontaneous electron transfer between neutral reactants: $\Delta G_{el} < 0$.

If the reactants are charged species, another form of eq. (2.30) can be employed. Eq. (2.31) includes a Coulombic term (w_r = - w_p) that expresses the work needed to bring charged reactants to a sufficiently close distance (this work will be negative if the charges are opposite sign, and positive for charges of same sign)

$$\Delta G_{el}(kcal/mol) = 23.06[E^0(D^+/D) - E^0(A/A^-)] - w_p + w_r - \Delta G_{00} \quad (2.31)$$

2.2. Electron transfer theories

2.2.1. Classical theory

The potential energy of the initial reactant state or precursor complex [D· · ·A] is a function of many nuclear coordinates, including reactant and solvent coordinates. This dependence results in a multidimensional potential energy surface. The similar potential surface is also applied for the product state or successor complex [D^+ · · ·A^-]. In the transition-state theory a reaction coordinate introduced to a one-dimensional profile. Figure 2.4 depicts for reactions with the free energy change, $\Delta G^0 = 0$. At the position where ET takes place, the reactant state must normally distort along the reaction coordinates from its equilibrium precursor position A to position of the transition state B, the transition. ET occurred at this position, and the resulting product state then relax to its equilibrium successor position C. This whole model relies on the Born-Oppenheimer approximation.

If the multidimensional potential surface is presented in a Gibbs (free) energy space, the Gibbs energy profiles along the reaction coordinates can be well approximated as parabolas. For purpose of presenting the theory, we consider first a ground-state reaction where $\Delta G^0 < 0$ (although this condition is no compulsory for the description of the theory). According to classical transition state theory, the first order rate constant k_{ET} is given by:

$$k_{ET} = \kappa_{ET} \nu_n \exp\left(\frac{-\Delta G^*}{k_B T}\right) \quad (2.32)$$

Where ν_n is the frequency of passage (nuclear motion) through the transition state along the reaction coordinates [D· · ·A]$^{\neq}$ ($\nu_n \sim 10^{13} s^{-1}$), ΔG^* is the Gibbs energy of activation for the ET process, κ_{ET} is the electronic factor. In classical treatment κ_{ET} is usually taken to be unity, k_B is the Boltzmann constant and T is the temperature. Figure 2.5 depicts the parabolic Gibbs energy surfaces as a function of reaction coordinates for a variety of conditions. In Marcus

theory, the curvature of the reactant and the product surfaces is assumed to be the same. The important parameters in the diagram are λ, the reorganization energy defined as the change in Gibbs energy if the reactant state [D· · ·A] was to distort to the equilibrium configuration of the product state [D^+ · · ·A^-] without transfer of the electron; ΔG^*, the Gibbs energy of activation for forward ET, and ΔG^0, the difference in Gibbs energy (the driving force) between the equilibrium configuration of the product and the reactant states.

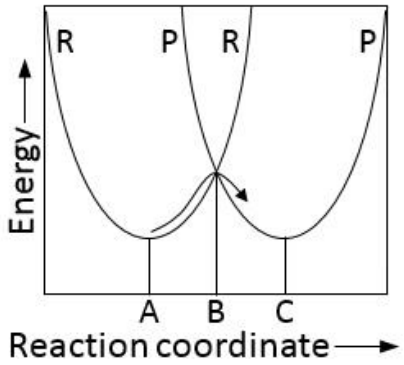

Figure 2.4. The progress of the electron transfer process expressed along the reaction coordinate through the multidimensional potential surface of the Reactant state (R) and that of the Product state (P). A and C give the equilibrium nuclear configurations of reactant and product, B is the configuration at the intersection (transition state) of the reactant and product potential energy surfaces.

Figure 2.5-a shows the ET reaction in which the difference in Gibbs energy, $-\Delta G^0 = 0$. Here the two parabolic surfaces are identical, except that the product surface is displaced along the reaction coordinate with respect to reactant surface. The Gibbs energy of activation is required, even though $\Delta G^0 = 0$. As an ET proceeds to interconvert these species, a geometry distortion of the reactants and solvents occurs, producing a structure similar to that encountered where the curves cross. Symmetry restrictions usually prohibit attaining the precise geometry described at the point of curve crossing, but molecular distortions occur to approximate the geometry described at that point where the curves cross. At this point, a reactant is converted to product without having to directly cross from one surface to another. This reaction trajectory involves what is known as avoided crossing. It follows from the properties of parabolas that for a self-exchange reaction or other reaction of zero ΔG^0, ignoring the effect of any work terms.

$$\Delta G^* = \frac{\lambda}{4} \tag{2.33}$$

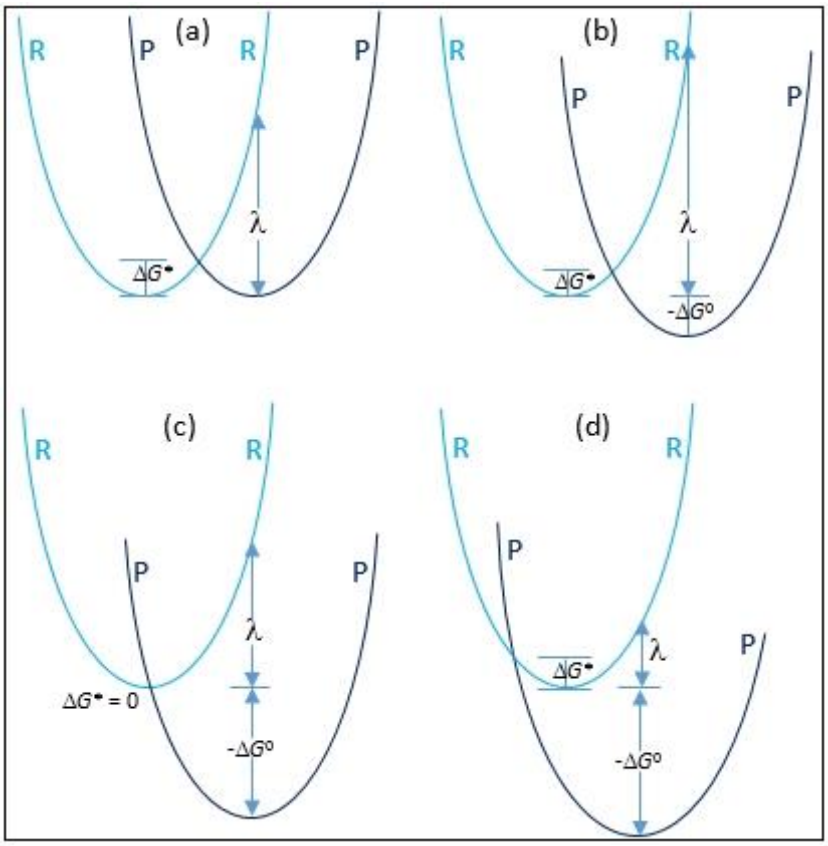

Figure 2.5. The intersections of the Gibbs energy surfaces of the reactant (R) state, [D...A], and the product (P) state, [D^+...A^-]. (a): an electron transfer reaction with the driving force, $-\Delta G^0 = 0$; (b): the normal region where $-\Delta G^0 \leq \lambda$; (c): the condition of maximum rate constant where $-\Delta G^0 = \lambda$ and (d): the inverted region where $-\Delta G^0 > \lambda$.

Figure 2.5-b depicts the ET reaction where $-\Delta G^0 \neq 0$. The parabolic surface of the product, [$D^+ \cdot\cdot\cdot A^-$] shifts vertically by ΔG^0 with respect to [D$\cdot\cdot\cdot$A] one. The activation energy for the ET process is given by:

$$\Delta G^* = \frac{(\lambda + \Delta G^0)^2}{4\lambda} \tag{2.34}$$

Inserting eq. (2.34) into equation (2.32) yields the classical Marcus equation:

$$k_{ET} = \kappa_{ET} \nu_n \exp\left[-\frac{(\lambda + \Delta G^0)^2}{4\lambda k_B T} \right] \tag{2.35}$$

Equations. (2.34) and (2.35) and Figure 2.5 indicate that for the exergonic reactions, ΔG^* will decrease and k_{ET} will consequently increase as ΔG^0 becomes more negative. When $-\Delta G^0 = \lambda$ (Figure 2.5-c), $\Delta G^* = 0$ and k_{ET} reaches it maximum value of $\kappa_{ET}\nu_n$. However, as ΔG^0 becomes more negative in a highly exergonic reaction, the intersection point of the R and P

surfaces moves to left of the center of the R surfaces as shown in Figure 2.5-d. ΔG^* should increase again and thus, from the eq. (2.35), k_{ET} will decrease as the reaction becomes highly exergonic in what has been called ***the Marcus Inverted Region***.

2.2.2. Reorganization energy

The total reorganization energy, λ, is usually divided into two terms,

$$\lambda = \lambda_{in} + \lambda_{out} \tag{2.36}$$

Where λ_{in} is the *inner-sphere* reorganization energy and λ_{out} is the *outer-sphere* reorganization energy. Inner-sphere reorganization energy refers to the energy changes accompanying changes in bond lengths and bond angles during electron transfer step. Outer-sphere reorganization energy is the energy change as the solvent shells surrounding the reactants rearrange.

The energy associated with changes in bond lengths (the inner-sphere reorganization energy) is given by the following equation [56]:

$$\lambda_{in} = \sum_i \left[\frac{f(R)_i \, f(P)_i}{f(R)_i + f(P)_i} \right] \left[\Delta q_i \right]^2 \tag{2.37}$$

Where Δq_i is the difference in equilibrium bond distance between the reactant and product states corresponding to a *ith* vibration, and *f(R)* and *f(P)* are the force constants for this vibration for a reactant and product molecule. The quantity contained in brackets is referred to as *the reduced force constant*. Equation (2.37) includes the summation of all vibrational modes and applies to the limit case where all vibrational states (assumed to display harmonic behaviour) are populated. This latter condition represents a case where λ_{in} is assumed to be temperature independent.

Solvent reorganization denotes the effects of orientational changes in the solvent molecules surrounding the reactants during electron transfer. In this section we show that solvent plays a special role in establishing the unique nature of the transition state in electron transfer. The reorganization due to the solvent contribution is closely related to the polarization of the solvent molecules surrounding a reactant pair. The solvent polarization is the sum of an orientational-vibrational and an electronic component [57]:

$$P = P_e + P_u \tag{2.38}$$

P is the total polarization, P_e is the electronic polarization, and P_u is the orientational-vibrational polarization of the solvent molecules. P_e is associated with the optical dielectric

constant, ε_{op}, which is in turn equal to the square of the refractive index, n^2. P_u is associated with the static dielectric constant, ε_s. P_u, unlike P_e, responds more slowly at a much lower frequency with an oscillating electric field.

The outer-sphere reorganization energy is given by the following expression:

$$\lambda_{out}(kcal/mol) = 332\Delta e^2\left(\frac{1}{r_D}+\frac{1}{r_A}-\frac{1}{d_{cc}}\right)\left(\frac{1}{\varepsilon_{op}}-\frac{1}{\varepsilon_s}\right) \tag{2.39}$$

Where Δe is the charge transferred in the reaction, r_D and r_A are the radii of the donor and the acceptor, respectively and d_{cc} is the center-to-center distance between the donor and acceptor.

2.2.3. Adiabatic versus diabatic electron transfer reaction

The magnitude of the electronic coupling energy, H_{rp}, between the reactant and the product states is used to distinguish the two types of ET reaction.

$$H_{rp} = \langle \psi_R^0 | \hat{H}_{ET} | \psi_P^0 \rangle \tag{2.40}$$

Where ψ_R^0 and ψ_P^0 are the electronic wave functions of the equilibrium reactant and product states, respectively and $\hat{H}_{ET}$ is the Born-Oppenheimer (rigid nuclei) electronic Hamiltonian for the system. The ET reactions is said to be adiabatic if H_{rp} is moderately large, so that the Gibbs energy surface interact as shown in Figure 2.6-a. Because the surfaces are separated in the intersection region, the reaction always remains on the lower surface as it proceeds through the transition state and the transmission coefficient $\kappa_{ET} \simeq 1$ in eq. (2.35). When H_{rp} becomes so small that the *R* and *P* surfaces no longer interact significantly, the ET reaction is said to be diabatic. As indicated in Figure 2.6-b, the system will then usually remains on the [D· · ·A] surface as it passes through the intersection region and will return to the equilibrium state of reactant. Only occasionally it cross over to *P* surface, bring about the ET reaction. The point at which a reaction is to be regarded as adiabatic or diabatic varies with system. Adiabatic reactions are generally found in those cases in which D and A are relatively close together. In practice this means either van der Waals contact of D and A in the reactant state or close coupling of D and A in an intramolecular entity.

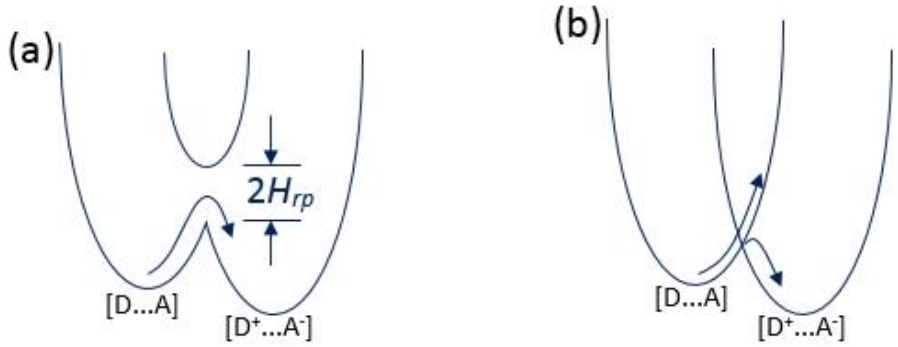

Figure 2.6. The electron transfer is said to be adiabatic (a) and diabatic (b). H_{rp} refers to the electronic coupling energy defined by eq. (2.40).

2.2.4. Inverted region

Mathematically, equation. (2.34) describes a quadratic relationship between the driving force and the free energy of activation. The physical meaning of this relationship will become apparent if we take a closer look at the rate constants (eq. (3.35)) of an excited state interacting with a series of homologous quenchers by an electron transfer mechanism [58]. If the $\log(k_{ET})$ is plotted vs. the driving forces ($-\Delta G^0$) , the Figure 2.7 describes the following trend: initially the rate will increase with an increase (more negative) in driving force and reach the maximum value in which $-\Delta G^0 = \lambda$. With further increases in the driving force, the rate constant should progressively decrease again.

Figure 2.8 shows the intersecting reactant and product potential energy surfaces. Starting with reactant and product curves (a), with increasing exothermicities, the activation energy progressively decreases until at some point it reaches zero (b). Here the rate attains its maximum value. With further increasing n the driving forces, the activation energy begins to increase again (c).

In photo-induced ET, the inverted region has important implications in charge separation and electron return. By taking advantage of the relationship, $-\Delta G^0 = \lambda$, one might be able control the onset of the inverted region for either forward ET or electron return and thereby influence reaction. If, for example, the reaction is dominated by the effects of solvent rather than bond reorganization, $\lambda \sim \lambda_{out}$. By varying the solvent, it is possible to change λ_{out}. Let us say that we want to increase the lifetimes of ion-pair intermediates by slowing the rate of electron return. We chose a solvent so that $-\Delta G^0 \gg \lambda$. This places the reaction in the inverted region.

In this kinetic region, electron return is slow [59-61], and accordingly the lifetime of ion-pair is enhanced.

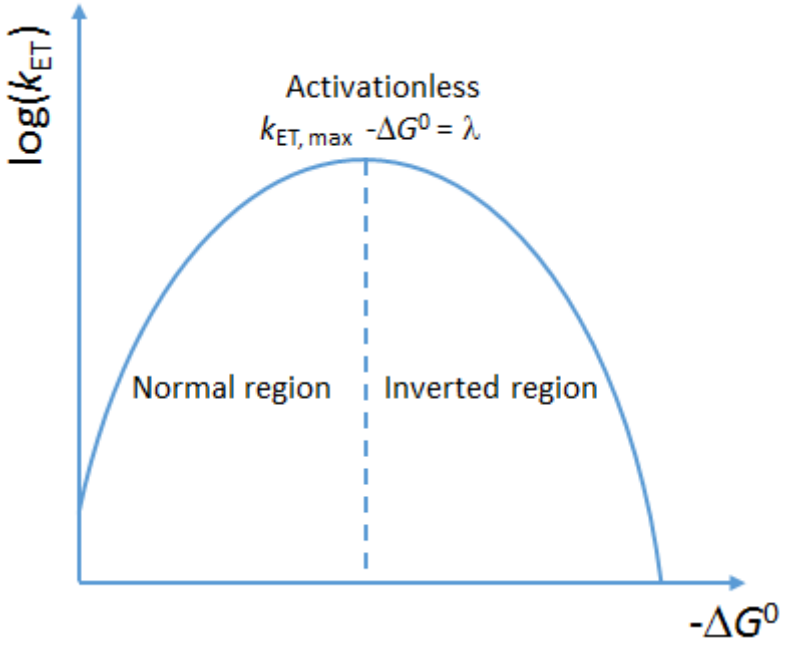

Figure 2.7. The log(k_{ET}) is a function of the driving force (-ΔG^0) of the ET reaction. At -ΔG^0 = λ, the rate constant reaches its maximum value.

2.2.5. Dynamic solvent effects

In equation (2.32), the rate of the electron transfer depends on the nuclear frequency, ν_n. The nuclear frequency consists of molecular vibrations in the reactants and solvent orientations. The intramolecular vibrations can be neglected. Thus, ν_n is largely related to dynamic solvent effects [1].

In Marcus theory, the focus of interest is on ΔG^*, which is contained in the exponential of eq. (2.35). In electron transfer where solvent polarity has a major effect on the activation energy, the solvent influences the outer-sphere reorganization energy. However, the solvation exercises a dynamic solvent effect. The dynamic solvent effect refers to the friction between reactants and polar solvents. Since the solvent molecules and the reacting molecules in ET are coupled electrostatically, the rates can be influenced dramatically. The outcome of this coupling turns up in the nuclear frequency ν_n. ν_n measures the frequency of solvent motion, or "how fast the polar solvents can respond to instantaneous charge". In our discussion of Marcus theory, we noted that solvent molecules can respond orientationally. Since there are

other solvent motions such as vibrational motions, the time required for solvation may span several time scales. However, it is convenient to consider only the orientational motion of solvent molecules. There may be a certain slowness associated with these motions, which ultimately may affect the rate. For any solvent, this orientational response can be represented by the longitudinal relaxation time, τ_L.

$$\tau_L = \frac{\varepsilon_{op}}{\varepsilon_s}\tau_D \tag{2.41}$$

The ratio $\frac{\varepsilon_{op}}{\varepsilon_s}$ measures the degree of coupling between the solvent and the reaction. ε_{op} and ε_s represent dielectric constants measured at different frequencies, ω ($\varepsilon_{op} \approx n^2$ for $\omega \to \infty$; ε_s ($\omega = 0$)). τ_L generally falls within the range of 10^{-13} to 10^{-10} s. τ_D is the dielectric relaxation time, represents the rotational diffusion time of a single particle. It is related to the viscosity of the solvent. Consequently, the longitudinal solvation time can be about order of magnitude smaller than τ_D.

If an adiabatic, outer-sphere ET takes place on a smooth and continuous potential energy surface, then, according to solvent dynamic theory, the rate of ET should be proportional to the inverse of the longitudinal relaxation time, i.e., $k_{ET} \propto \tau_L^{-1}$. This rate represents the maximum rate of an ET. This ET should occur much more rapidly in acetonitrile than the less polar and more viscous *n*-propanol. It should be pointed out, however, this correlation holds only for adiabatic where dynamic solvent motion is important. However, the possibility of significant nuclear and electronic barriers must be carefully sorted out before concluding that solvent dynamic effects dominant.

Experimentally, the response of a solvent to instantaneous charge can be estimated from dynamic Stokes measurements [62]. When a ground state molecule in equilibrium with its solvent environment is excited with an ultrashort pulse of light, molecule is converted to its excited state, which still has the ground state solvent orientation. During its short lifetime, the non-equilibrated excited state emits fluorescence. Eventually, as the solvent molecules reorient to the charge distribution of the excited state, the fluorescence emission shifts. The change in the fluorescence spectrum is related to the solvent response.

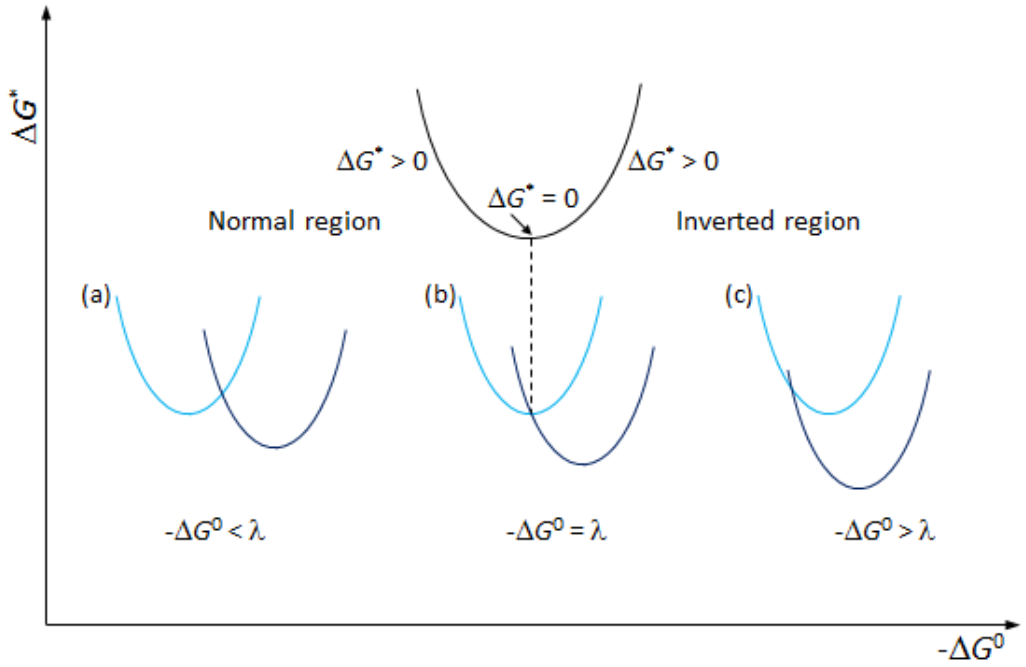

Figure 2.8. The parabolic curves: The top is a plot of ΔG^* *vs.* $-\Delta G^0$. The energy potential surfaces of the reactant and product shown in the bottom describe the relationships between the driving forces ($-\Delta G^0$) and reorganization energy (λ). The normal region ($-\Delta G^0 < \lambda$) is shown on the left, ΔG^* decreases with decreasing λ or as ΔG^0 becomes more negative. The inverted region ($-\Delta G^0 > \lambda$) is on the right, ΔG^* increases with decreasing or as ΔG^0 becomes more negative. When $\Delta G^* = 0$, the rate is maximum ($-\Delta G^0 = \lambda$) and this case is shown in the center.

2.3. Magnetic field effects

The present part will focus on the radical pair mechanism to explain the mechanism of the magnetic field effects (MFEs) on chemical [63, 64]. There is an inspection of the two spin-mixing mechanisms, including the hyperfine-mechanism and the Δg-mechanism. The effect of the radical pair mechanism at intermediate fields on chemical reactions within the low-viscosity approximation will be addressed. Finally, the photo-induced ET reaction scheme and MFE on the exciplex emission will be described.

2.3.1. Radical pair mechanism

Radical pairs are generated via photo-induced electron transfer reactions of excited fluorophores with quenchers. The spin multiplicity [singlet (S) or triplet (T)] of the correlated

geminate radical pairs retain the spin multiplicity of their precursors, according to the rules of spin conservation, i.e., the precursor is a singlet state, the singlet product will be born and the triplet precursor will give rise to triplet product. If, however, under suitable condition, the radicals are separated to the distance where the S-T conversion becomes feasible through such weak magnetic interactions as the Zeeman effect or the hyperfine coupling.

The spin Hamiltonian, H_{RP}, for a radical pair, this is two spatially separated spin correlated electron spins, in solution can be written as

$$H_{RP} = H_{ex} + H_{mag} \tag{2.42}$$

Here, the first term refers to the distance dependent exchange interaction between the two electron spins.

$$H_{ex} = -J(r)(2S_1.S_2 + \frac{1}{2}) \tag{2.43}$$

Where S_i is the operator of the electron spin *i* and *J(r)* is the exchange integral between the two electron spins, depending on the inter-radical separation. The exchange interaction arises when the electronic wavefunctions of two unpaired electrons overlap and their spins exchange.

$$J(r) = 2\int \psi_1^*(r_1)\psi_2^*(r_2)\frac{1}{|r_1 - r_2|}\psi_2(r_1)\psi_1(r_2)dr_1dr_2 \tag{2.44}$$

Where $\psi_i(r_j)$ refers to the wavefunction of electron *i* at position r_j . The experiments showed that *J(r)* decreases exponentially with inter-radical separation [65].

$$J(r) = J_0 \exp\left(-\frac{r-\sigma}{L}\right) \tag{2.45}$$

The second term in eq. (2.42) gives the effect of a magnetic field on the radical ion pair.

$$H_{mag} = (g_1\mu_B BS_{1z} + g_2\mu_B BS_{2z}) + (\sum_i a_{1i} S_1.\hat{I}_{1i} + \sum_i a_{2j} S_2.\hat{I}_{2j}) \tag{2.46}$$

The first term in eq. (2.46) denotes Zeeman interaction and the second term gives hyperfine interaction. g_i is the isotropic electron *g*-factor of radical *i*, μ_B is the Bohr magneton, S_{iz} is the *z*-component of the *i*th electron spin operator, S_i and $\hat{I}_{ij}$ denote the *j*th nuclear spin operator for the *i*th electron spin with its corresponding isotropic hyperfine coupling constant, a_{ij} .

This combination of two spatially separated, though still correlated, electron spin with spin quantum numbers S_1 = ½ and S_2 = ½ generates a new set of singlet and triplet states which

can be expressed via the product of their individual electron ($|X\rangle$) and nuclear spin ($|\chi_i\rangle$) wavefunctions

$$|S\rangle = \frac{1}{\sqrt{2}}(|\alpha_1\beta_2\rangle - |\beta_1\alpha_2\rangle) \tag{2.47a}$$

$$|T_0\rangle = \frac{1}{\sqrt{2}}(|\alpha_1\beta_2\rangle + |\beta_1\alpha_2\rangle) \tag{2.47b}$$

$$|T_{+1}\rangle = |\alpha_1\alpha_2\rangle \tag{2.47c}$$

$$|T_{-1}\rangle = |\beta_1\beta_2\rangle \tag{2.47d}$$

Where α and β denote the parallel (spin-up, m_s = +1/2) and antiparallel (spin-down, m_s = -1/2) magnetic substates of the electron in the presence of an external magnetic field, B_z, respectively. Figure 2. 9 depicts the vector representation for the two electron spins of the geminate radical ion pair in the presence of an external magnetic field, B_z. The overall spin quantum number, S = 0, 1, and magnetic spin quantum number, M_s = -1, 0, 1, for the correlated spin pair are indicated. The nuclear spin wavefunctions are given by:

$$|\chi_N\rangle = \prod_i^a |m_{I,i}\rangle \prod_j^b |m_{I,j}\rangle \tag{2.48}$$

Here $m_{I,i}$ and $m_{I,j}$ refer to the magnetic nuclear spin quantum numbers on atom *i* of radical 1 and atom *j* of radical 2.

In the presence of an external magnetic field, the energies of the S and T states of the radical ion pair are given by:

$$E(S) = \langle S, \chi_N | H_{ex} | S, \chi_N \rangle = J(r) \tag{2.49a}$$

$$E(T_n) = \langle T_n, \chi_N | H_{ex} | T_n, \chi_N \rangle = -J(r) \tag{2.49b}$$

With *n* = -1, 0, +1 for the three triplet states, $|T_{-1}\rangle$, $|T_0\rangle$, $|T_{+1}\rangle$, respectively. The distance dependence of the exchange integral $J(r)$ expresses the S and T energies distance dependence as well.

The S and T energies are shown in Figure 2.10. Figure 2.10-a shows the S and T energies in the absence of an external magnetic field. The energy gap is separated at close inter-radical distances *r* and it becomes smaller at large separation distances. In the presence of an external magnetic field, the singlet and triplet energies are given by:

$$E(S) = \langle S, \chi_N | H_{ex} + H_{mag} | S, \chi_N \rangle = J(r) \tag{2.50a}$$

$$E(T_n) = \langle T_n, \chi_N \left| H_{ex} + H_{mag} \right| T_n, \chi_N \rangle = -J(r) + ng\mu_B B + \frac{n}{2}(\sum_i a_{1i} m_{I,i} + \sum_j a_{2j} m_{I,j}) \quad (2.50b)$$

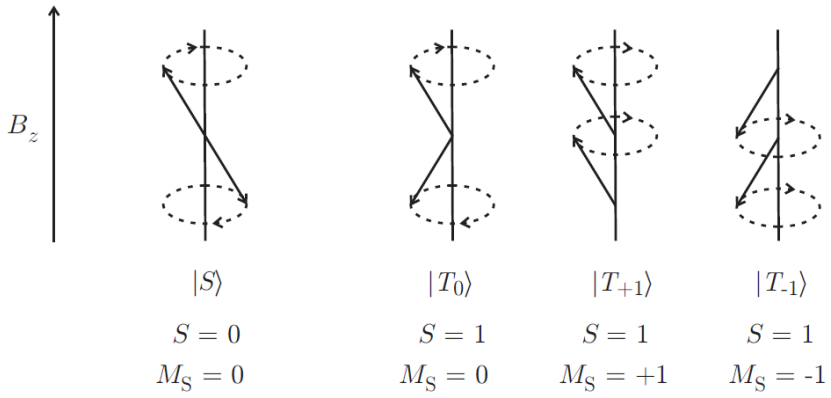

Figure 2.9. Vector presentation for the two electron spins of the spin correlated radical ion pair in the presence of an external magnetic field. The precession of the electron spin angular momentum vectors, S_i, about the external magnetic field, B_z, is included.

Due to Zeeman interaction, the degeneracy of the three triplet sates is now lifted by $g\mu_B B$ (Figure 2.10-b). Figure 2.11 shows the energy level diagram at a given inter-radical separation distance r in the absence (left) and presence of an external magnetic field (right). As a consequence, at large distances the degeneracy between all three triplet states and the singlet state is reduced to a degeneracy between $|S\rangle$ and $|T_0\rangle$ only. Furthermore, another degeneracy between $|S\rangle$ and $|T_-\rangle$ arises at intermediate separation distances giving rises to the called ‘‘level-crossing’’ mechanism [64].

When the singlet and triplet states are degenerate, S-T mixing occurs. This spin conversion occurs through the off-diagonal elements of the radical pair Shrödinger equation.

$$\langle T_0, \chi_N \left| H_{ex} + H_{mag} \right| S, \chi_N \rangle = \frac{1}{2}\left[\Delta g \mu_B B + \sum_i a_{1i} m_{I,i} - \sum_j a_{2j} m_{I,j} \right] \quad (2.51a)$$

$$\langle T_{\pm 1}, \chi_N' \left| H_{ex} + H_{mag} \right| S, \chi_N \rangle = \frac{\pm a_i}{2\sqrt{2}}\left[I_i(I_i+1) - m_{I,i}(m_{I,i} \pm 1) \right]^{1/2} \quad (2.51b)$$

Here $\Delta g = g_1 - g_2$ is the difference of the two isotropic g values of the radical pair and $m'_{I,i} = m_{I,i} \pm 1$ and $m'_{I,j} = m_{I,j}$, where the dashed quantum numbers refers to χ'_N. For the $S - T_{\pm 1}$ transition a different nuclear configuration is required to ensure the conservation of the total angular momentum (spin plus orbital angular momentum).

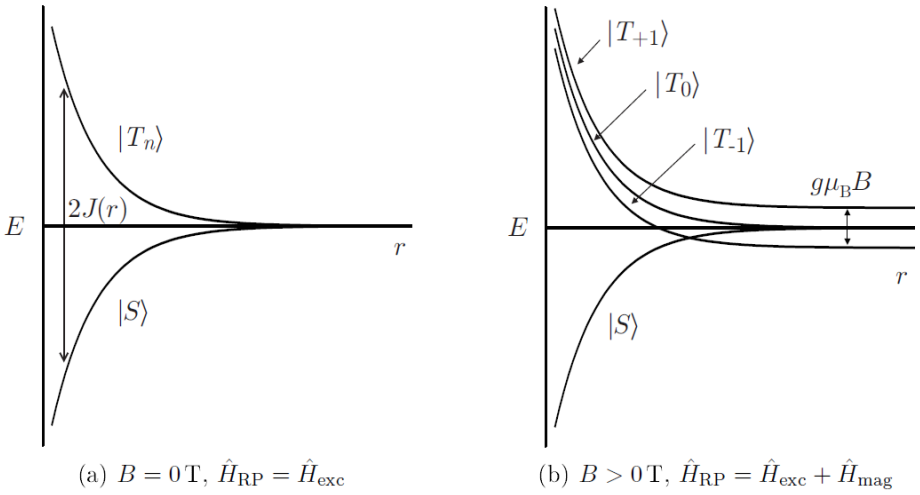

Figure 2.10. The dependence of the energy difference between singlet and triplet states of the radical ion pair in the absence (a) and presence (b) of an external magnetic field for the case of a negative exchange integral *J*.

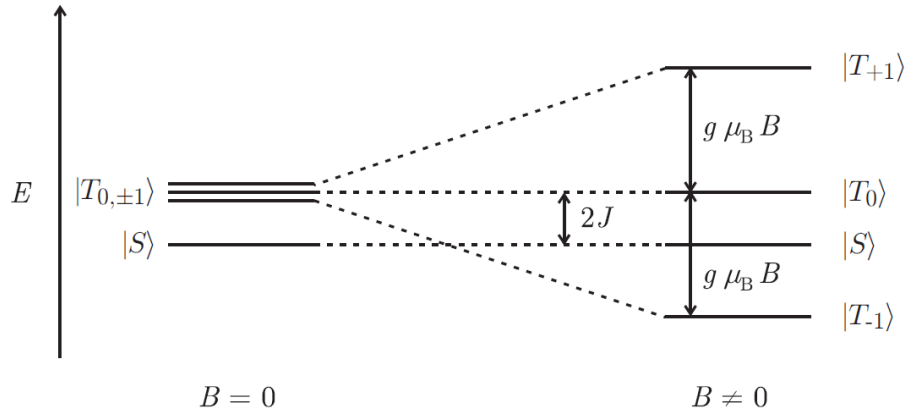

Figure 2.11. Energy levels of singlet and triplet states of a radical ion pair in the absence and presence of an external magnetic field.

Inspection of eqs. (2.50) and (2.51) allows to attribute the S-T conversion in radical pairs to the following terms: a) The Zeeman term in eq. (2.51a) which is given by $\Delta g \mu_B B$; b) the hyperfine coupling terms in eq. (2.51b) which are characterized by a_i and a_j; and finally c) the exchange term, which is characterized by J and its intrinsic distance dependence. From these observations it is possible to classify the MFEs on chemical reactions through radical pairs by the following mechanisms:

+ Δg mechanism: applicable when $\Delta g \neq 0$, $J = 0$, and $a_i = a_j = 0$

+ Hyperfine Interaction (HFI) mechanism: applicable when $\Delta g = 0$, J = 0 and $a_i \neq 0$ and/or $a_j = 0$

Additionally, other mechanisms, such as the relaxation mechanism, spin-orbit coupling, or the level crossing mechanism can induce S-T conversion in radical pairs. However, these three mechanisms are not at all important for the freely diffusing, no heavy atoms containing, radical pairs studied in the present work.

Δg mechanism

When the two electronic spins on the two radicals possess different *g*-values. As a consequence their Larmor frequencies, $\omega_i = g_i \mu_B \hbar^{-1} B$, with which they precess about the external magnetic field effect, giving rise to a dephasing of the precessing of S_1 and S_2 with respect to each other (Figure 2.12). As a result the spin multiplicity will oscillate between $|S\rangle$ and $|T_0\rangle$ with the frequency.

$$\omega_{ST_0} = \omega_1 - \omega_2 = (g_1 - g_2)\mu_B \hbar^{-1} B = \Delta g \mu_B \hbar^{-1} B \tag{2.52}$$

Figure 2.13-a gives a schematic representation of S-T conversion by Δ*g* mechanism. This mechanism induces a S-T conversion only in the presence of an external magnetic field, *B* through the $\Delta g \mu_B B$ term in eq. (2.51a). Due to Zeeman interaction, the $|T_{-1}\rangle$ and $|T_{+1}\rangle$ states are lifted energetically remove from the $|S\rangle$ state. Thus there is no mixing between $|S\rangle$ state and $|T_{\pm}\rangle$.

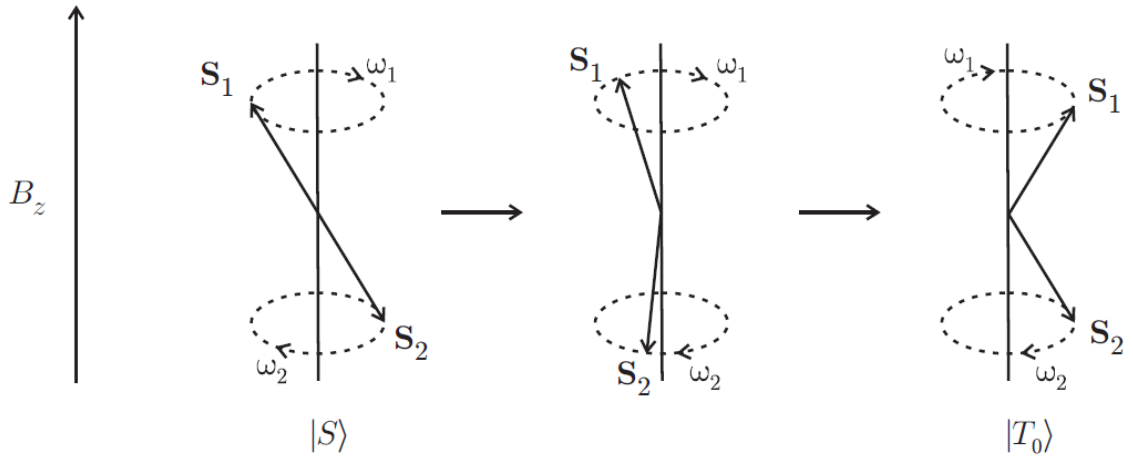

Figure 2.12. Vector model of the S-T_0 conversion in a radical pair. The dephasing of the S_1 and S_2 spins which gives rise to the oscillatory S-T_0 transition may be caused by different *g*-value of the two radicals (Δ*g*-mechanism) or by hyperfine interaction.

The dependence of the singlet probability, ρ_S, on an external magnetic field is depicted in Figure 2.13-b, for a short lived radical pair, created in its singlet state, where spin evolution can occur only to some small extent. The increasing importance of the Δg-mechanism at high external magnetic fields, resulting in a reduction of the singlet probability, is obvious.

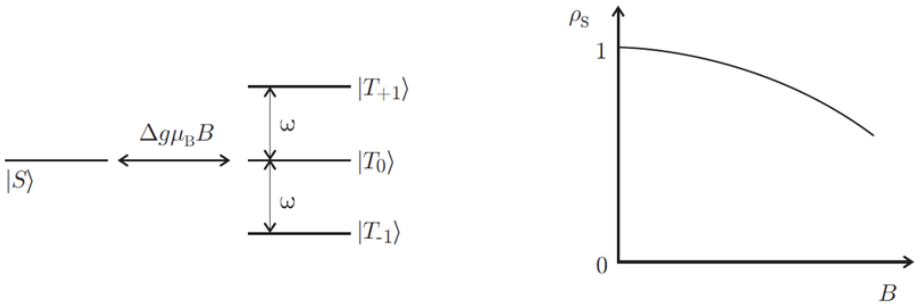

(a) Energy levels and transitions for the Δg-mechanism.

(b) Magnetic field effect dependence of the singlet probability, ρ_S, for a short living radical pair, initially created in the S state. $J = 0$, $a_i = 0$.

Figure 2.13. S-T conversion by Δg mechanism (a) and the dependence of the singlet probability, ρ_S, on an external magnetic field (b).

Hyperfine Interaction mechanism

The electron-nuclear hyperfine interaction (HFI) induces S-T transitions qualitatively different depending on the external applied magnetic field. At applied magnetic fields which exceed the magnetic field, which is induced by the magnetic nuclei of the radical at the location of the unpaired electron spin (B > 10 to 100 mT), the HFI-mechanism operates in a way similar to the Δg-mechanism. Now, the HFI has the effect of an additional local magnetic field that alters the precession frequency of the electronic spin (see Figure 2.12). The electronic spin on the two radicals will have different local fields resulting in different precession frequencies, which then induce spin conversion. Contrary to the Δg-mechanism, the S-T transition rate is magnetic field independent. The large Zeeman splitting at high external magnetic fields renders the S-T_0 transition the only feasible mixing channel (see Figure 2.51-a).

Generally the unpaired electron precesses about a magnetic field, B_{tot}, which is the vector sum of the external magnetic field, B_{ext}, and the local hyperfine field, B_{HFI}. Whenever $B_{ext} >> B_{HFI}$ the directions of B_{tot} and B_{ext} practically coincide, and hence the electron spin projection onto the external field is not altered. In low external fields, however, B_{tot} and B_{ext} don not coincide

and thus the precess about B_{tot} affects the spin projection onto B_{ext} giving rise to transition from S to all three T states. Figure 2.14 describes the situation for zero external field and static electron spin on radical 2. The S-T transition occurs in the course of the precession of the unpaired electron spin S_1 and the nuclear spin I about their resultant (transitions to the other two triplet states occurs in completely analogous way).

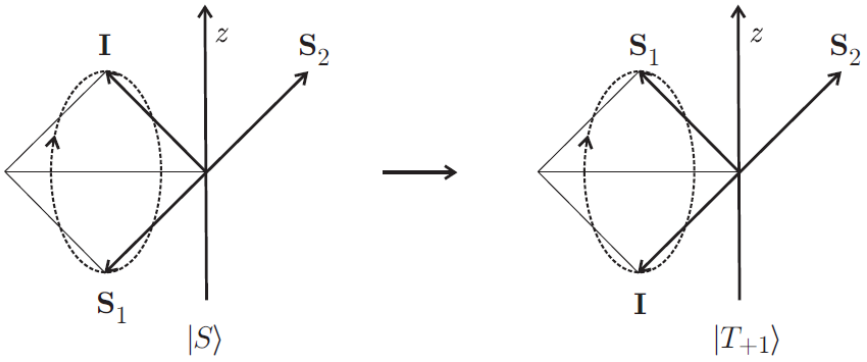

Figure 2.14. Vector model of HFI induced S-T_+ transition at zero magnetic field. The electron spin, S_1, and total nuclear spin, I, precess about their resultant and thereby change their projections onto the *z*-axis.

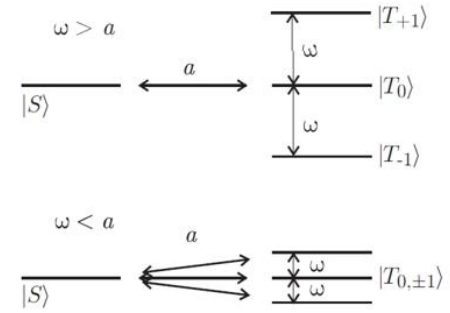

(a) HFI mechanism at high external magnetic field ($\omega = g\mu_B B > a$) (above) and at small and zero external magnetic field ($\omega = g\mu_B B < a$).

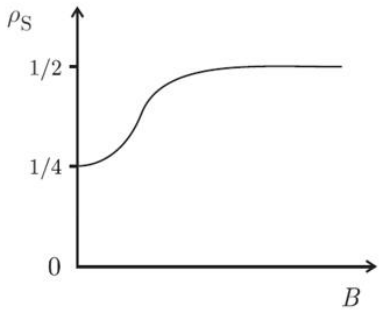

(b) Magnetic field dependence of the singlet yield, ρ_S, for an infinitely long living radical pair, initially created in the S state. J = 0, Δg = 0.

Figure 2.15. S-T transition by the HFI-mechanism. At high field, the mixing occurs between $|S\rangle$ and $|T_0\rangle$ since the $|T_{+1}\rangle$ and $|T_{-1}\rangle$ states are energetically split due to the Zeeman interaction (here expressed in terms of the angular frequency $\omega = g_i\mu_B\hbar^{-1}B$). At low and zero external magnetic field the smaller energy gap between $|S\rangle$ and $|T_{-1}\rangle$ and $|T_{+1}\rangle$ allows for transitions between singlet and all three triplet states.

2.3.2. Magnetic field effects in view of the low viscosity approximation

The magnetic field effect (MFE), χ, is defined as the difference in the yield of a given species in reaction such as radical ions, triplets, exciplexes, etc., in the presence, $\phi(B)$, and absence, $\phi(B_0)$, of an external magnetic field divided by the product yield at zero field.

$$\chi = \frac{\phi(B) - \phi(B_0)}{\phi(B_0)} \tag{2.53}$$

The low viscosity approximation includes the following two simplifications:

a) The exchange interaction is negligible, i.e., it is assumed zero over the entire domain of spatial diffusion.

b) The diffusional evolution of the radical pair, $n(r, t)$, and its spin evolution given by the singlet probability, $\rho_S(B, t)$, are treated independently (see the experimental section).

The product yield for species i is hence given as the integral of the singlet or triplet probability of this species, $\rho_i(B, t)$, weighted by a suitable function $f(t)$, which describes the species' formation:

$$\phi_i = \int_0^\infty \rho_i(B,t)\, f(t) dt \tag{2.54}$$

2.3.3. Photo-induced electron transfer reaction scheme and time-resolved magnetic field effect of exciplex emission

Exciplexes appear as intermediate species in photochemistry. In general, exciplexes can be observed by their emission. Furthermore, under suitable conditions, the exciplex production is sensitive to an external magnetic field [25-36]. MFEs on exciplexes result from the inter-conversion of the singlet and the three triplet states of the RIP in equilibrium with the exciplex. This process is sensitive to the presence of an external magnetic field which lifts the degeneracy of the three triplet states and, thus, reduces the singlet-triplet conversion ($S\text{-}T_{+-}$). This causes an increase of the singlet population of the initial spin state in the presence of a magnetic field. Due to the reversible conversion of the exciplex and the singlet RIP, the exciplex luminescence becomes magnetosensitive. Figure 2.16 depicts a reaction scheme of the photo-induced ET processes of an exciplex forming donor-acceptor system. The involved species can be classified by their inter-particle distance and the solvent polarization expressed by the Marcus outer-sphere ET coordinate. Here, the horizontal arrangement is arbitrary.

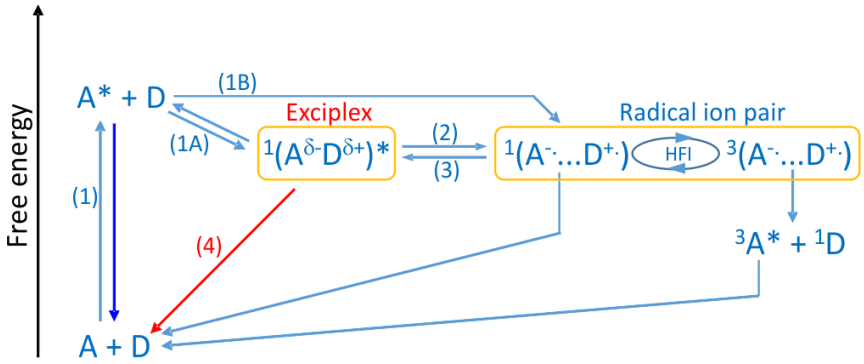

(a) Free acceptor/donor pair

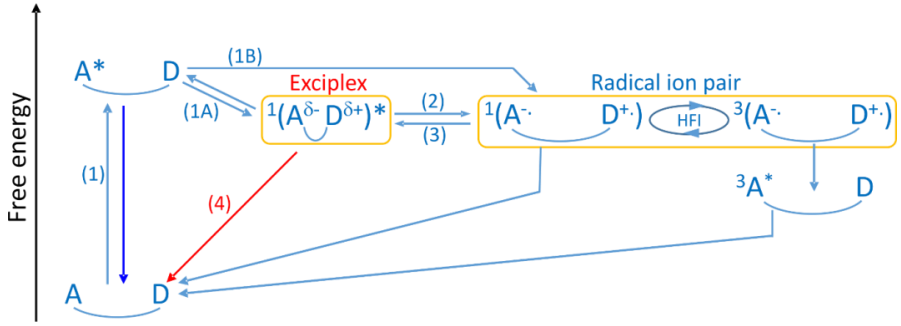

(b) Chain-linked acceptor/donor pair

Figure 2.16. Schematic representation of the species involved in the process of the magnetic field effect on the exciplex of free acceptor/donor (a) and chain-linked acceptor/donor (b) pairs: photoexcitation (1), exciplex formation (1A), direct formation of the RIP via remote electron transfer (1B), exciplex dissociation into RIP (2), spin evolution by hyperfine interaction (HFI), the singlet RIP re-forms the exciplex (3) and exciplex emission (4). The red and blue arrows denote the fluorescent decay process of either the photo-excited acceptor (magneto-insensitive) or the exciplex (magneto-sensitive) that are observed in the experiment. The magnetically sensitive species are enclosed in the frame. Spin multiplicities are indicated by superscripts.

Magnetic field effect on exciplex can proceed as following: An electron acceptor (A) in ground state absorbs light to become an excited state (A*). The excited state is quenched via electron transfer (ET) with an electron donor (D) in a process called as photo-induced electron transfer (PET) reaction. In the course of the quenching process via ET, the two initial quenching products are possible (1A versus 1B). The singlet radical ion pair (RIP) can be formed via distant ET (1B) or by the dissociation of an exciplex (2), which is formed via reaction (1A). The singlet RIP so obtained can undergo inter-system crossing induced by the

hyperfine coupling interaction and the Zeeman interaction. By applying an external magnetic field, because of the Zeeman interaction, the singlet $|S\rangle$ and $|T_{\pm}\rangle$ states are not degenerate. There is only S-T_0 transition, this causes an increase in the singlet probability. Only the singlet RIP can reform the exciplex and, thus, its formation and emission can be influenced by an external magnetic field. Furthermore, since exciplex dissociation is a typically slow process, the ions resulting from the exciplex dissociation will be delayed with respect to those formed by direct electron transfer. As a consequence the MFE generated by the exciplex route will also be delayed. Thus, time-resolved studies of MFE of the exciplexes, allow deducing the initial quenching state (i.e., 1A versus 1B in Figure 2.16).

It is now possible to reformulate the magnitude of magnetic field effect introduced in eq. (2.53) by taking the exciplex quantum yield as the observable species of interest,

$$\chi = \frac{\phi_{exc}(B) - \phi_{exc}(B_0)}{\phi_{exc}(B_0)} = \frac{\Delta\phi_{exc}}{\phi_{exc}} \tag{2.55}$$

Here $\phi_{exc}(B)$ and $\phi_{exc}(B_0)$ give the exciplex quantum yield in the presence and absence of an external magnetic field, respectively. Within the low-viscosity approximation the numerator can be expressed as:

$$\Delta\phi_{exc} \propto \int_0^{\infty} f(t)(\rho_S(B,t) - \rho_S(B_0,t))dt \tag{2.56}$$

Here ρ_S refers to the singlet probability-as only the singlet RIP is capable of forming the exciplex and $f(t)$ represents a recombination function describing the reformation of the exciplex. Assuming, that the radical ion pair only decays via the exciplex, the quantum yield of the exciplex can be expressed as:

$$\Delta\phi_{exc} \propto 1 - \phi_{ions} \tag{2.57}$$

With ϕ_{ions} giving the yield of free ions (or the survival probability of the radical pair at infinite time).

2.4. Theory of experiments

2.4.1. Meaning of the lifetime in time-correlated single photon-counting (TCSPC) technique

The time-domain and frequency-domain methods are widely employed to measure time-resolved fluorescence [66]. In time-domain, the sample is excited with a pulse of light (Figure

2.17). The width of the pulse is much shorter than the decay time τ of the sample. The fluorescence intensity decay, I(t), is a function of time and recorded after excitation pulse. The lifetime of the sample is determined from the slope of a plot of ln I(t) versus time, t, or from the time at which the intensity decreases to 1/e of the intensity at t = 0.

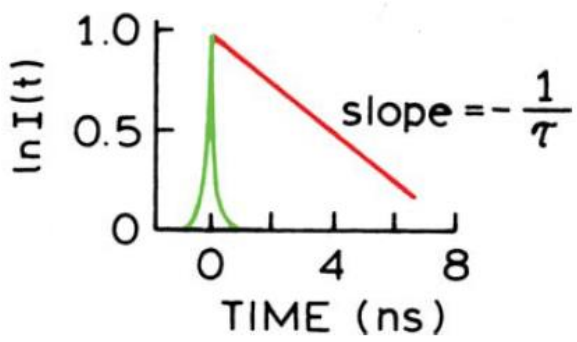

Figure 2.17. The lifetime of sample is calculated from the slope of a plot of ln I(t) versus time, t.

The meaning of the lifetime, τ, should be consider prior to further discussion of the lifetime measurements. The fluorophores are excited with an infinitely sharp (δ-function) pulse of the light, resulting in an initial population (n_0) of excited fluorophores. The excited states decay via radiative and/or non-radiative pathways with a rate constant (Γ + k_{nr}). The rate of the decay is expressed as:

$$\frac{dn(t)}{dt} = (\Gamma + k_{nr})n(t) \tag{2.58}$$

Where $n(t)$ is the population of the excited molecules at time t following excitation, Γ is the radiative rate , and k_{nr} is the non-radiative rate. Emission is a random event, and each excited fluorophore has the same probability of emitting in a given period of time. The results in an exponential decay of the excited state population.

$$n(t) = n_0 \exp\left(-\frac{t}{\tau}\right) \tag{2.59}$$

Fluorescence intensity is observable in experiment. It is proportional to the number of excited molecules. Hence, eq. (2.59) can be expressed in the term of the time-dependent intensity I(t).

$$I(t) = I_0 \exp\left(-\frac{t}{\tau}\right) \tag{2.60}$$

Where I_0 is the intensity at $t = 0$ and $\tau = \left(\Gamma + k_{nr}\right)^{-1}$. The fluorescence lifetime can be determined from the slope of a plot of log $I(t)$ versus t, but more commonly by fitting the data to assumed decay models (see below).

If the sample displays more than one decay time, intensity decays are typically fit to the multi-exponential model:

$$I(t) = \sum_i \alpha_i \exp\left(-\frac{t}{\tau_i}\right) \tag{2.61}$$

Where α_i values are called the pre-exponential factors and τ_i is the lifetime of species i in the sample.

The lifetime of fluorescence species is the average amount of time, $<t>$, a species remains in the excited state following excitation. This value is obtained by averaging t over the intensity decay (eq. 2.60) of the species:

$$< t >= \frac{\int_0^\infty tI(t)dt}{\int_0^\infty I(t)dt} = \frac{\int_0^\infty t\exp\left(-t/\tau\right)dt}{\int_0^\infty \exp\left(-t/\tau\right)dt} \tag{2.62}$$

Solution of the denominator is equal to τ while the numerator is equal to τ^2. This results in eq. (2.63):

$$< t >= \tau \tag{2.63}$$

It is important to note that eq. (2.63) is not true for more complex decay laws, such as multi- or non-exponential decays. Another important concept is that the lifetime is a statistical average, and fluorophores emit randomly throughout the decay. The fluorophores do not all emit at a time delay equal to the lifetime. For a large number of fluorophores some will emit quickly following excitation and some will emit at times longer than the lifetime. This time distribution of emitted photons is the intensity decay.

2.4.2. Example of TCSPC data

The electronic components will be described in more detail in experimental section. Here the experimental data of TCSPC method is shown as an example. Intensity decay for 1-bromo-8-[9-(10-methyl)anthryl]octane (MAnt-8-Br) is shown in Figure 2.18. The light source used for excitation of the sample was a 374 nm laser diode (Picoquant, LDH series, Pulse FWHM 60 ps). A photomultiplier tube (PMT, Hamamatsu, R5600-U04) in combination with a non-fluorescing emission filter LP 435 was used to detect the optical signal.

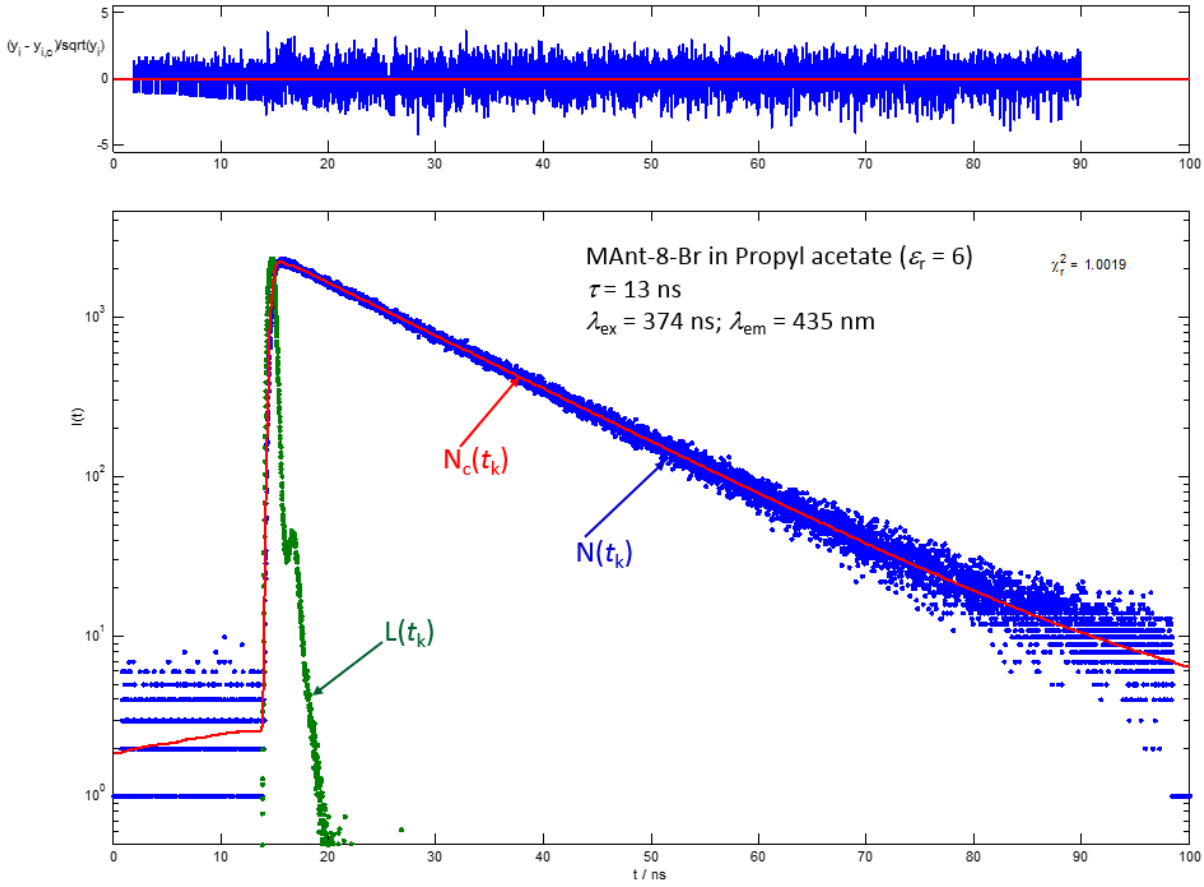

Figure 2.18. TCSPC data for 1-bromo-8-[9-(10-methyl)anthryl]octane (MAnt-8-Br) in propyl acetate. The green curve, $L(t_k)$, denotes the instrument response function. The blue curve, $N(t_k)$, gives the measured data and the red curve, $N_c(t_k)$ is called the fitted function. The lifetime of the fluorophore, τ, determined after fitting is 13 ns The upper panel shows some minor systematic error.

There are typically three curves associated with an intensity decay. These are the measured data $N(t_k)$, the instrument response function $L(t_k)$, and the calculated decay $N_c(t_k)$. These functions are in terms of discrete times (t_k) because the counted photons are collected into channels each with a known time (t_k) and width (Δt_k). The instrument response function (IRF) is the response of the instrument to a zero lifetime sample. This curve typically collected using a dilute scattering solution such as colloidal silica and no emission filter. This decay represents the shortest time profile that can be measured by the instrument.

The measured intensity decay, $N(t_k)$, is shown as a histogram of dots. The *y*-axis represents the number of photons that were detected within the timing interval t_k to $t_k + \Delta t$, where Δt is the width of the timing channel. The last curve is calculated data, $N_c(t_k)$, which is usually

called the fitted function. This curve represents a convolution of the IRF with the impulse response function, which is the intensity decay law. The fitted function is the time profile expected for a given intensity decay when one considers the form of the IRF. For exponential decay the lifetime is the value of τ that provides the best match between the measured data, $N(t_k)$, and the calculated curve, $N_c(t_k)$.

3. EXPERIMENTAL

3.1. Reactants

In this thesis inter- and intra-acceptor/donor systems were used to investigate electron transfer driving force and solvent dependences on the mechanism of fluorescence quenching and magnetic field effects (MFEs) of the exciplexes in inter- and intramolecular photo-induced ET reactions.

3.1.1. Inter-molecular photo-induced electron transfer systems

3.1.1.1. Acceptors (fluorophores)

9,10-Dimethylanthracene (DMAnt, Aldrich, 99%) was used as received, 9-methylanthracene (MAnt, Aldrich, 98%) and anthracene (Ant, Aldrich, 99%) were recrystallized from ethanol. The chemical structures and some parameters of the fluorophores are shown in Figure 3.1 and Table 3.1.

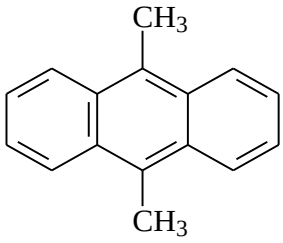

9,10-Dimethylanthracene
(DMAnt)

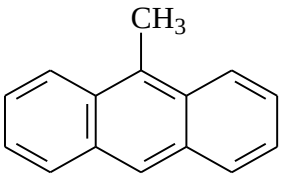

9-Methylanthracene
(MAnt)

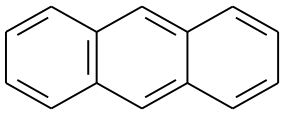
Anthracene
(Ant)

Figure 3.1. Chemical structures of electron acceptors used in time-resolved magnetic field effect studies.

3.1.1.2. Donors (quenchers)

N,*N*-dimethylaniline (DMA, Aldrich, 99.5%) and *N*,*N*-diethylaniline (DEA, Aldrich, 99.5%) were distilled under reduced pressure and subsequently handled under an argon atmosphere.

Structures and some parameters of the donors used in the magnetic field studies are depicted in Figure 3.2 and Table 3.1.

Inter-acceptor/donor pairs used in this thesis provide a change of free energy difference, $-\Delta G^0$, of the photo-induced ET within a range from 0.28 to 0.58 eV.

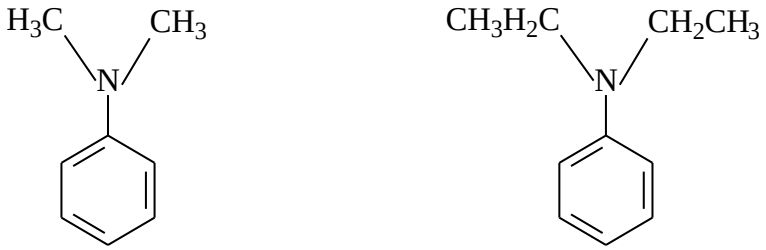

N,*N*-Dimethylaniline (DMA)

N,*N*-Diethylaniline (DEA)

Figure 3.2. Chemical structures of electron donors used in experiments

3.1.2. Intra-molecular photo-induced electron transfer systems

A brief summary of the used chemicals for the synthesis of polymethylene-linked acceptor/donor systems refers to Table 3.2. The chain-linked 9-methylanthracene (Mant)/*N*,*N*-dimethylaniline (DMA) systems, Mant-$(CH_2)_n$-O-$(CH_2)_2$-DMA (Mant-*n*-O-2-DMA), were synthesized by the following procedure (Scheme 3.1):

9-bromo-10-methylanthracene: This compound was synthesized following the published procedure [68]. A stirred mixture of 9-methylanthracene (960 mg, 5.0 mmole) and copper (II) bromide (2.24 g, 5.0 mmole) in chlorobenzene (200 ml) was heated under reflux for 24h. The reaction mixture was filtered and concentrated in vacuo. The residue was then purified by chromatography on alumina eluting with *n*-hexane to obtain 9-bromo-10-methylanthracene (0.83 g, 60 % yield). Mp: 169-171 ^{0}C. See ^{1}H-NMR spectrum in appendix A.2.

1-bromo-10-[9-(10-methyl)anthryl]decane (Mant-10-Br) [45]**:** 2.5M solution (2.8 ml) of *n*-butyllithium in hexane was added dropwise to a solution of 9-bromo-10-methylanthracene (1 g, 3.68 mmole) in dried diethyl ether (20 ml) under argon atmosphere in an ice bath to maintain the temperature at 0 ^{0}C. The mixture was stirred at 0 ^{0}C for 4h. After adding 3.4 g (11.33 mmole) of 1,10-dibromodecane at once, the mixture was stirred for 30 minutes. The reaction mixture was refluxed for 2h in an oil bath. The resulting mixture was extracted by

benzene (3×25 ml). The benzene layers were combined and washed with water (2×50 ml). The separated organic layer was dried over $MgSO_4$ overnight. The solution was concentrated in vacuo. The residue was absorbed on the Silica gel and run column chromatography eluting with *n*-hexane to give Mant-10-Br (0.78 g, 52% yield). Mp: 77-78 ^{0}C. The ^{1}H-NMR spectrum is shown in appendix A.2.

Table 3.1. Physical parameters of the used acceptors and donors [67]: The 0,0-energy E_{00}, lifetime of acceptors (A), τ_A, and donors (D), τ_D, reduction and oxidation potentials, $\boldsymbol{E_{1/2}^{red}}$ and $\boldsymbol{E_{1/2}^{ox}}$, respectively. The free energy difference of electron transfer $-\Delta G^0$ was calculated at ε_s = 13 in propyl acetate/butyronitrile mixture, using the Rehm-Weller equation with Born correction assuming an inter-particle distance of 6.5 Å [55] and an ion radius of 3.25 Å.

A	E_{00} / eV	τ_A / ns	$\boldsymbol{E_{1/2}^{red}}$ / V vs. SCE, ACN[b]	$\boldsymbol{E_{1/2}^{ox}}$ / V vs. SCE, ACN[b]	$-\Delta G^0$ (ε_s = 13) / eV
DMAnt	3.07	13.0[a]	-1.98	+0.95	0.28
MAnt	3.20	5.8[a]	-1.97	+0.96	0.47
Ant	3.29	5.3[a]	-1.95	+1.16	0.58
D	E_{00} / eV	τ_D / ns	$\boldsymbol{E_{1/2}^{red}}$ / V vs. SCE, ACN[b]	$\boldsymbol{E_{1/2}^{ox}}$ / V vs. SCE, ACN[b]	
DMA	-	-	-	+0.81	
DEA	-	-	-	+0.76	

[a] lifetime measured in acetonitrile (ACN)

[b] acetonitrile (ACN)

2-[4-(dimethylamino)phenyl]ethyl 10-[9-(10-methyl)anthryl]decyl ether (Mant-10-O-2-DMA) [45]**:** Mant-10-Br (0.65 g, 1.58 mmole) and 2-[(4-dimethylamino)phenyl]ethanol (0.56 g, 3.39 mmole) were added to solution of 0.57 g NaH 60% oil suspension in *N,N*-dimethylacetamide (15 ml) and the mixture was stirred for 4h in an ice bath at 0 ^{0}C. The resulting mixture was extracted by benzene (3×15 ml). The benzene layer was washed by cold water (3×20 ml) and then dried over $MgSO_4$ overnight. The solvent was removed in vacuo. The product was isolated by column chromatography on Silica gel with *n*-hexane and *n*-hexane-ethyl acetate (95:5) mixture as eluting solvent systems to obtain Mant-10-O-2-DMA (0.25 g, 38% yield). Formula: $C_{35}H_{45}ON$, Mp: 55-56 ^{0}C. The ^{1}H, ^{13}C-NMR and mass spectra are shown in appendix A.2. ^{1}H-NMR ($CDCl_3$, MHz) δ = 8.6-7.4 ppm (8H, anthracene ring), 7.2-6.7 (4H, benzene ring), 3.7-3.5 (4H, -CH_2-O-), 3.45 (2H, -CH_2-DMA), 3.1 (3H, CH_3-anthracene), 2.95 (6H, $(CH_3)_2$N-), 2.8 (2H, -CH_2-anthracene), 2.0-1.2 (16H, chain). MS (EI) *m/z* 495.35 (M^+, 100).

Other chain-linked acceptor/donor pairs with different chain lengths (Mant-*n*-O-2-DMA, *n* = 6, 8, 16) are prepared in the same procedure: Mant-6-O-2-DMA ($C_{31}H_{37}ON$, Mp: 49-50 ^{0}C); Mant-8-O-2-DMA ($C_{33}H_{41}ON$, Mp: 71-72 ^{0}C); Mant-16-O-2-DMA ($C_{41}H_{57}ON$, Mp: 53-54 ^{0}C). The ^{1}H, ^{13}C-NMR, mass spectra of these compounds are shown in appendix A.2. For synthesis of Mant-16-O-2-DMA compound, the starting material of 1,16-dibromohexadecane (1,16-DBHD) is not commercially available. 1,16-DBHD was synthesized by the following procedure [69]: To a stirred solution of *N*-bromosuccinimide (2.75 g, 15.45 mmole) in 50 ml of tetrahydrofuran (THF) at 0 ^{0}C, a solution of triphenylphosphine (4.06 g, 14.59 mmole) in 50 ml of THF was added dropwise. After reaching room temperature a solution of hexadecane-1,16-diol (1.0 g, 3.87 mmole) in 10 ml of THF was also added dropwise. The mixture is heated at 55 ^{0}C for 2.5h. The solvent was evaporated under vacuum. Water was added to the residue and the solution was extracted with diethyl ether. The organic layer was washed with water, dried with $MgSO_4$, filtrated and then concentrated in vacuo. Silica gel chromatography of the resulting solid with *n*-heptane as eluent gives 1,16-dibromohexadecane (0.82 g, 55% yield) as a white solid. Mp: 56-57 ^{0}C. 1,16-DBHD was used in the next steps.

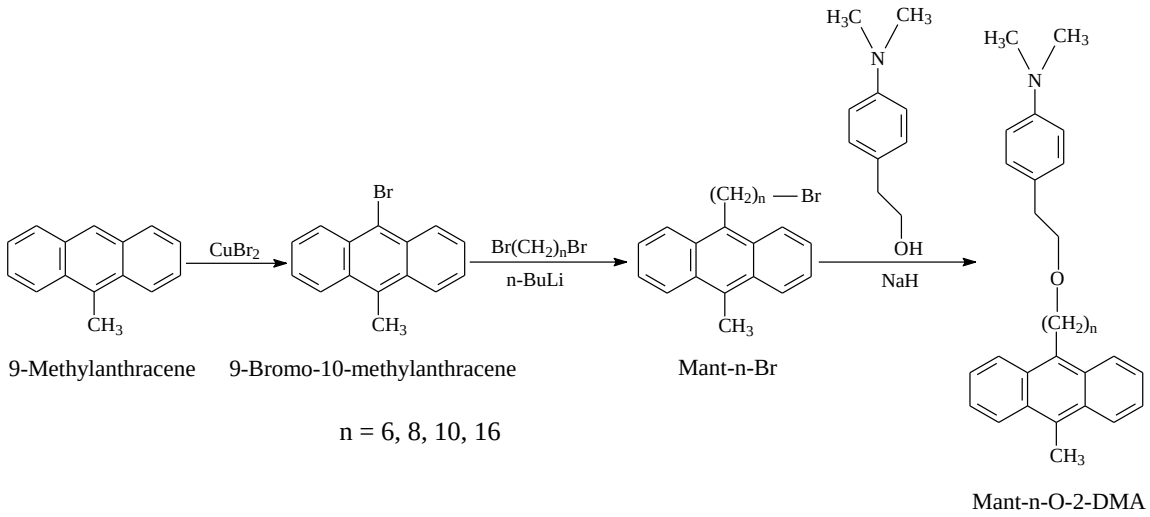

Scheme 3.1. The synthesis of the polymethylene-linked acceptor/donor systems.

Table 3.2. Chemicals used in the synthetic steps of the polymethylene-linked acceptor/donor systems. Abbreviations: Mant: 9-methylanthracene, 1,6-DBH: 1,6-dibromohexane, 1,8-DBO: 1,8-dibromooctane, 1,10-DBD: 1,10-dibromodecane, 1,16-HDDO: 1,16-hexadecanediol, DMAPE: 2-[(4-dimethylamino)phenyl]ethanol. Supplier and purification are indicated.

Chemicals	Supplier	Purification
Mant	Aldrich (99%)	as received
1,6-DBH	Aldrich (96%)	as received
1,8-DBO	Aldrich (98%)	as received
1,10-DBD	Aldrich (98%)	as received
1,16-HDDO	Aldrich (97%)	as received
DMAPE	Aldrich (99%)	as received

3.2. Solvents

During this work micro-homogeneous solvent mixtures were used. The homogeneity is due to the difference in dielectric constants and the mutual miscibility of the two components in

binary solvent mixtures [30, 31]. The three macroscopic solvent properties of main interest in the presented studies are: the viscosity, η, the refractive index, n, and the static dielectric constant, ε_s. All solvents used, their macroscopic properties of interest and their purification are summarized in Table 3.3. Series of mixture of propyl acetate (PA) and butyronitrile (BN) with varying dielectric constant, ε_s, in a range from 6 to 24.7. The dielectric constant was calculated from: $\varepsilon(w_1) = w_1\varepsilon_1 + (1 - w_1)\varepsilon_2$ with w_i and ε_i denoting the weight fraction and dielectric constant of component *i* [30, 31, 36]. In these mixtures (Table 3.4), the viscosity (η = 0.58 cP), and thus, the diffusion coefficients are nearly constant (maximum variation of 1.2%). The refractive index (n = 1.383) is likewise almost invariant with solvent composition [30, 36]. The Pekar factor ($1/n^2 - 1/\varepsilon_s$) of PA/BN mixtures, which governs the outer-sphere electron transfer reorganization energy and, thus the rate of the ET processes, varies by only ±5% in the studied ε_s-range [1, 3]. Propionitrile (EtCN) and acetonitrile (ACN) were used to extend the solvent polarity range in intra-molecular photo-induced ET reactions.

Table 3.3. Macroscopic solvent properties are given at 25 ^{0}C: density (ρ), dielectric constant (ε_s), dynamic viscosity (η), refractive index (n). Additionally the solvent supplier and the purification methods are given. Abbreviations: PA: propyl acetate, BN: butyronitrile. ACN: acetonitrile, EtCN: propionitrile. All solvent properties were taken from reference [70].

Solvent	ρ / g mL^{-1}	ε_s	η / cP	n	Supplier	Purification
PA	0.888	6.0	0.58	1.383	Aldrich (99.5%)	distilled
BN	0.794	24.6	0.58	1.383	Fluka (99%)	distilled
ACN	0.782	36.0	0.34	1.341	Aldrich (99.8%)	distilled
EtCN	0.776	28.3	0.39	1.363	Aldrich (99.5%)	distilled

Table 3.4. The dielectric constant mixture ($\varepsilon_{s,\ mix}$), mole fraction of butyronitrile (x_{BN}), viscosity (η), refractive index (n) and Pekar factor ($\gamma = (1/n^2 - 1/\varepsilon_s)$ of PA/BN mixtures.

$\varepsilon_{s,\ mix}$	x_{BN}	η / cP	n	γ
10	0.28	0.58	1.383	0.4228
12	0.41	0.58	1.383	0.4394
14	0.52	0.58	1.383	0.4513
16	0.63	0.58	1.383	0.4603
18	0.72	0.58	1.383	0.4672
20	0.81	0.58	1.383	0.4728
22	0.89	0.58	1.383	0.4773
24.7	1.00	0.58	1.383	0.4823

3.3. Sample preparation

For inter-molecular photo-induced ET measurements, the concentration of electron donors (quenchers) was 0.06 M, while that of the electron acceptors (fluorophores) was 2.10^{-5} M. For polymethylene-linked acceptor/donor systems, the concentration of acceptor/donor pairs was 2.10^{-5} M. Samples were prepared in septa-sealed quartz cuvettes. In order to remove dissolved oxygen, all solutions of inter-systems were sparged with nitrogen gas for 15 minutes prior to addition of the quencher. The liquid quenchers were added directly through the septum using a Hamilton syringe. The solutions were sparged with nitrogen gas for 15 minutes prior to measurements.

3.4. Apparatuses and measurements

3.4.1. Absorption and fluorescence spectroscopy

Figure 3.3 depicts the fluorescence and absorption spectra of the Mant-10-O-2-DMA system. Fluorescence spectra were measured on a thermostated Jobin Yvon Fluoromax-2 spectrofluorimeter. The fluorescence measurements were kept constant at 295 K with the help

of a Haake-F3 thermostat. A theoretical model has to be employed to extract the exciplex emission [35], e.g, a sum of vibronic transitions with Gaussian band shape can be assumed [71]. Absorption spectra were recorded on a Shimadzu UV-3101-PC UV-VIS-NIR spectrometer. All absorption and fluorescence spectra of inter-systems and intra-systems Mant-*n*-O-2-DMA (*n* = 6, 8, 16) compounds are shown in appendix A.3.

3.4.2. Steady-state magnetic field effect measurements

Magnetic field effects (MFEs) on exciplexes from steady-state measurements were recorded using a thermostated cell (295 K) coupled to a Jobin Yvon FluoroMax2 fluorescence spectrometer via light guides. The magnetic field in the sample compartment was measured using a F. W. Bell Model-9200 gaussmeter. A saturating magnetic field of 62 mT was employed. The earth magnetic field and stray fields were not compensated, i.e., the ‘‘zero field’’ reading corresponds to approximately 0.08 mT. The MFEs on systems were obtained by detecting the fluorescence intensity at 550 nm (Figure 3.3) for 60 s, using a spectrometer time constant of 1 s. For each sample, fluorescence intensities were acquired alternating three times between zero and saturating magnetic field. In general, the excitation slit width was 2 nm and the emission slit width 6 nm. All fluorescence signals have been background corrected. The three repetitions were analysed independently and the experimental errors were obtained according to the method described in reference [54]. Time scans at the emission wavelength of the exciplex were used to evaluate the absolute MFE on the exciplex, χ_{SS}, given by:

$$\chi_{SS} = \frac{\bar{I}(\lambda_{em}, B_{sat}) - \bar{I}(\lambda_{em}, B_0)}{\bar{I}(\lambda_{em}, B_0) - (\bar{I}_F(\lambda_{em}, B_0) - \overline{BG}(\lambda_{em}))I_c / I_0 - \overline{BG}(\lambda_{em})} \tag{3.1}$$

Here, $\bar{I}(\lambda_{em}, B_{sat})$ and $\bar{I}(\lambda_{em}, B_0)$ are the mean intensities at λ_{em} in a saturated magnetic field, B_{sat}, and in the absent magnetic field, B_0. $\bar{I}_F(\lambda_{em}, B_0)$ is the residual emission of the locally-excited fluorophore at λ_{em} in the absence of quencher. I_c and I_0 are the fluorescence intensities in the presence and absence of quencher. I_c/I_0 is the relative intensity of the prompt emission of the fluorophore in the presence of the quencher as obtained from the fluorescence spectra decomposition and $\overline{BG}(\lambda_{em})$ is the mean background intensity.

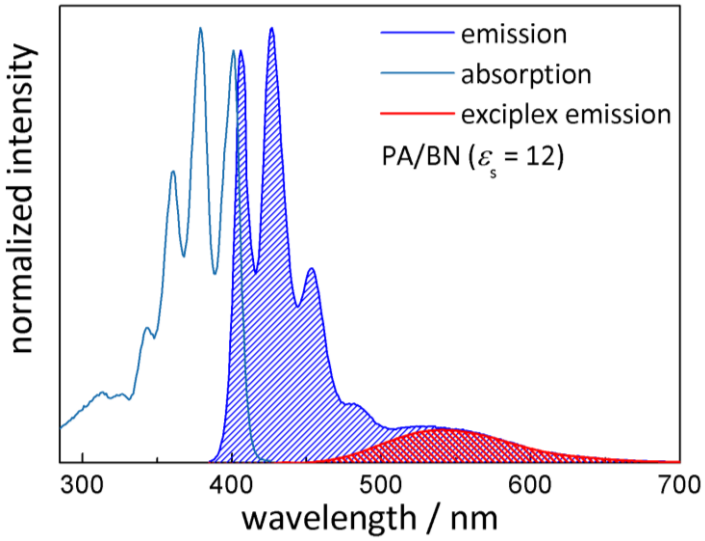

Figure 3.3. Absorption and fluorescence spectra of Mant-10-O-2-DMA in a mixture of propyl acetate/butyronitrile at ε_s = 12. The emissions of the locally excited acceptor and the exciplex are shaded in blue and red, respectively.

3.4.3. Time-resolved magnetic field effect measurements

Figure 3.4 shows the time-resolved magnetic field effect (TR-MFE) of the exciplex of Mant-16-O-2-DMA system. The TR-MFE spectra of other systems are given in appendix A.4. All TR-MFE measurements have been performed at 295 K. The time-resolved emission data of the exciplex were collected by the Time-Correlated Single Photon-Counting (TCSPC) method with the sample immersed in the magnetic field of a Bruker B-E10B8 electromagnet. The electromagnet was set to B_0 = 0 mT or 62 mT, the magnetic flux density being measured by a Hall probe placed next to the cuvette half-way between the pole pieces. The sample holder was fabricated from and thermostated by circulating. The acceptor moieties were excited at 374 nm using a picosecond diode laser (Picoquant, LDH-P-C-405, FWHM 60 ps). A 550 nm long-pass filter was placed in front of the detector to extract the exciplex emission.

The used setup is depicted in Figure 3.5. The light source is driven by an external pulse generator (Stanford Research Systems, INC, Model DG-535) with a repetition rate of 0.8 MHz. The experiment is commenced by the excitation pulse that excites the sample and triggers the time-to-amplitude converter. This signal is passed through a constant function discriminator (CFD), which accurately measures the arrival time of the pulse. This signal is passed to a time-to-amplitude converter (TAC). The arrival time of the signal is accurately determined using a second CFD. In the front of the light source, an UV-passing filter [**4**]

(UG1) was used. The intensity of the light hitting the sample was adjusted by an iris [**3**]. A prism [**5**] (triangular prism) is used to refract the pulse light, which is placed at right angle to the sample holder [**6**], where the sample is excited. The emission light from the sample is transported to the detector. The filter 550 nm [**10**] is placed in the front of PMT to get exciplex emission. A high voltage driven [**11**] photomultiplier tube **PMT** (PMT Hamamatsu, R5600-U04) was used for detecting the single-photon events. As the amplitude of the PMT output signal is only in the range of some 20 mV, a pre-amplifier [**12**] (Ortec, VT120) is used before the signal is transferred to the CFD. At TAC the information from two signal paths is evaluated and transferred to the multi-channel analyser MCA (Ortec, EASY-MCA) where a histogram of single photon events is generated. A magnet power supply [**1**] in combination with Helmholtz coils [**7**] and DC offset [**2**] have been used to adjust the magnetic field strength. On the gaussmeter [**9**], the actual field value sensed by the Hall probe [**8**] is read off.

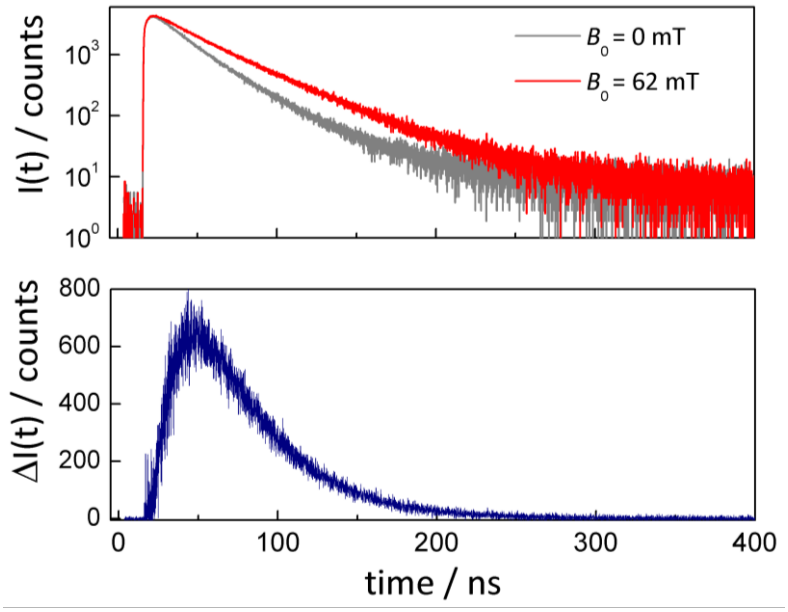

Figure 3.4. (Upper panel) Emission time trace of the Mant-16-O-2-DMA exciplex in butyronitrile (ε_s = 24.7) in the absence (gray plot) and presence (red plot) of an external magnetic field monitored with a 550 nm long-pass filter after excitation with a laser pulse at 374 nm. Time-resolved magnetic field effect of the exciplex extracted from the experimental data was shown in lower panel (blue plot).

The decay kinetics of the exciplex includes the dissociation into free ions and recombination giving rise to delayed exciplex luminescence. The difference in the exciplex fluorescence

intensity, $\Delta I(t)$, in the presence and absence a saturating external magnetic field effect is the time-resolved MFE:

$$\Delta I(t) = I(t, B_0) - I(t, B_0 = 0) \tag{3.2}$$

Here, $I(t, B_0)$ and $I(t, B_0 = 0)$ are time-dependent intensities of the exciplex in the presence and absence a saturating external magnetic field effect. Prior to making the difference according eq. (3.2), the amplitudes of two time traces have been matched within the first nanosecond after excitation, which has no significant MFE. Integrating the time-dependent intensity according to eq. (3.3) with $t_{max} \rightarrow \infty$ to determine the MFE of the exciplex, χ_{TR}:

$$\chi_{TR} = \frac{\int_0^{t_{max}} \Delta I(t)dt}{\int_0^{t_{max}} I(t, B_0 = 0)dt} \tag{3.3}$$

Here, t_{max} in the range from 200 ns to 500 ns was employed depending on the static dielectric constant.

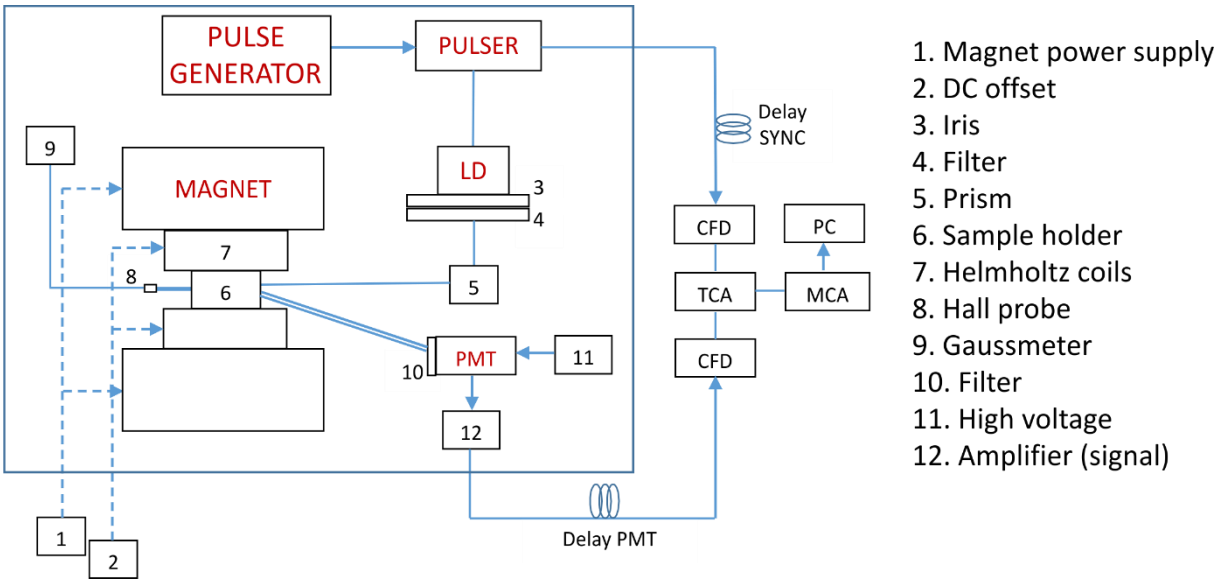

Figure 3.5. Scheme of the time-resolved magnetic field effect setup.

4. Simulations

Simulations: We have used a model which accounts for the initial quenching product and the possibility of exciplex dissociation (Figure 4.1) in the scenario of the inter- and intra-molecular electron transfer in the low-viscosity limit, for which spin and recombination are

treated independently [36]. According to this model, the probability that the system is observed in the exciplex state, ρ_E, is given as:

$$\rho_E(t, B_0) = \phi_E + \phi_I R(t|r_I, B_0) + k_d \int_0^t \rho_E(\tau) R(t-\tau|r_E, B_0) d\tau - (k_d + \tau_E^{-1}) \int_0^t \rho_E(\tau) d\tau \quad (4.1)$$

Here, r_I is the distance where the loose ion pair is formed by (distant) electron transfer, r_E the contact distance of donor and acceptor from which the exciplex is eventually formed, $R(t|r_I, B_0)$ refers to the probability that the RIP formed at t = 0 at distance r_I has recombined until t, and k_d is the exciplex dissociation rate. The first term in equation (4.1), ϕ_E = 1 - ϕ_I, is the probability that the exciplex is formed initially (path 1A in Figure 2.16), the second term denotes the probability that the RIP is formed initially and recombines forming the exciplex until t, the third term gives the probability that the exciplex dissociates with the probability $k_d \rho_E(\tau) dt$ at time τ and is reformed until t, and the last term refers to the depopulation by dissociation and radiative/non-radiative decay of the exciplex. The exciplex lifetime, τ_E, shown in Figure 5.9, has been extracted from the initial fluorescence decay. $R(t|r_I, B_0)$ depends on the singlet-probability of the radical pair and recombination function, for which a radiative boundary condition with recombination rate k_a was chosen [36].

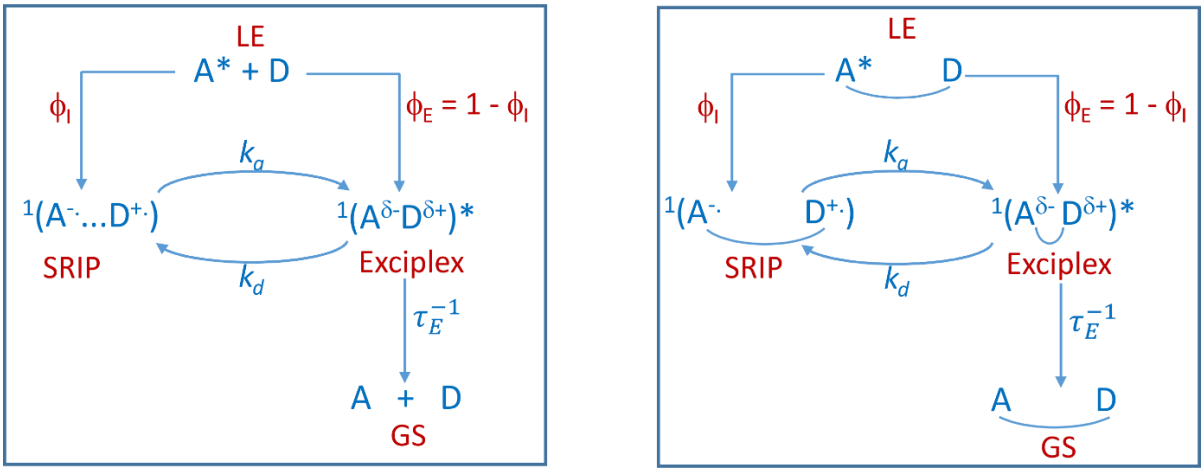

Figure 4.1: The graphic visualization of the exciplex kinetics of inter-systems (left panel) and Mant-*n*-O-2-DMA systems (right panel): ϕ_I gives the probability of the initial singlet radical ion pair (SRIP) formation while ϕ_E = 1-ϕ_I denotes the probability of the initial exciplex formation. The exciplex dissociates into the singlet radical ion pair with the rate constant, k_d, the SRIP associates into the exciplex with the rate constant, k_a and the radiative/non-radiative exciplex decay to the ground-state (GS) with the rate constant, τ_E^{-1}. LE refers to the locally-excited acceptor.

The association constant, $K_A = k_a/k_d$ (k_a is the rate of RIP association into exciplex), has been determined (besides ϕ_I and ϕ_d) to reproduce the experimental MFE in the least-squares sense. The k_d values so obtained are plotted in Figures 5.10 as a function of dielectric constant.

Simulation parameters: The time evolution of the MFE depends on the following parameters:

a) Diffusive motion

   D: diffusion coefficient (estimated from the Stokes-Einstein relation assuming a hydrodynamic radius of 3.25 Å)

   r_E: contact distance of donor and acceptor (6.5 Å)

   r_c: Onsager radius ($r_c = \frac{e_0^2}{4\pi\varepsilon_0\varepsilon_r k_B T}$) (calculated from the solvent dielectric constant)

   Hydrodynamic hindrance (the Deutch-Felderhof model has been used [20])

b) Exciplex

   τ_E: exciplex lifetime (determined from a bi-exponential fit to the initial fluorescence decay).

   $\phi_d = k_d \tau_E$: dissociation quantum yield of the exciplex

c) Radical ion pair (RIP)

   Spin evolution (calculated as described in [36] using the hyperfine coupling constants reported below)

   τ_R: radical ion pair lifetime (200 ns)

   r_I: distance where ions are generated by distant ET (7 Å was used on account of the fact that the ET is in the Marcus normal region)

   ϕ_I: initial probability of the RIP state

   $k_a = K_A k_d$: rate of RIP association into exciplex

   Most of listed parameters are either known, or can be determined in independent experimental measurements and kept constant during simulations. τ_E can be determined experimentally, and ϕ_d values obtained are close to those calculated from the dependence of τ_E on the solvent polarity.

Tables 4.1-4.5 list the hyperfine coupling constants that have been used to calculate the spin evolution of the RIP.

Table 4.1. Used hyperfine coupling constants, a_{-}^{H}, for anthracene$^{-\cdot}$ taken from [72-73].

Value / mT	-0.556	-0.274	-0.157
Type	2H	4H	4H
Position	(9, 10)	(1, 4, 5, 8)	(2, 3, 6, 7)

Table 4.2. Used hyperfine coupling constants, $|a_{-}^{H}|$, for 9-methylanthracene$^{-\cdot}$ taken from [72].

Value/ mT	0.427	0.516	0.294	0.139	0.173	0.277
Type	3H	1H	2H	2H	2H	2H
Position	(-CH_3)	(10)	(1, 8)	(2, 7)	(3, 6)	(4, 5)

Table 4. 3. Used hyperfine coupling constants, a_{-}^{H}, for 9,10-dimethylanthracene$^{-\cdot}$ taken from [72].

Value / mT	0.388	0.290	-0.152
Type	6H	4H	4H
Position	(-2CH_3)	(1, 4, 5, 8)	(2, 3, 6, 7)

Table 4.4. Used hyperfine coupling constants, a_{+}^{H}, for the radical cation of *N*,*N*-diethylaninline$^{+\cdot}$. No experimental values are available, the values below have been calculated using DFT (UB3LYB/EPRII).

Value / mT	0.9222	-0.7910	0.1922	-0.5294	0.7315	-0.0018
Type	1N	1H	2H	2H	4H	6H
Position	(N)	(4)	(3, 5)	(2, 6)	(>2CH_2)	(-2CH_3)

Table 4.5. Used hyperfine coupling constants, a_{+}^{H}, for *N*,*N*-dimethylaniline$^{+\cdot}$. No experimental values are available, the values below have been calculated using DFT (UB3LYB/EPRII).

Value / mT	0.833	-0,428	0.0868	-0.722	1.30
Type	1N	2H	2H	1H	6H
Position	(N)	(2, 6)	(3, 5)	(4)	(-2CH_3)

Calculations of the Singlet Probability / and the Recombination Function:

The singlet probability $\rho_S(t, B_0)$ is given by:

$$\rho_S(t, B_0) = Tr\left[\hat{P}_S \hat{\rho}(t, B_0)\right] \tag{4.2}$$

Where $\hat{P}_S$ refers to the singlet projection operator, *Tr* is the trace operator, and the time behavior of the spin density matrix $\hat{\rho}(t, B_0)$ is obtained from the Liouville-von-Neumann equation:

$$\frac{d\hat{\rho}}{dt} = -i\left[\hat{H}, \hat{\rho}\right] + \hat{\hat{K}}_{ex}\hat{\rho} \tag{4.3}$$

With the initial density matrix given by:

$$\hat{\rho}(t = 0) = \frac{\hat{P}_S}{Tr(\hat{\rho})} \tag{4.4}$$

In the low-viscosity approximation, the exchange interaction can be neglected, thus, the Hamiltonian $\hat{H}$ for a single radical *i* only contains contributions from the Zeeman interaction of the electron spins and the hyperfine interactions according to:

$$\hat{H}_i = g_i \mu_B B \hat{S}_{i,z} + \sum_j a_{ij} \hat{S}_i \hat{I}_{ij} \tag{4.5}$$

Since only moderate magnetic fields are employed, it is furthermore assumed that $g_1 = g_2 = 2.0023$. The influence of the exchange operator $\hat{\hat{K}}_{ex}$ accounting for degenerate electron exchange is then calculated from:

$$\hat{\hat{K}}_{ex}\hat{\rho} = \frac{1}{\tau_{ex}}\left[Tr_n(\hat{\rho}) \otimes \frac{\hat{1}}{N} - \hat{\rho}\right] \tag{4.6}$$

In this work, the spin correlation tensor approach was used to calculate the singlet probability (Figure 4.2). This approach implies a reformulation of Equations (4.3, 4.4, 4.6) which allows a more efficient numerical treatment of the problem in Hilbert space. Details can be found in references [28, 29, 74]. For the pseudo first-order self-exchange rate constant, $k_{ex} = 1/\tau_{ex}$, a value of $\tau_{ex} = 8$ ns was used in all simulations.

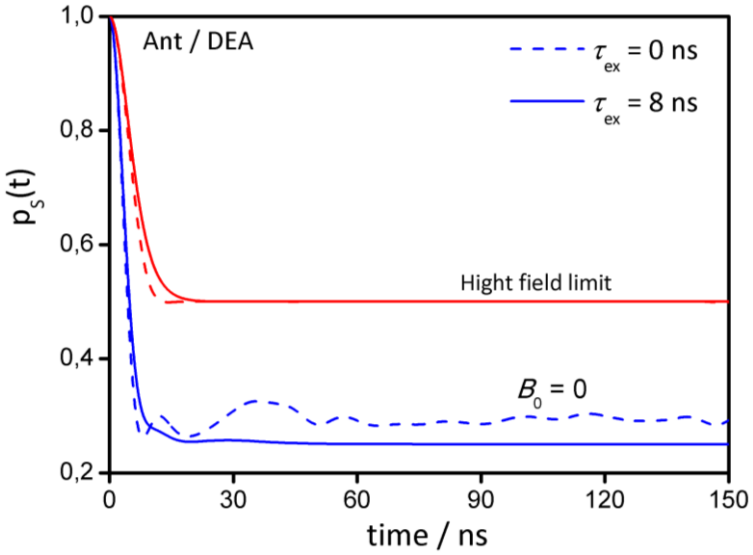

Figure 4.2. Calculated singlet probability as a function of time for anthracene/*N*,*N*-diethylaniline at zero field and high field limit. The solid lines denote $p_S(t)$ when the electron self-exchange taken into account with τ_{ex} = 8 ns whereas the dash lines show $p_S(t)$ with neglecting the electron self-exchange.

In this work a diffusion Green's function approach [21, 75] has been used to calculate the singlet yields from:

$$R(t, B_0 \mid r_I) = \int_0^t \rho_S(t, B_0)\, f(t \mid r_I) \exp\left(-\frac{t}{\tau_R}\right) dt \tag{4.7}$$

With $f(t \mid r_I)$ denoting the recombination flux, and τ_R the radical pair lifetime. The recombination flux is the defined as:

$$f(t \mid r_I) = k_a n(r_E, t \mid r_I) \tag{4.8}$$

With the time-dependence of $n(r,t)$ given by:

$$\frac{\partial n(r,t)}{\partial t} = \frac{1}{r^2}\frac{\partial}{\partial r} D(r) r^2 \exp(\frac{r}{r_c}) \frac{\partial}{\partial r} \exp(-\frac{r}{r_c}) n(r,t) \tag{4.9}$$

Where $r_c = \dfrac{e_0^2}{4\pi\varepsilon_0\varepsilon_s k_B T}$ denotes the Onsager radius. The initial condition (for instantaneous RIP generation) is taken to be:

$$n(r, t=0) = \delta(r - r_I) / 4\pi r^2 \tag{4.10}$$

and the system obeys the radiation boundary condition:

$$\left(\frac{\partial n}{\partial r} + \frac{r_c}{r^2} n - \frac{k_a}{4\pi r_E^2 D(r_E)} n \right)\Big|_{r=r_E} \tag{4.11}$$

5. RESULTS AND DISCUSSION

5.1. Magnetic field effect dependence on the static dielectric constant and chain length

Figure 5.1 depicts the magnetic field effects (MFEs) of the exciplexes of inter- and intra-donor/acceptor systems in PA/BN mixtures, propionitrile (EtCN) and acetonitrile (ACN). The MFEs were determined from the time-resolved MFE data, χ_{TR}, by integration according to eq. (3.3) in comparison to χ_{SS} determined from steady-state measurements according to eq. (3.1). Within the experimental error, the two sets of MFE agree, suggesting that all processes leading to the MFE under the experimental conditions occur on the time window (< 500 ns, see below). The agreement indicates that the bulk processes, e.g., reencounters of uncorrelated ions and processes involving fluorophore triplet do not significantly contribute to the MFE [76]. In fact, the experimental conditions have been chosen under low light intensities and low fluorophore concentrations to minimize these effects.

MFEs of the exciplexes are functions of the static dielectric constant, ε_s, of the binary solvent mixtures. For inter-systems, there is no MFE for $\varepsilon_s < 7$. For $\varepsilon_s > 7$ MFEs increase sharply and obtain the maximum value at $\varepsilon_s = 18$, followed by a monotonous decrease for $\varepsilon_s > 18$. For intra-systems (Mant-*n*-O-2-DMA), the onset of the MFE attains at $\varepsilon_s > 10$ and the maximum MFE obtains at $\varepsilon_s = 24.7$ (neat butyronitrile), followed by a decrease with increasing solvent polarity. MFEs of the exciplexes are proportional to the intersystem crossing (ISC) rate (S-T conversion) in the radical ion pairs (RIP) which produced in photo-induced electron transfer reaction. The spin evolution can only take place if component radicals in RIP diffusively separate until the exchange interaction between unpaired electrons is negligible to allow a hyperfine coupling-induced (HFC) intersystem crossing.

The solvent polarity and viscosity can affect the separation distance of the two radicals. The interaction between solvent molecules (polar components) and exciplexes, RIPs can be simplified as dipole-dipole interactions [77-78]. At low values of ε_s, the both radicals in RIP cannot diffuse to the extent of S-T degeneracy, thus ISC is unfavourable and MFE is zero. In contrast, at high ε_s values, the radical separation is sufficient, but the reencounter probability is not effective due to the prevention from the polar components (BN) in solvent mixtures.

This results in a decrease in the MFEs. At moderate polarity, there is a good compromise between radical separation and reencounter and the MFE thus is at maximum.

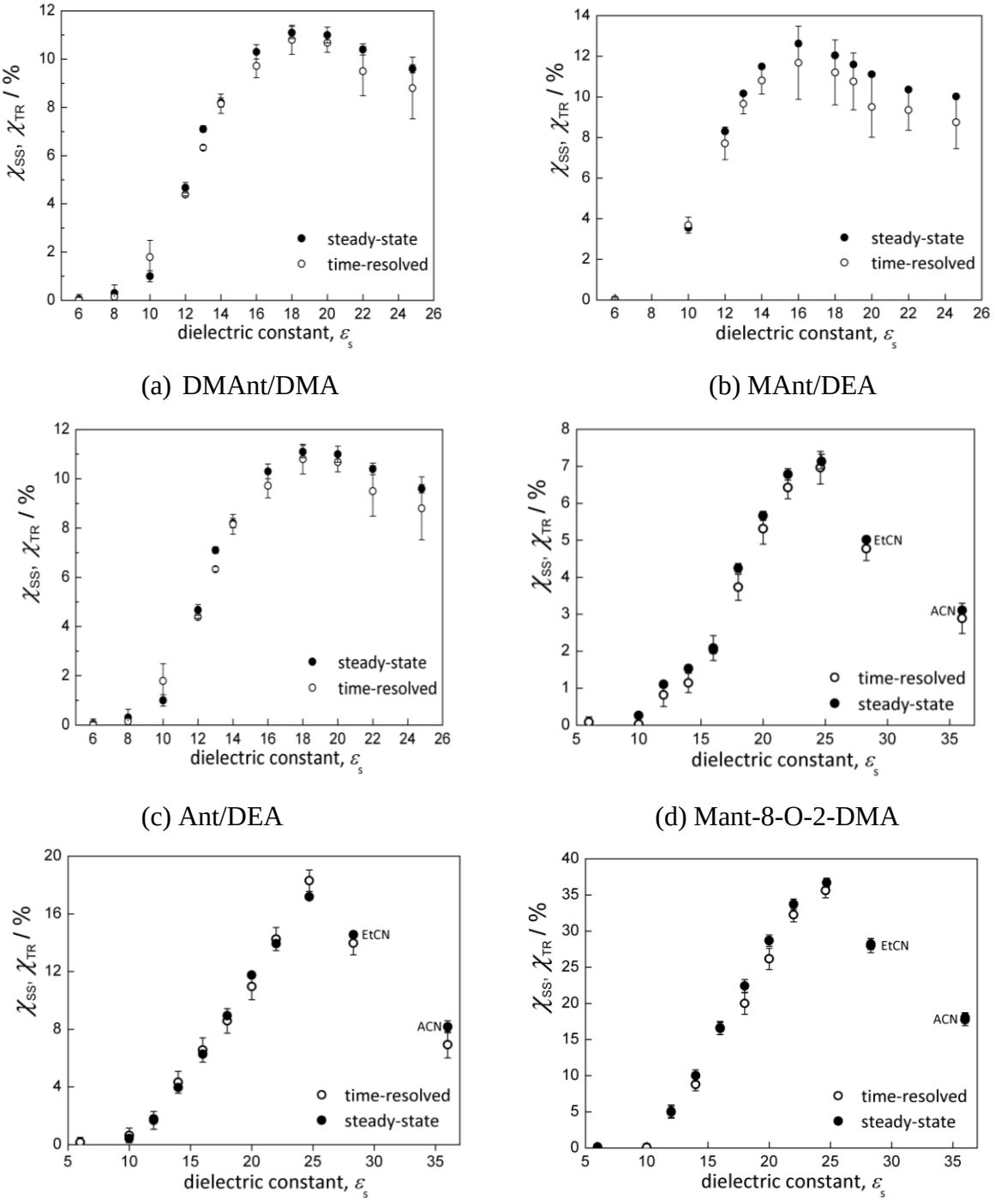

(a) DMAnt/DMA (b) MAnt/DEA

(c) Ant/DEA (d) Mant-8-O-2-DMA

(e) Mant-10-O-2-DMA (f) Mant-16-O-2-DMA

Figure 5.1. The magnetic field effects on inter-system (a-c) and Mant-*n*-O-2-DMA exciplexes (d-f) determined from TR-MFE using eq. (3.3) (filled circle with error bars) and from steady-state measurements using eq (3.1) (open circles with error bars) in propyl acetate/butyronitrile mixtures by varying the dielectric constant, ε_S. For intra-acceptor/donor systems, pure propionitrile (EtCN) and acetonitrile (ACN) are used to extend the range of solvent polarity.

The maximum MFE values in the polymethylene-linked systems with long chains are larger (χ_E = 17.8% with n = 10; χ_E = 37.5% with n = 16) than the freely diffusing systems (χ_E = 11.2%). For linked-acceptor/donor pairs, since the two radicals in RIP at the end of the chain are linked by a ‘‘bridge’’, the probability of geminate radical-pair recombination is high and MFE magnitude thus enhances significantly [33, 39, 43, 45, 79-80].

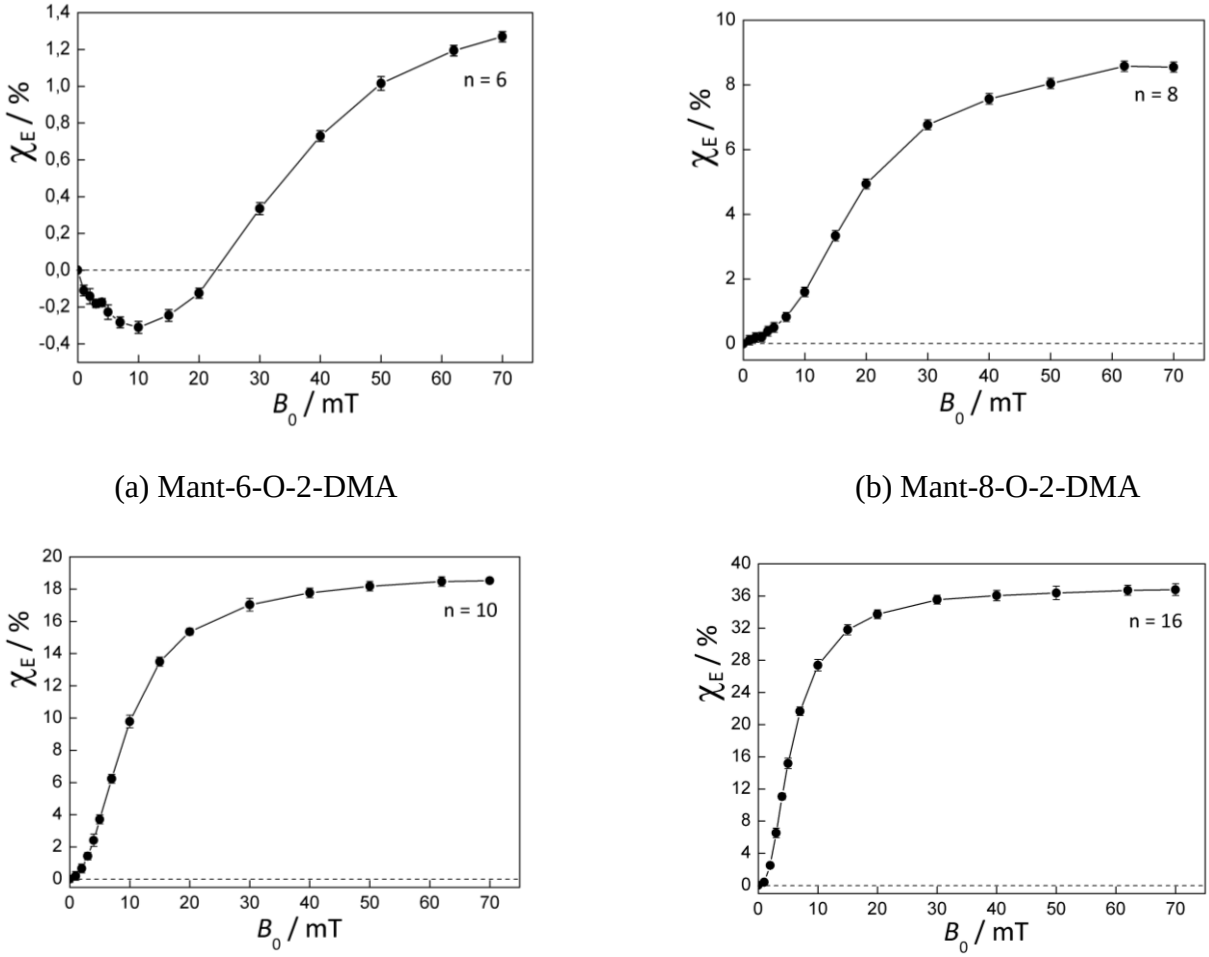

(a) Mant-6-O-2-DMA

(b) Mant-8-O-2-DMA

(c) Mant-10-O-2-DMA

(d) Mant-16-O-2-DMA

Figure 5.2. Magnetic field dependence of the exciplex fluorescence of polymethylene-linked compounds (Mant-*n*-O-2-DMA) in neat butyronitrile. The MFEs on systems were obtained in steady-state measurements by detecting the exciplex emission intensity at 550 nm for 60 s, using a spectrometer time constant of 1 s. For each χ_E value, fluorescence intensities were acquired alternating three times between zero and an external magnetic field. The data were analysed to extract the χ_E values by using eq. (3.1).

The influence of chain length on MFE of the exciplexes for intra-acceptor/donor pairs is shown in Figure 5.2. As already noted in the theoretical consideration, at zero and low field, the singlet (S) and three triplet sates (T_+, T_0, T_-) are degenerate and hyperfine interaction (HFI) induced conversion between the singlet and three triplet states takes place. When applying an external magnetic field, the S-T conversion rate is reduced due to Zeeman interaction. T_+ and T_- states are lifted, the degeneracy of between S and T_0 states results in S-T_0 conversion. This case only works when the S-T energy gap is zero, i.e. the exchange interaction J(r) (eq. (2.44)) between two unpaired electrons is negligible. The J(r) value assumed is negative as usual, a positive value is suggested for some RIPs [81]. The exchange interaction decays exponentially with the distance between two radicals, r. In the free systems, two radicals in a RIP generated via photo-induced ET can separate freely to the region where the exchange interaction is negligible. However, in the case of RIP generated by intramolecular photo-induced ET, two radicals are linked by a "bridge". They cannot separate freely because of steric restriction.

When the chain length is short (n = 6), J(r) value increases with decreasing r value, leading to a large S-T energy gap, HFI induced intersystem crossing (ISC) between S and $T_{\pm,0}$ does not work at zero field (Figure 5.3) and a decrease MFE when separation distance, r, is small. In the case of short chain (n = 6), by applying an external magnetic field (B_0 < 22 mT), the energy level of the T_- state shifts to a lower energy, S and T_- states become degenerate and S-T_- conversion takes place. This crossing leads to a negative MFE as a dip in the exciplex fluorescence intensity as shown in Figure 5.2-a

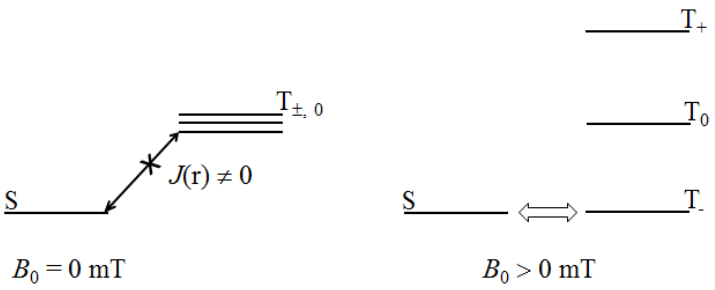

Figure 5.3. Graphic visualization of S-T conversion in the zero field and an external field (B_0 < 22 mT) for the linked-system of Mant-6-O-2-DMA.

In the case of the compounds with n = 8, 10, 16, S and T states are nearly degenerate at zero field, i.e., the exchange interaction is negligible and MFEs can be simply explained by hyperfine coupling mechanism.

The $B_{1/2}$ value, the magnetic field strength at which the delayed exciplex fluorescence reaches half its saturation value compared to zero field, is calculated by using the hyperfine-coupling constants (A_i) of two radicals forming the RIP and can be estimated by eq. (5.1) [82]:

$$B_{1/2} = \frac{2(A_1^2 + A_2^2)}{A_1 + A_2} \tag{5.1}$$

With $A_i = \sqrt{\sum_k a_{ik}^2 I_{ik}(I_{ik}+1)}$ where a_{ik} and I_{ik} are the individual isotropic hyperfine coupling constants and nuclear spin quantum numbers of the radical *i*, respectively.

In the unlinked pair composed of 9,10-dimethylanthracene and *N*,*N*-dimethylaniline, the $B_{1/2}$ value is 5.32 mT, determined from magnetic field effect on reaction yield (MARY) experiments and closely matches the theoretical value, 5.27 mT, determined from eq. (5.1) [30-31]. In the linked systems of Mant-*n*-O-2-DMA, the $B_{1/2}$ values, determined from the plots of the magnetic field dependence of the exciplex luminescence (Figure 5.2), are 18 mT (*n* = 8), 9.5 mT (*n* = 10) and 5.6 mT (*n* = 16). The larger $B_{1/2}$ values obtained from the intramolecular radical pairs can be explained by the effect of the spin exchange interaction [83]. This effect can suppress the S-T conversion, this effect is reflected in the intra-systems with shorter length. Since the biradicals are linked by a chain, radical pair dissociation into free ions does not take place. There is a time-dependent *J*(r), i.e., the molecular motion is modulating the exchange interaction. As a consequence the S-T coherences are decaying faster and this gives rise to the larger $B_{1/2}$ values.

5.2. Magnetic field effects on the locally excited fluorophore in intra-molecular photo-induced electron transfer reactions

Figure 5.4 depicts the MFEs on the fluorophore (acceptor) moieties and the exciplex determined by wavelength-resolved MFE measurements of the Mant-*n*-O-2-DMA (*n* = 8, 10, 16) in butyronitrile. Energetic factors, in particular, the free energy gap of the exciplex and the fluorophore (Figure 2.16), determines the probability of exciplex-fluorophore reversibility. MFEs on the locally excited (LE) fluorophores have been exhibited to be significant for the systems characterised by a free energy difference up to approximately -0.35 eV [34-35]. Here, it is assumed that the free energy of charge separation of the fluorophore and exciplex of intra-systems is the same with the one of the free system (DMAnt/DMA). The

free energy difference approximated of the linked-systems is -0.34 eV in butyronitrile [34]. Thus, MFEs on the LE fluorophore are expected.

Wavelength-resolved scans in the absence and presence of a saturating external magnetic field were taken in turn of five scans under field-off (B_0 = 0 mT) and field-on (B_0 = 62 mT) conditions in each case. All acceptor moieties were excited at 378 nm. The magnitude of MFE of the LE fluorophores and exciplexes was evaluated as $\chi = I(B_0 = 62\ \text{mT})/I(B_0 = 0\ \text{mT}) - 1$. All data have been background corrected.

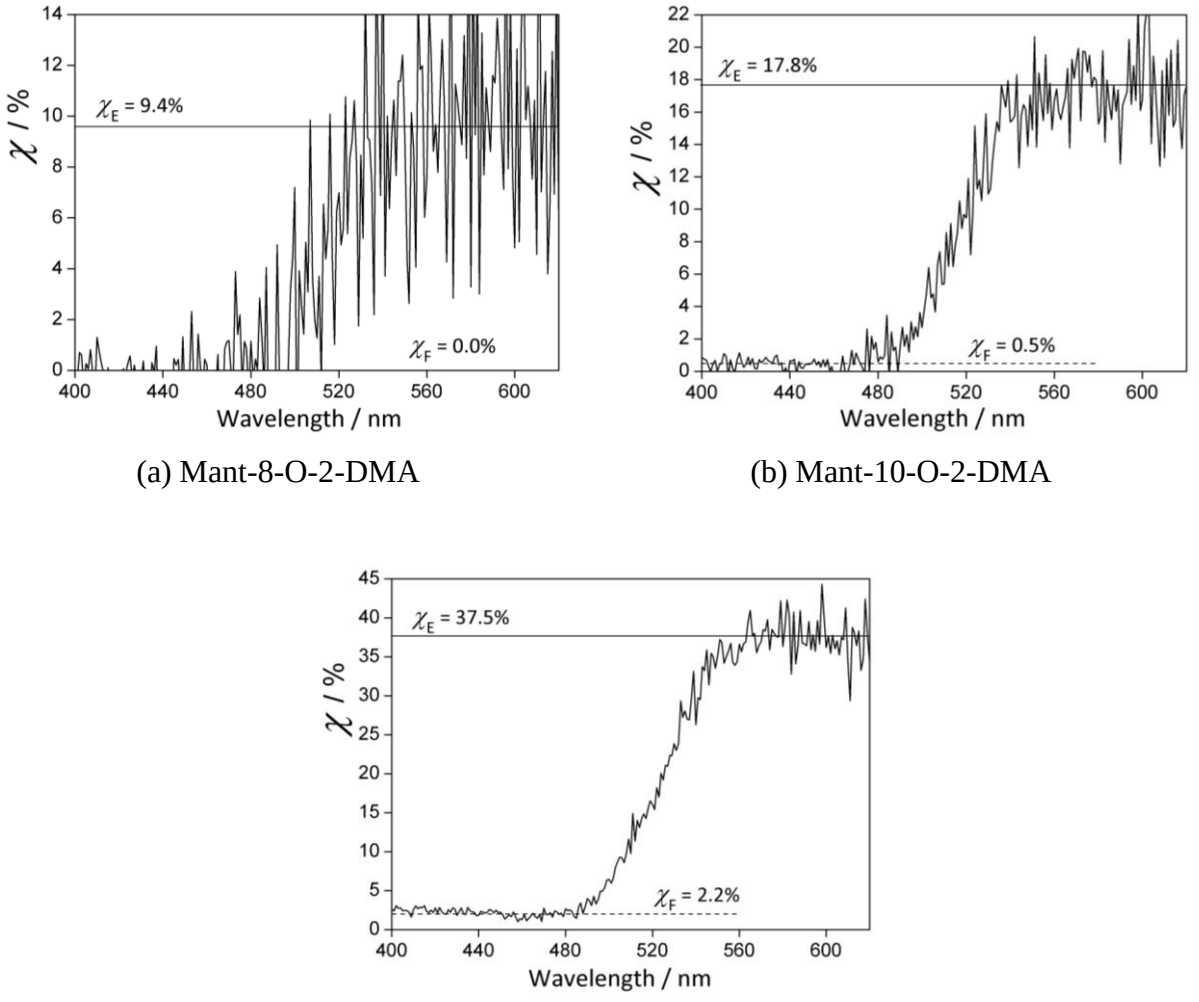

(a) Mant-8-O-2-DMA

(b) Mant-10-O-2-DMA

(c) Mant-16-O-2-DMA

Figure 5.4. Wavelength-resolved magnetic field effects of the Mant-*n*-O-2-DMA (*n* = 8, 10, 16) systems in butyronitrile. χ_F and χ_E denote the magnetic field effects on the locally-excited fluorophore and the exciplex, respectively.

MFEs on the LE fluorophore can neither be attributed to triplet-triplet annihilation (P-type delayed fluorescence) nor thermal repopulation from triplet state (E-type) [84]. The former is insignificant under the low intensity chosen in the experimental condition. The latter can be excluded because the energy gap of the singlet and triplet states is large (ΔG_{ST} = 1.3 eV) [34]. These results indicated that χ_F is due to the dissociation of the exciplex re-establishing the LE fluorophore. There is a fully reversible inter-conversion between RIP, exciplex and LE fluorophore (Figure 2.16). For the Mant-16-O-2-DMA, the MFE on the exciplex is huge (χ_E = 37.5%), the reversible inter-conversion between the exciplex and LE fluorophore is more significant (χ_F = 2.2%). The MFE on LE fluorophore of the Mant-10-O-2-DMA system is 0.5%, while that of the Mant-8-O-2-DMA system is absent.

5.3. Exciplex emission bands and Stokes shifts in binary solvent mixtures

Figure 5.5 depicts the red-shift of the exciplex fluorescence of the studied inter-systems. The free energies of exciplex formations, $-\Delta G_{EX}$, of the studied systems are listed in Table 5.1. The exciplex emission proceeds vertically giving rise to the dissociative ground state (Figure 2.16) and the energy gaps of the exciplex state and the ground state, $-\Delta G_R$, are diffent in three free A/D pairs. As a consequence the exciplex emission bands shift to longer wavelengths with less negative values of the free energy of back-electron transfer, $-\Delta G_R$.

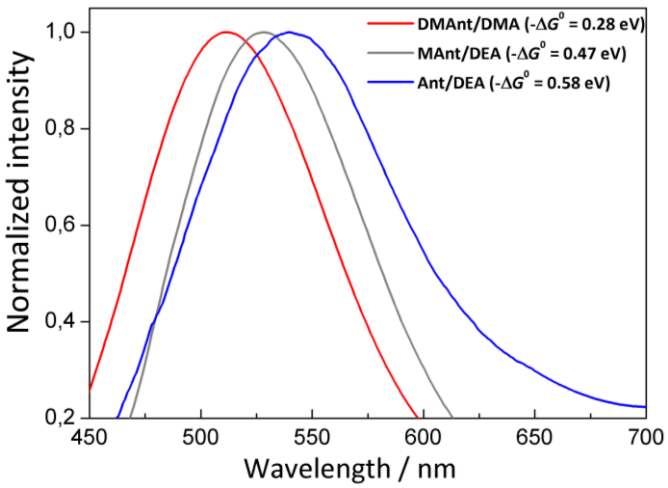

Figure 5.5. The exciplex emission bands of the studied inter-systems in propyl acetate/butyronitrile mixture at ε_s = 13.

Table 5.1. Some parameters of the studied A/D pairs at ε_s = 13 in propyl acetate/butyronitrile mixture. E_{00} is the 0-0 transition energy of acceptor; $-\Delta G_{Ex}$ refers to the free energy of exciplex formation; $-\Delta G_R$ gives the free energy of back-electron transfer; λ_{max} denotes the maximum wavelength of the exciplex emission band.

A/D	E_{00} / eV	$-\Delta G_{Ex}$ (ε_s = 13) / eV	$-\Delta G_R$ (ε_s = 13) / eV	λ_{max} / nm
DMAnt/DMA	3.07	0.28	2.79	512
MAnt/DEA	3.20	0.47	2.73	528
Ant/DEA	3.29	0.58	2.71	540

Figure 5.6 shows the wavelength shifts of the exciplex fluorescence bands with different solvent dielectric constant, ε_s, in PA/BN mixtures. There are Stokes shifts of the exciplex spectra with increasing the solvent polarity. This effect is based on the solvent relaxation properties in the excited complexes (exciplexes) [66]. In particular, the preferential solvation of polar component in binary solvent is involved in this effect [85-86]. After photo-excitation, an excited acceptor diffusively approaches an electron donor, under a well-defined relative orientation [5-9], an excited-state charge-transfer complex (exciplex) is formed. The exciplex shows a dipole moment. Polar solvent molecules in binary mixture can diffuse from the bulk to the surface of the dipolar solute molecules (exciplexes) to generate a solvent shell or polar clusters surrounding exciplex due to dipole-dipole interaction [77-78]. The concentration of polar components (BN) in solvent shell increases with increasing their mole fractions. The enrichment of polar solvent molecules in solvent shell gives rise to a difference between the effective dielectric constant around exciplex and the bulk dielectric constant. This effect is reflected in the red shifts of exciplex emission bands with increasing the mole fraction of polar components in binary mixtures.

In energetic aspect, this effect is also predicted from the solvent dielectric constant dependence of the driving force of exciplex formation, ΔG_{Ex}. The ΔG_{Ex} values of chain-linked acceptor/donor pairs are calculated as the calculation was applied for the free acceptor/donor pair of DMAnt/DMA system. The $-\Delta G_{Ex}$ ranges from 0.30 eV for ε_s = 6 to 0.34 eV for ε_s =

24.7 [34]. The driving forces of exciplex formation become slightly more negative with increasing ε_s values, i.e. the energy gap between the locally excited fluorophore (acceptor)/quencher (donor) pair and the exciplex (see Figure 2.16) is larger. As a consequence the maximum peak position of the exciplex emission to ground state is shifted to the longer wavelengths.

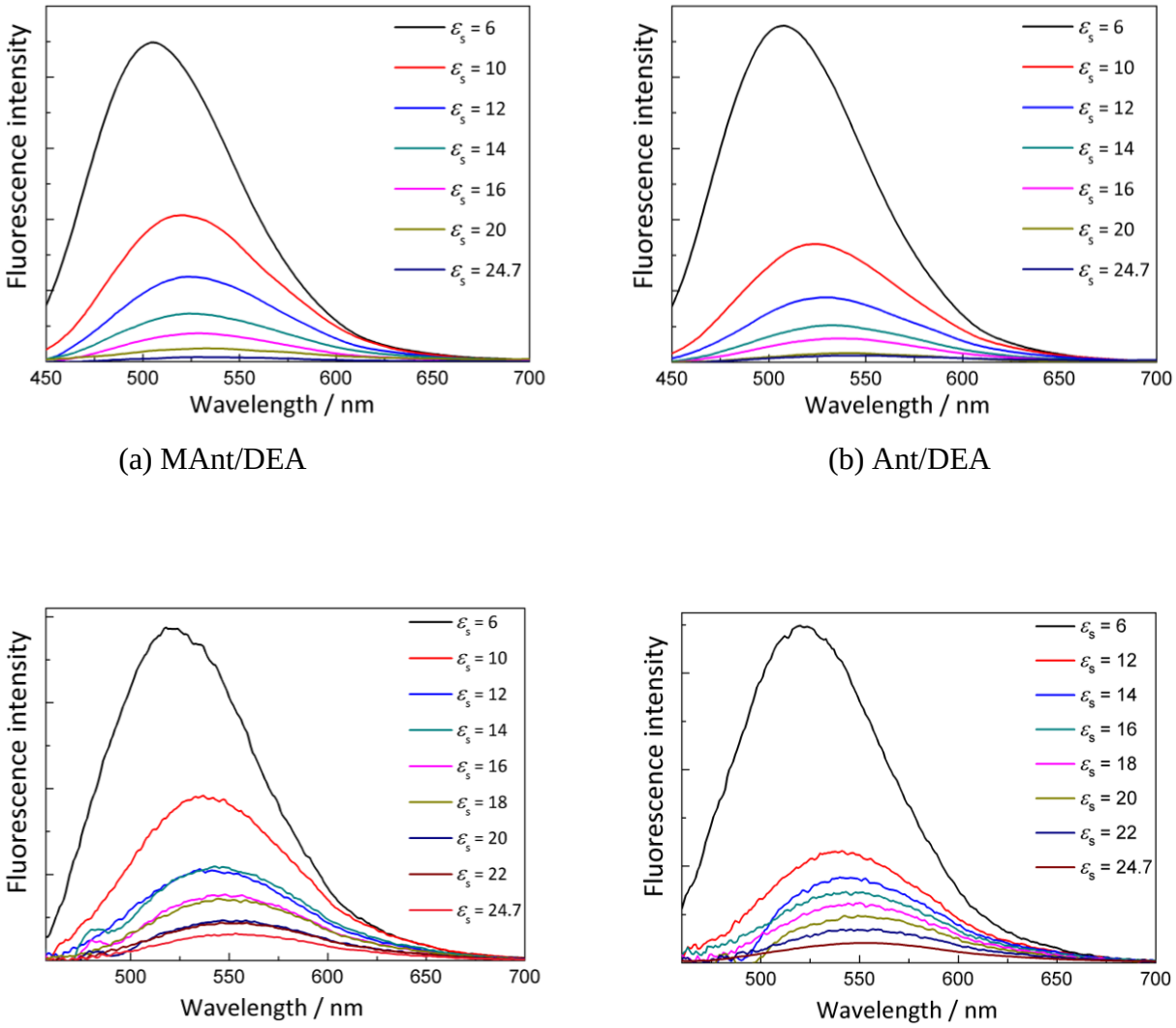

(a) MAnt/DEA

(b) Ant/DEA

(c) Mant-10-O-2-DMA

(d) Mant-16-O-2-DMA

Figure 5.6. Exciplex fluorescence spectra of inter-systems (a-b) and Mant-*n*-O-2-DMA systems (c-d) in neat propyl acetate (PA), butyronitrile (BN) and mixtures of propyl acetate/butyronitrile (PA/BN) at different dielectric constants.

5.4. The initial quenching products: Exciplexes vs loose ion pairs. Their dependence on solvent dielectric constant and electron transfer driving force in inter-molecular photo-induced electron transfer reactions

In this part, the time-resolved magnetic field effect (MFE) of the delayed exciplex luminescence was employed to distinguish the two reaction channels. This thesis focuses on the effects of the driving force, $-\Delta G^o$, and the solvent dielectric constant, ε_s, on the prevalence of the reaction channels. To this end, the different acceptor/donor systems in micro-homogeneous solvent mixtures of propyl acetate/butyronitrile of varying dielectric constant, ε_s, in the range from 6 to 24.7 were investigated. The acceptor/donor pairs 9,10-dimethylanthracene/*N*,*N*-dimethylaniline, 9-methylanthracene/*N*,*N*-diethylaniline and anthracene/*N*,*N*-diethylaniline with free energies of photo-induced ET in the range from 0.28 to 0.58 eV (at $\varepsilon_s = 13$) have been considered (Table 3.1).

As noted, the formation of RIPs via distant electron transfer or via exciplex dissociation depends strongly on the properties of the solvent and the electron transfer driving force. Figure 5.7 depicts the time-dependent MFEs at different dielectric constant in PA/BN mixtures. The maximum of the TR-MFE occurs in the range from 10 to 70 ns after excitation, with the larger values occurring at lower ε_s values. $\Delta I(t) = I(t, B_0 = 62\ mT) - I(t, B_0 = 0\ mT)$ peaks at times where the delayed fluorescence contributes significantly and the intrinsic exciplex fluorescence is low. Thereafter, the effect decays and reaches the noise level of the experiment within 500 ns. Since the exciplex dissociation is usually a slow process, the ion resulting from the exciplex dissociation will be delayed with respect to those formed by direct electron transfer. In solutions with higher polarity, the initial formation of RIP is favoured. Thus, the TR-MFE reaches its maximum at shorter times.

The primary quenching products are strongly affected by energetic parameters. The direct formation of free ions, partly at distances exceeding the contact distance, is expected to be significant for systems with larger driving force [10, 14, 20-21]. The experimental results for the DCA/durene system in acetonitrile indicated that with a free energy change of ion formation of $-\Delta G^o = 0.25$ eV, exciplexes are formed efficiently in the bimolecular quenching reaction from AD* state, whereas in the case of 2,6,9,10-tetracyanoanthracene (TCA)/pentamethylbenzene (PMB) with $-\Delta G^o = 0.75$ eV, an exciplex could not be detected [22- 23]. Exciplex fluorescence was observed for several systems in acetonitrile when the $-\Delta G^o$ is in the range from -0.28 to +0.20 eV [7-8]. Yet, full electron transfer is observed for the

vast majority of acceptor/donor system in acetonitrile [7- 8, 13, 23-24]. Figure 5.8 gives the time-dependent MFEs at different driving forces in PA/BN at ε_s = 13. The maximum of the TR-MFE occurs at shorter time-scales for the systems with a more negative driving force of ET. The direct formation of RIP via distant electron transfer is significant for system with larger driving force. Therefore, the TR-MFE reaches its maximum at shorter time-scales.

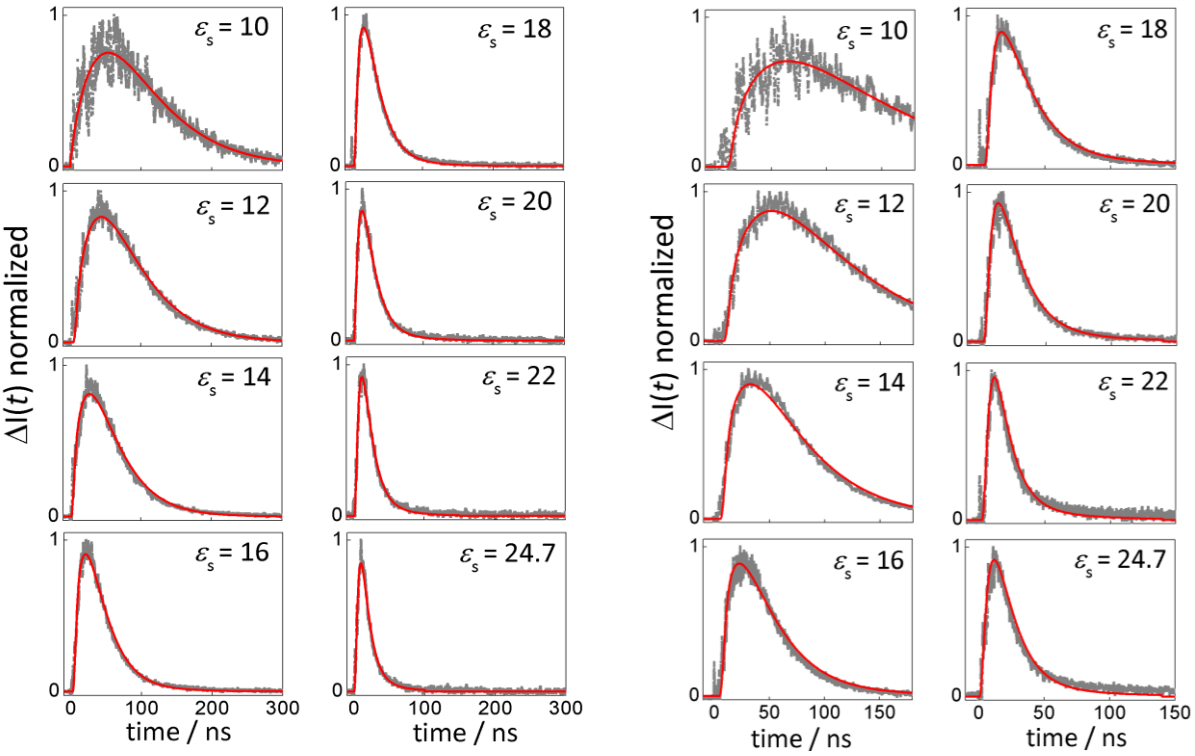

Figure 5.7. Experimental (grey scatter plots) and simulated (red solid lines) time-dependent magnetic field effects. The left column shows data for the anthracene/*N*,*N*-diethylanline system at different ε_s in propyl acetate/butyronitrile mixtures. The right column illustrates for the 9-methylanthracene/*N*,*N*-diethylaniline system.

The time evolution of the MFE depends on the parameters of the diffusive motion, the exciplex lifetime (τ_E) (see Figure 5.9), the exciplex dissociation quantum yield ($\phi_d = k_d \tau_E$, where k_d is the dissociation rate constant (see Figure 5.10), the probability that the initial states (as prepared by the quenching reaction) is a loose ion pair (ϕ_I; the probability that the initial state is the exciplex is thus 1 - ϕ_I) and the parameters governing the spin evolution (hyperfine coupling constants). Most of these parameters can be obtained from experiments or independently estimated. Making use of a model accounting for the exciplex dissociation, the spin evolution of the geminate pair, and its reencounter [36] (see eq. 4.1), the parameter ϕ_I can

be determined by fitting the experimental MFEs. Figure 5.11 depicts the dependence of the dissociation quantum yield of the exciplex, ϕ_d, and the initial probability of the loose ion pair state, ϕ_I, as function of the dielectric constants of the solvent and the ET driving force for the inter-systems studied. The ϕ_d values so obtained are close to those calculated from the dependence of τ_E on the solvent permittivity by assuming that for ε_s = 6, no exciplex dissociation occurs and that the radiative and non-radiative rates of the exciplex are constant within the polarity range studied [36] (see appendix A.5).

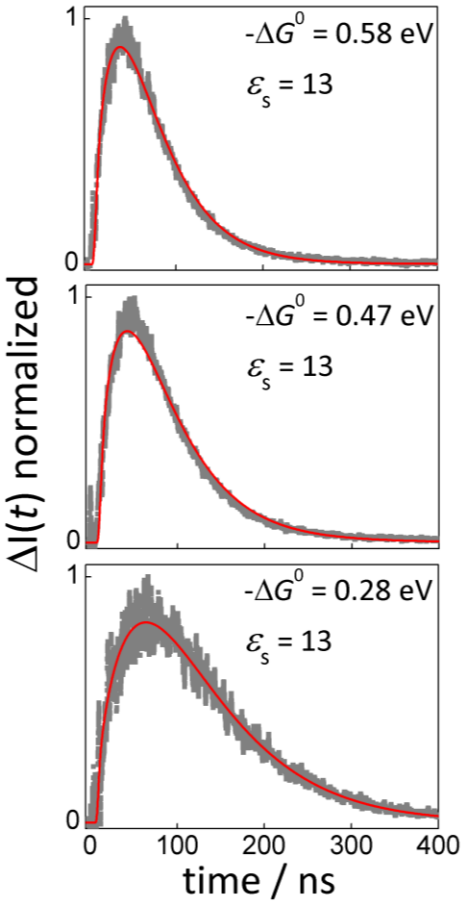

Figure 5.8. The driving force dependence of the TR-MFEs observed for the systems 9,10-dimethylanthracene/*N*,*N*-dimethylaniline ($-\Delta G^o \approx 0.28$ eV), 9-methylanthracene/*N*,*N*-diethylaniline ($-\Delta G^o \approx 0.47$ eV), and anthracene/*N*,*N*-diethylaniline ($-\Delta G^o \approx 0.58$ eV) at $\varepsilon_s = 13$. The grey scatter plots denote the experimentally time-resolved magnetic field effect data and their simulations are given as the red solid lines.

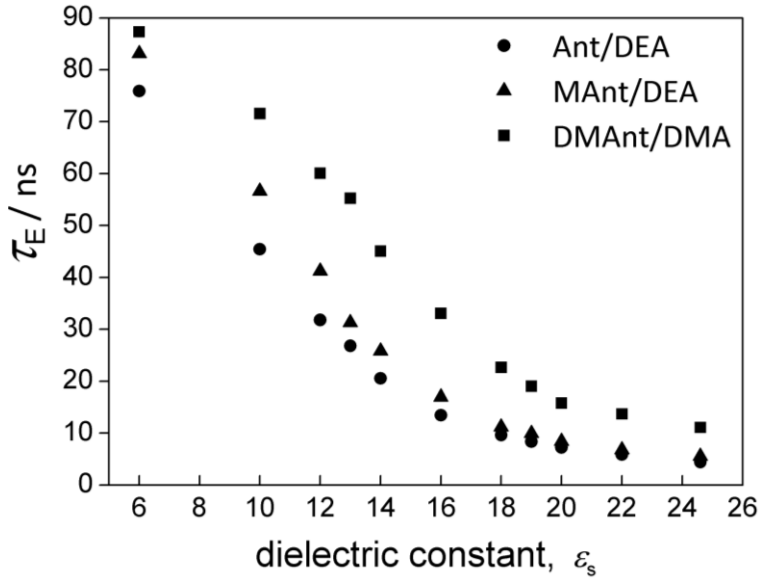

Figure 5.9. Solvent polarity dependence of the intrinsic exciplex lifetimes for the studied inter-systems.

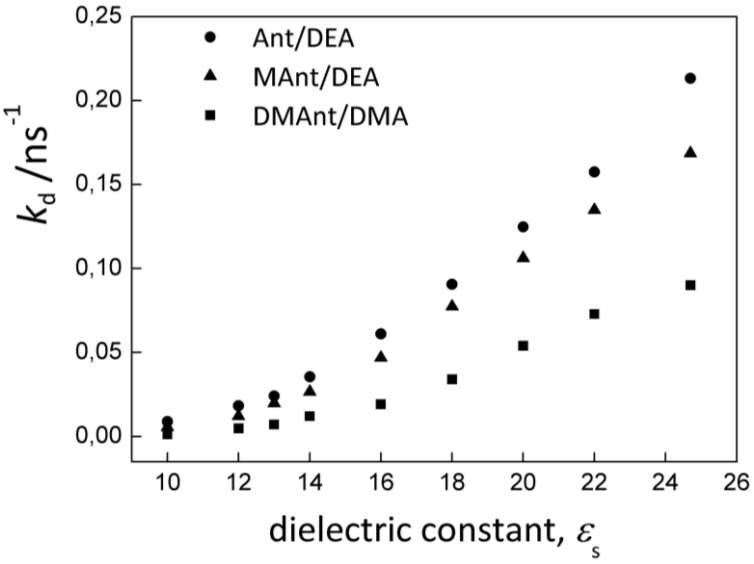

Figure 5.10. Solvent dependence of the dissociation rate constant for the studied inter-systems.

From the data summarized in Figure 5.11, we infer that the exciplex quenching channels contributes at all studied polarities, even for anthracene/*N*,*N*-diethylaniline, which exhibits the most exergonic ET among the inter-system studied ($-\Delta G^o \approx 0.58$ eV). As expected, exciplex formation is dominating at low polarities (for $\varepsilon_s < 15$) and its significance increases with decreasing ET driving force. Interestingly, however, for all system, ϕ_I levels off upon

increasing the solvent dielectric constant (for ε_s > 15) and the exciplex channel contributes significantly even in pure butyronitrile (ε_s = 24.7). ϕ_d increases with increasing polarity of the solutions. At low polarity, the exciplex formation (pathway 1A in Figure 2.16) is dominant. This is in qualitative agreement with the model introduced in ref. 35, which predicts a more stabilized exciplex at low polarity of the solvent environment – essentially a consequence of the less shielded Coulomb interaction of A^- and D^+ in low-permittivity solvents. The initial formation of the RIP is more favoured in polar solution, where the exciplex potential well is less pronounced and the excited state population partly reacts through the loose-ion pair channel prior to assuming the well-defined mutual orientation necessary for forming the exciplex.

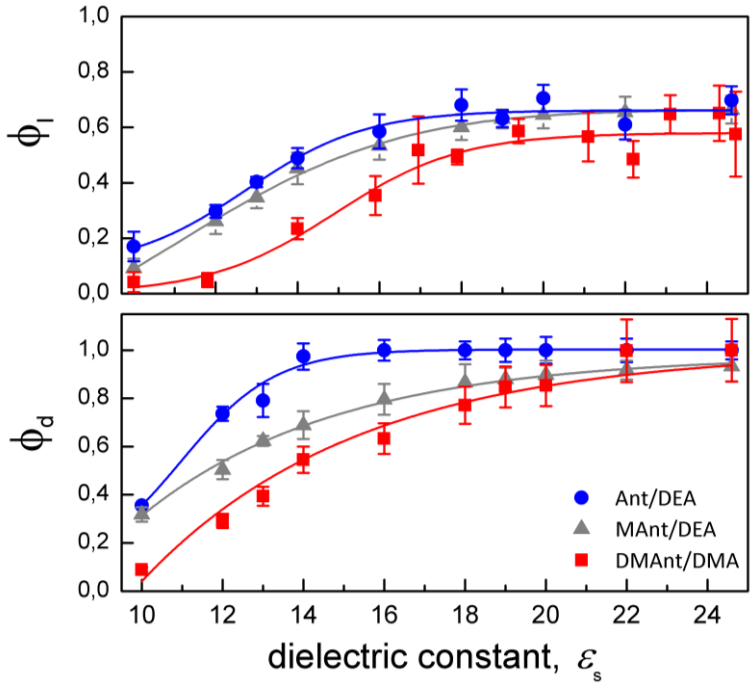

Figure 5.11. Solvent dependence of the initial probability of the loose ion pair state, ϕ_I, (upper panel) and the dissociation quantum yield of the exciplex, ϕ_d, (lower panel) of the systems 9,10-dimethylanthracene/*N*,*N*-dimethylaniline (red filled squares), 9-methylanthracene/*N*,*N*-diethylaniline (grey filled triangles), and anthracene/*N*,*N*-diethylaniline (blue filled circles) in propyl acetate/butyronitrile mixtures. The sole purpose of the solid lines is to guide the eye; no physical model is implied.

The fact that the direct formation of loose ions via full electron transfer (pathway 1B in Figure 2.16) is more significant for systems with larger ET driving forces is a consequence of the

intrinsic ET rate constants increasing with driving force in the Marcus normal region [87-88]. Yet, even for the most polar solutions and the largest driving forces studied the two types of ET reactions occur competitively. If the (long-distance) ET occurs faster than the diffusive approach of A* and D, the acceptor excited state is deactivated by full ET. On the other hand, if the diffusive approach giving rise to the favourable stacked configuration facilitating the exciplex is faster than the (more) distant ET process, the exciplex channel dominates. This also suggests that in solvents of comparable permittivity and electron transfer parameters, the loose-ion channel will gain significance with increasing solvent viscosity. Work along the lines of this supposition is underway. Apparently, for the low-viscous solvent system studied here (η = 0.58 cP independent from composition), the diffusive approach to the stacking distance is fast enough for the exciplex formation to always contribute significantly, even at ε_s ~ 20. Unfortunately, the approach detailed here cannot be easily extended to more polar solutions as a consequence of the low emissivity of the exciplexes/tight ion pairs at dielectric constants exceeding 25.

5.5. The initial quenching products: Exciplexes vs loose ion pairs. Their dependence on solvent dielectric constant and chain length of Mant-*n*-O-2-DMA systems

All polymethylene-linked compounds synthesized to investigate the fluorescence quenching mechanism in this thesis are completely new. No MFE results on these systems have been described in the literature so far. Furthermore, the hyperfine coupling constants (HFCs) used to calculate the spin evolution of the RIP have not been published yet. The experimental measurements to get the HFCs and simulations of the time-resolved MFE data are in progress.

6. CONCLUSIONS AND OUTLOOKS

6.1. Conclusions

The polymethylene-linked acceptor/donor pairs have been synthesized. The magnitude of the MFE of the exciplex of these compounds determined from steady-state and time-resolved MFE measurements is larger than that of inter-systems. This can be attributed to an increase of the probability of geminate reencounter between two radicals of RIP which generated via intra-molecular photo-induced ET.

MFE dependence on solvent polarity and chain length has been investigated. For both systems, the MFE of the exciplex is a function of the static dielectric constants, ε_s. The onset of the MFE in inter-systems is at $\varepsilon_s > 7$ while that is at $\varepsilon_s > 10$ in intra-systems. The maximum MFE of linked-acceptor/donor exciplex attains at larger ε_s value ($\varepsilon_s = 24.7$) while that appears around $\varepsilon_s = 18$ for free diffusing systems. S-T conversion is impeded when the inter-radical distance is small, i.e., the exchange interaction $J(r)$ is large. This results in a decrease in the MFE with decreasing chain length. When the chain length increases (n = 8, 10, 16), the exchange interaction is negligible. S-T conversion is similar to the inter-systems, MFE thus enhances.

By systematically varying the solvent polarity as well as the electron transfer driving forces and using a model which accounts for the initial charge transfer state and the dissociation of the exciplex, this work has been able to demonstrate that even in comparably polar solvents a significant fraction of photo-excited acceptor/donor systems deactivates via direct exciplex formation instead of full charge transfer. This conclusion has been reached based on TR-MFE data and the observation that the MFE originating from the exciplex (by dissociation into a RIP and its reencounter) lags the MFE resulting from loose ion pairs. The results can contribute to the clarification of the question whether exciplexes can contribute to the charge separation process even in polar media. This question is of relevance insofar as to date no theoretical model is known that satisfactory bridges the domains of diabatic, solvent-controlled outer-sphere electron transfer and that of exciplex formation. For the studied systems, the initial RIP probability was always markedly less than unity. At low polarities, and less negative driving force ($-\Delta G^0 \approx 0.28$ eV), fluorescence is quenched predominantly by

forming an exciplex. At higher polarity and for more exergonic charge separation processes, a RIP is the primary quenching product. Nonetheless, the exciplex formation remains important even for $-\Delta G^0 \approx 0.58$ eV and $\varepsilon_s = 24.7$. Furthermore, the direct RIP formation is slightly more significant for the system with larger ET driving force.

6.2. Outlooks

- The experimental data from time-resolved MFE measurements will be simulated by using the model in which the reversibility of RIP and exciplex is taken into account. The scenario of the mechanism of fluorescence quenching via intra-molecular photo-induced ET will be clarified.
- In this thesis, there have been left space for many more interesting experiments. For chain-linked systems, the fluorescence quenching mechanism and MFE should be measured in micro-heterogeneous binary solvents (toluene/dimethylsulfoxide). Hopefully, the preferential solvation effect will give the interesting results.
- Observation of the initial quenching products by absorption transient spectroscopy in time-scales of picosecond or femtosecond would be necessary.

A. APPENDIX

A1. Unit conversion

Energy in eV:	1 eV = 96.485 $kJmol^{-1}$ = 8065.5 cm^{-1}
Time in ns:	1 ns = 10^{-9} s
Length in Å:	1 Å = 10^{-10} m
Unimolecular rate constant in ns^{-1}:	1 ns^{-1} = 10^{9} s^{-1}

A2. ^{1}H, ^{13}C-NMR and mass spectra of Mant-*n*-O-2-DMA compounds

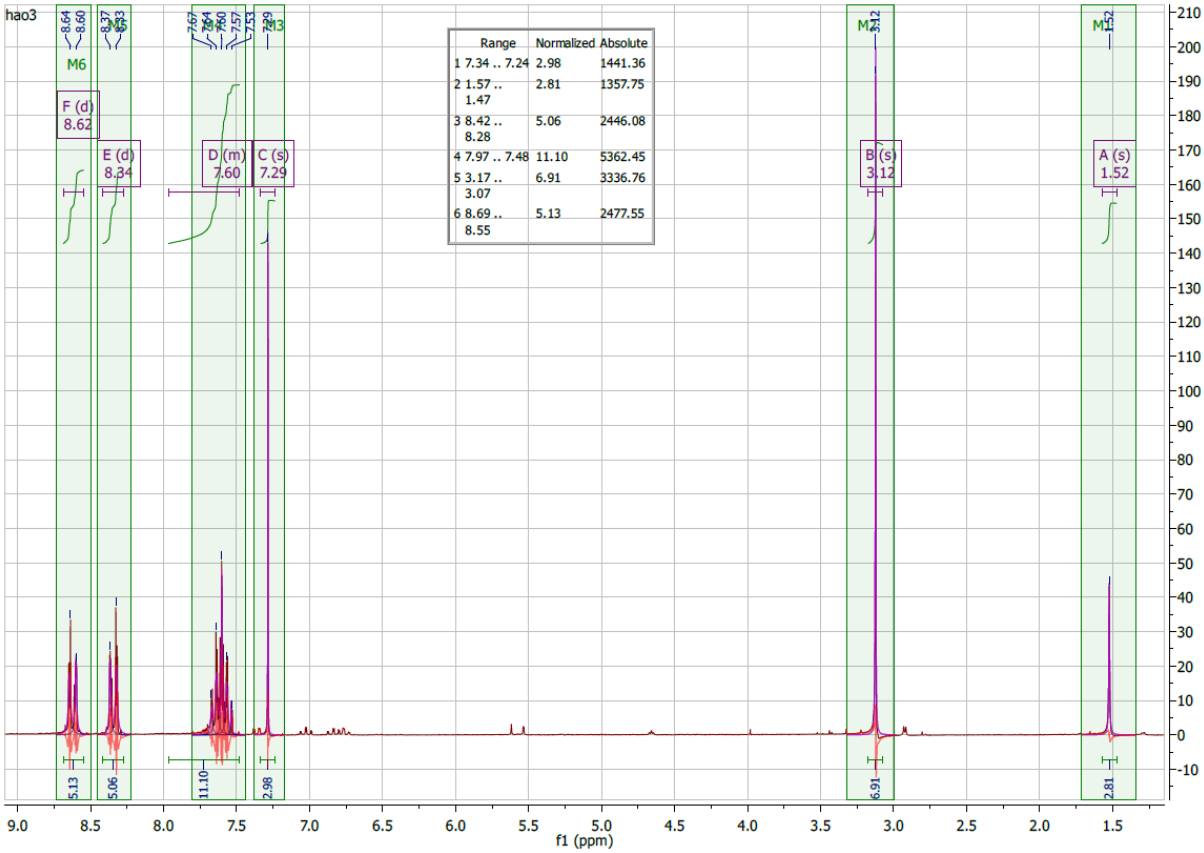

(a) ^{1}H-NMR spectrum of 9-Bromo-10-methylanthracene

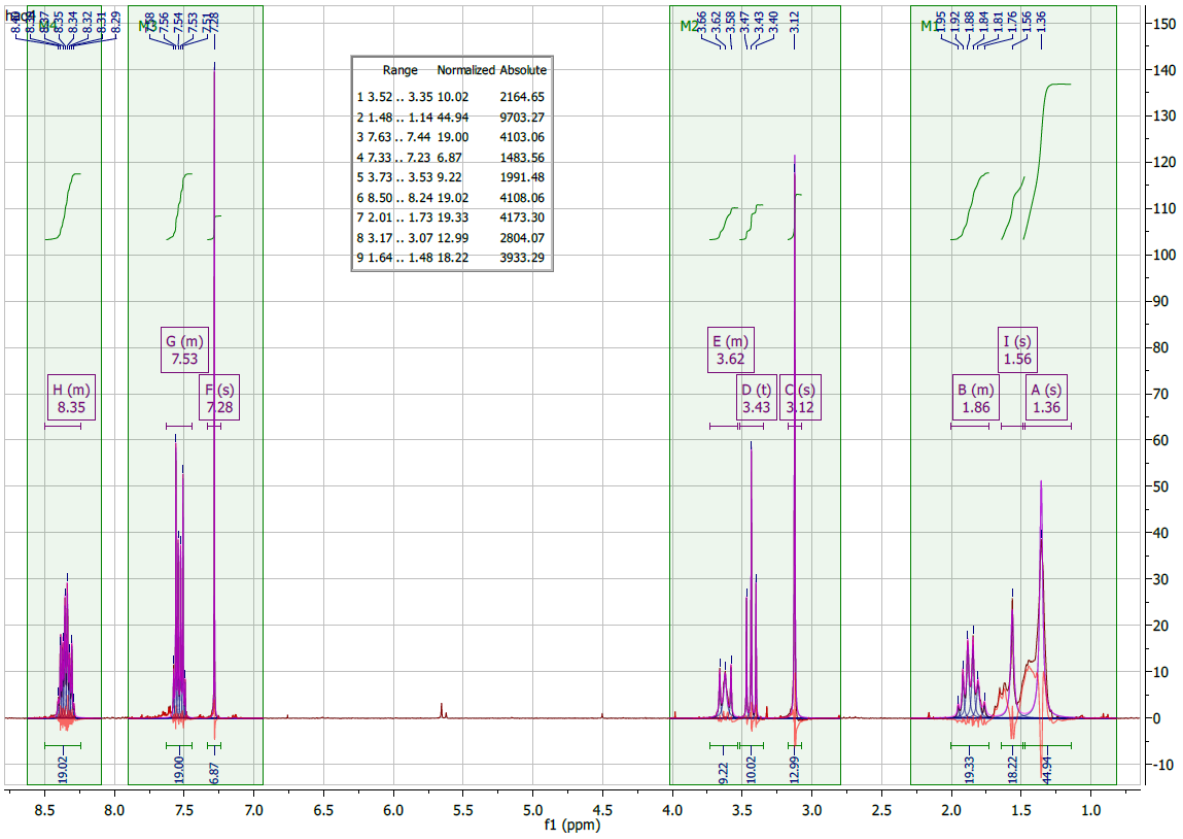

(b) [1]H-NMR spectrum of Mant-10-Br

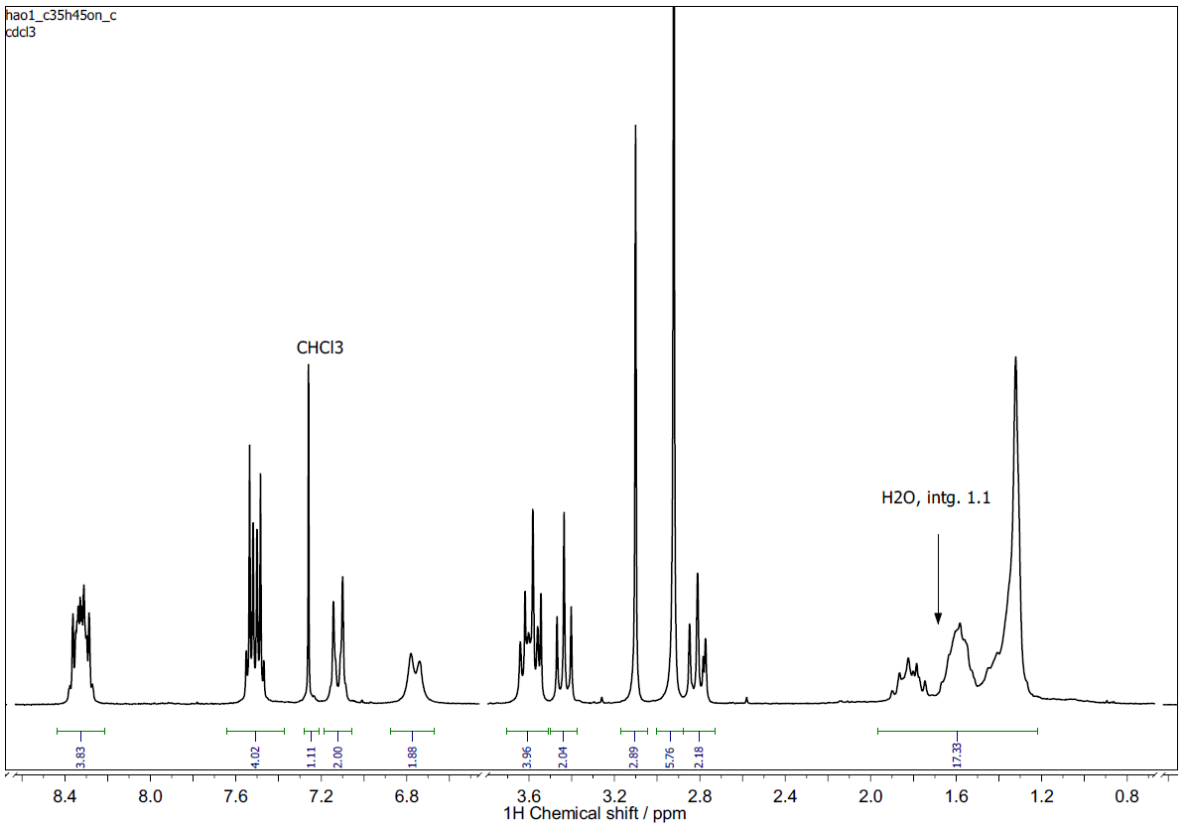

(c) [1]H-NMR spectrum of Mant-10-O-2-DMA

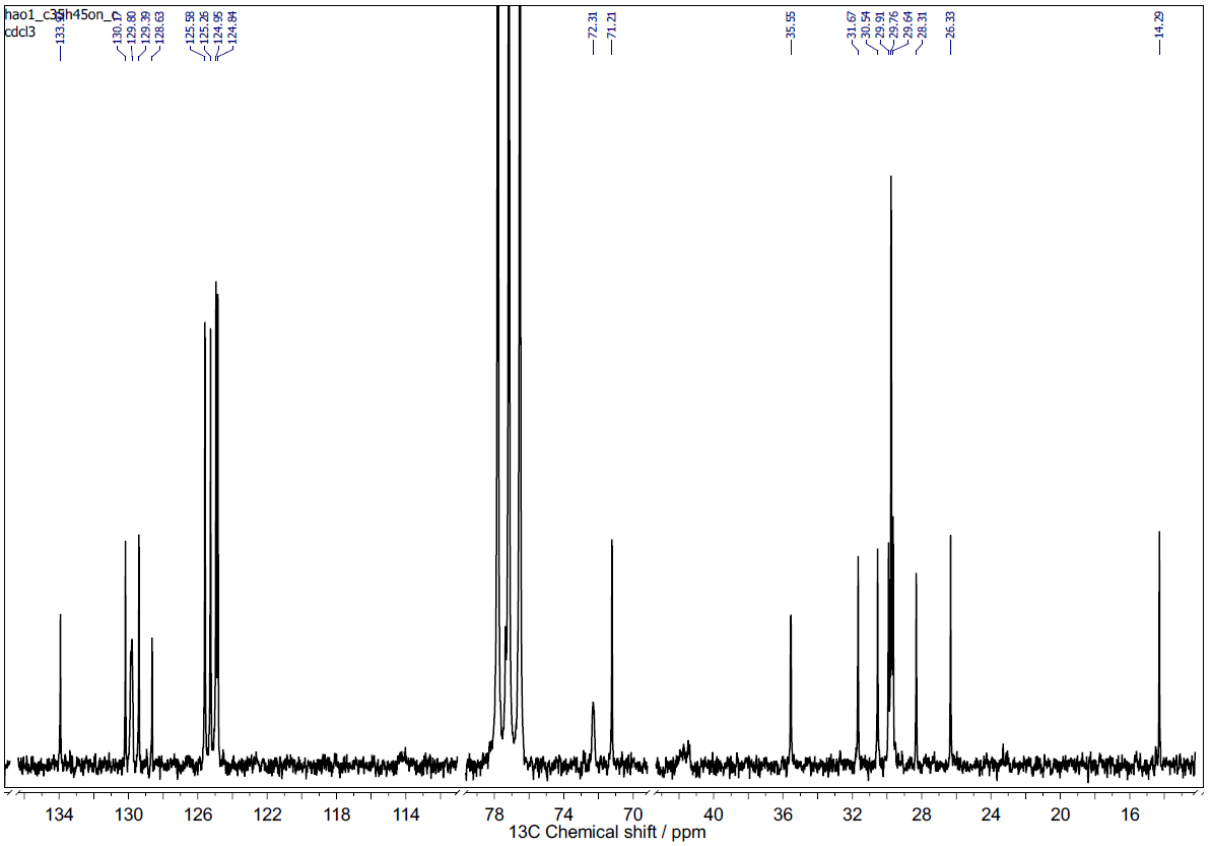

(d) ^{13}C-NMR spectrum of Mant-10-O-2-DMA

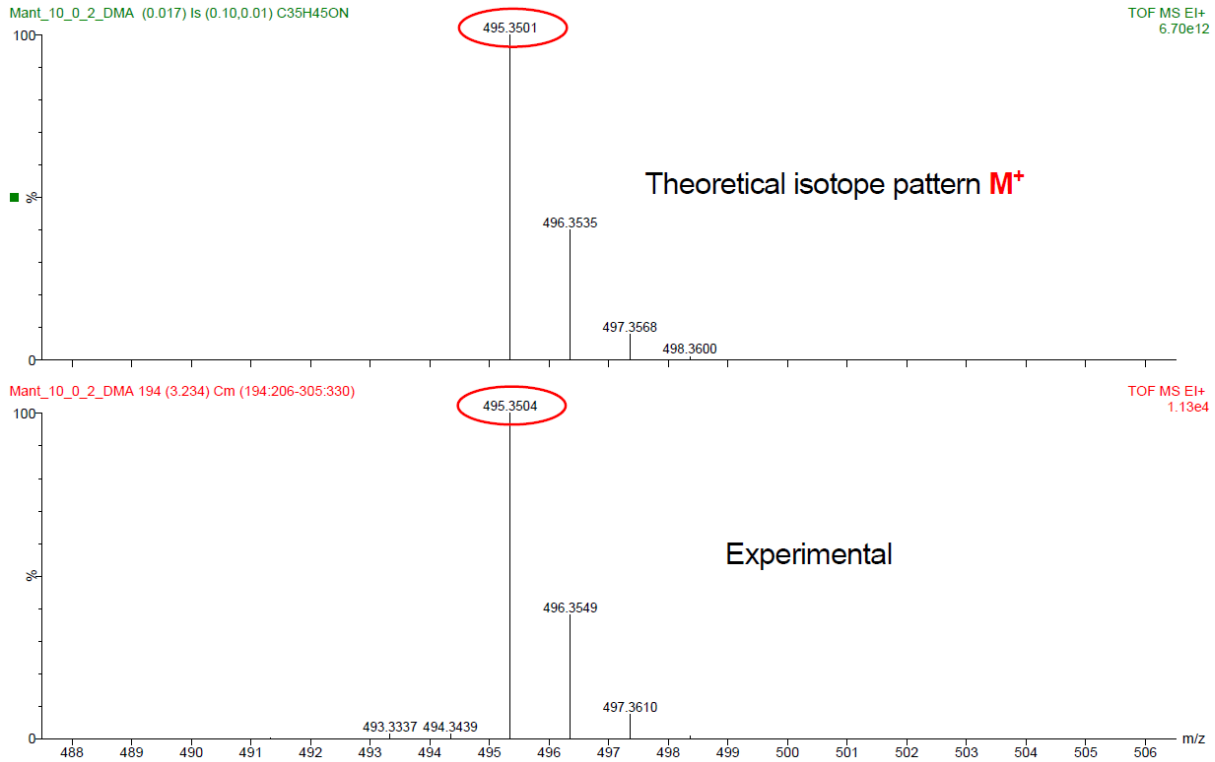

(e) Mass spectrum of Mant-10-O-2-DMA

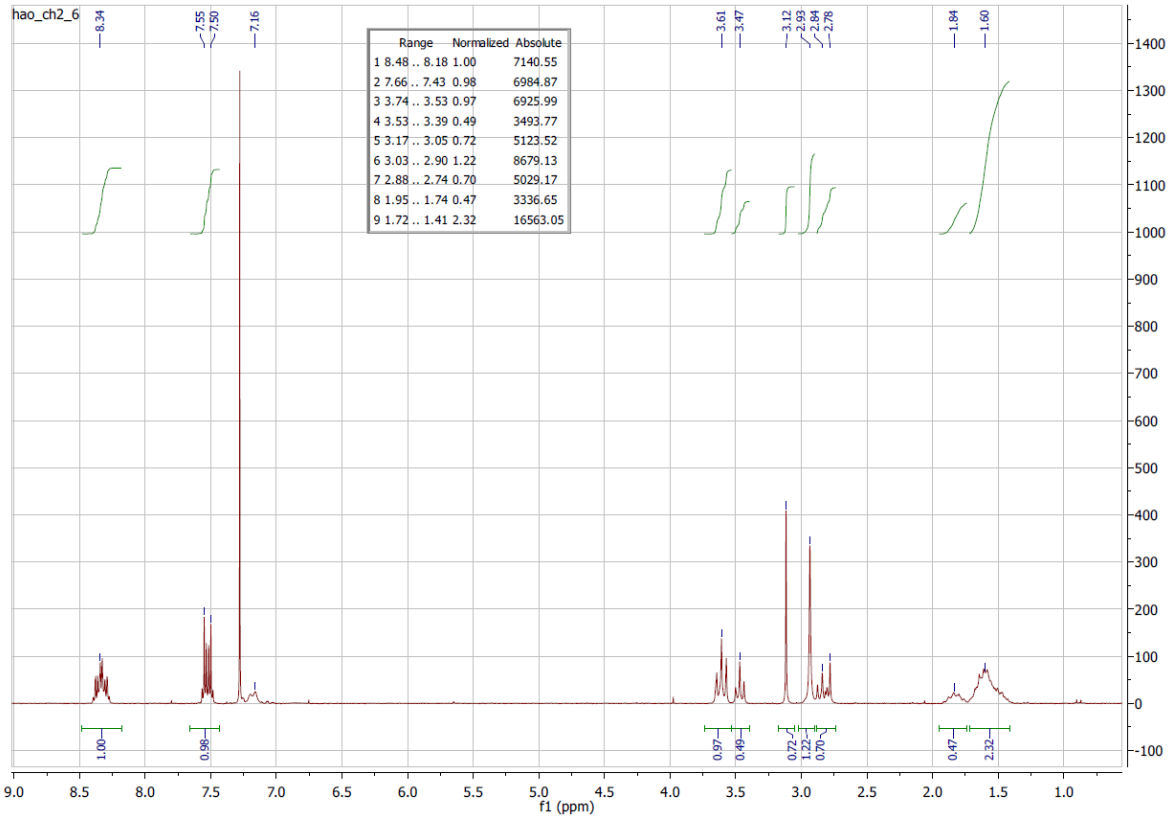

(f) ^{1}H-NMR spectrum of Mant-6-O-2-DMA

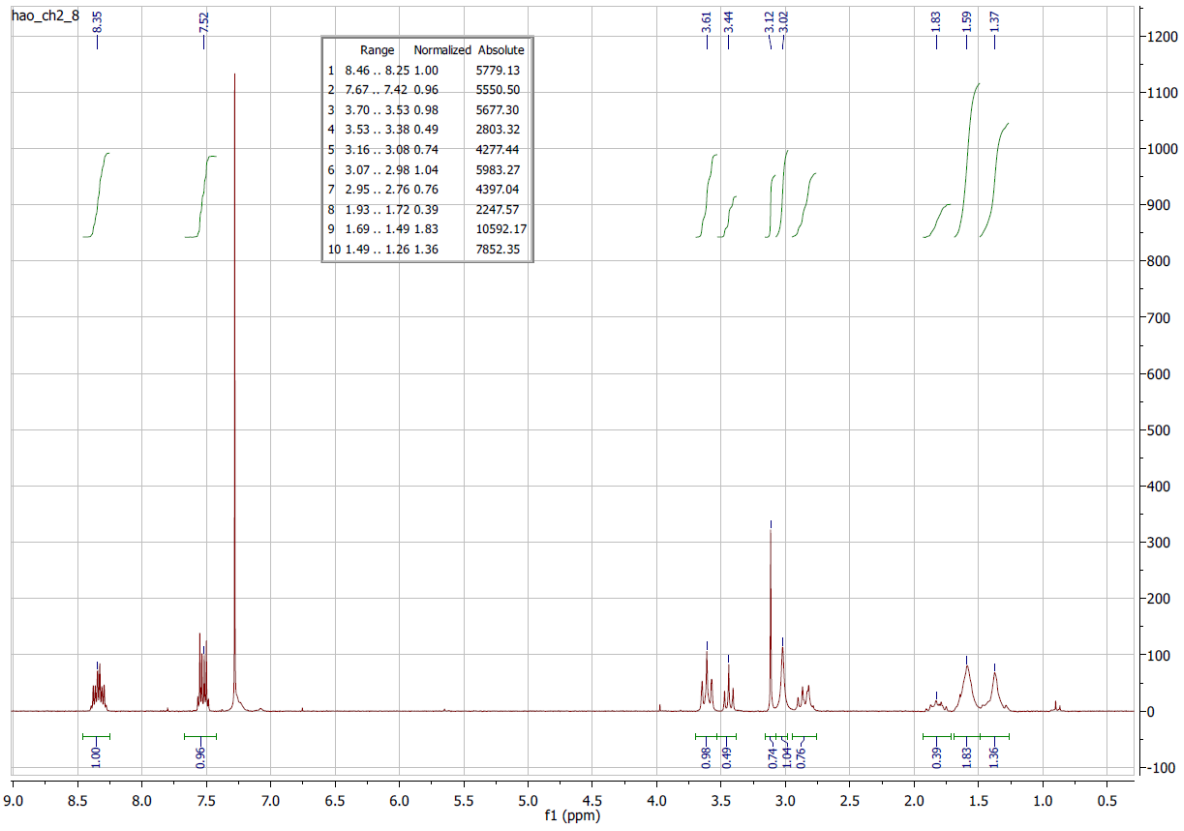

(g) ^{1}H-NMR spectrum of Mant-8-O-2-DMA

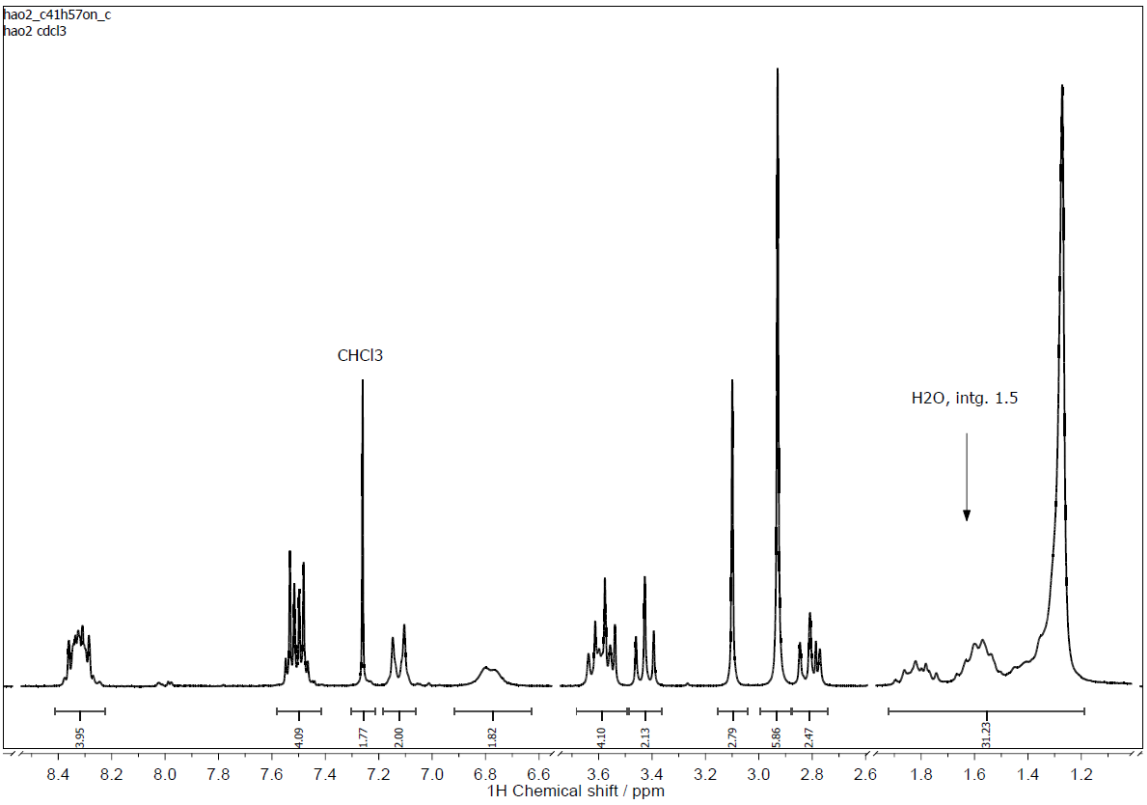

(h) ^{1}H-NMR spectrum of Mant-16-O-2-DMA

(i)

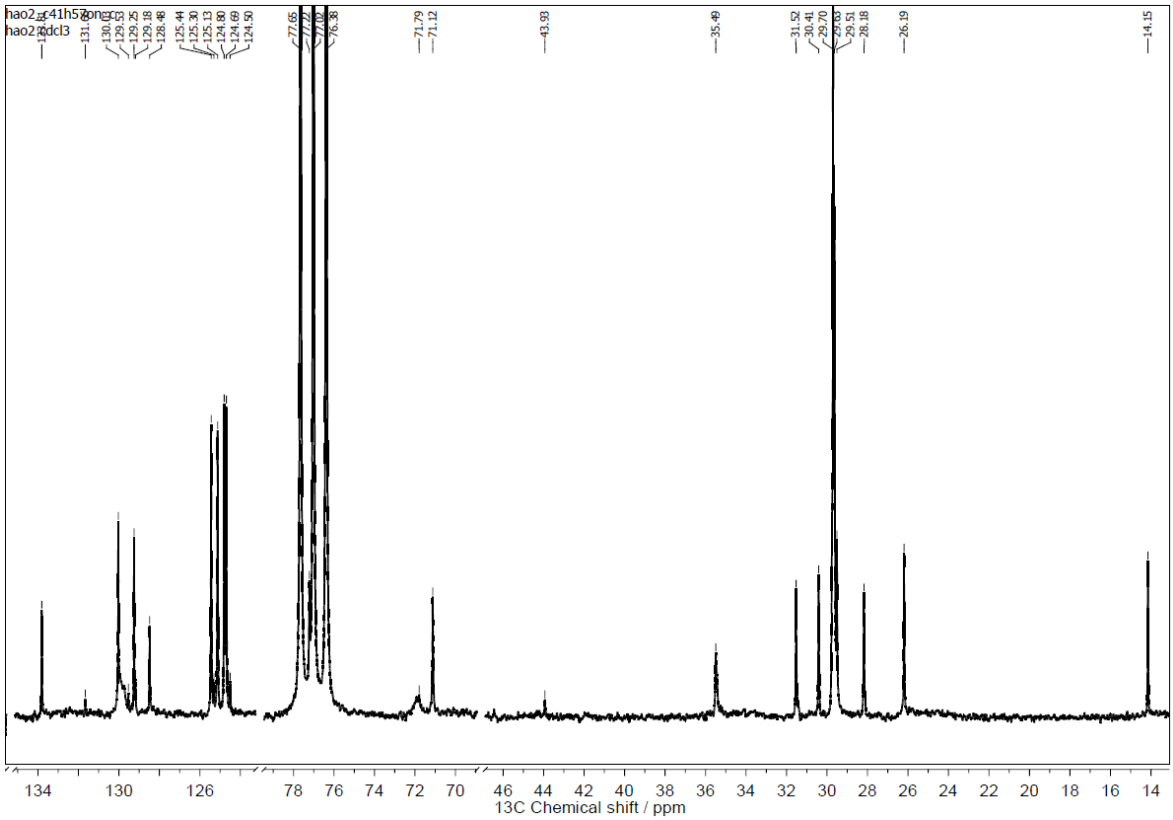

(j) ^{13}C-NMR spectrum of Mant-16-O-2-DMA

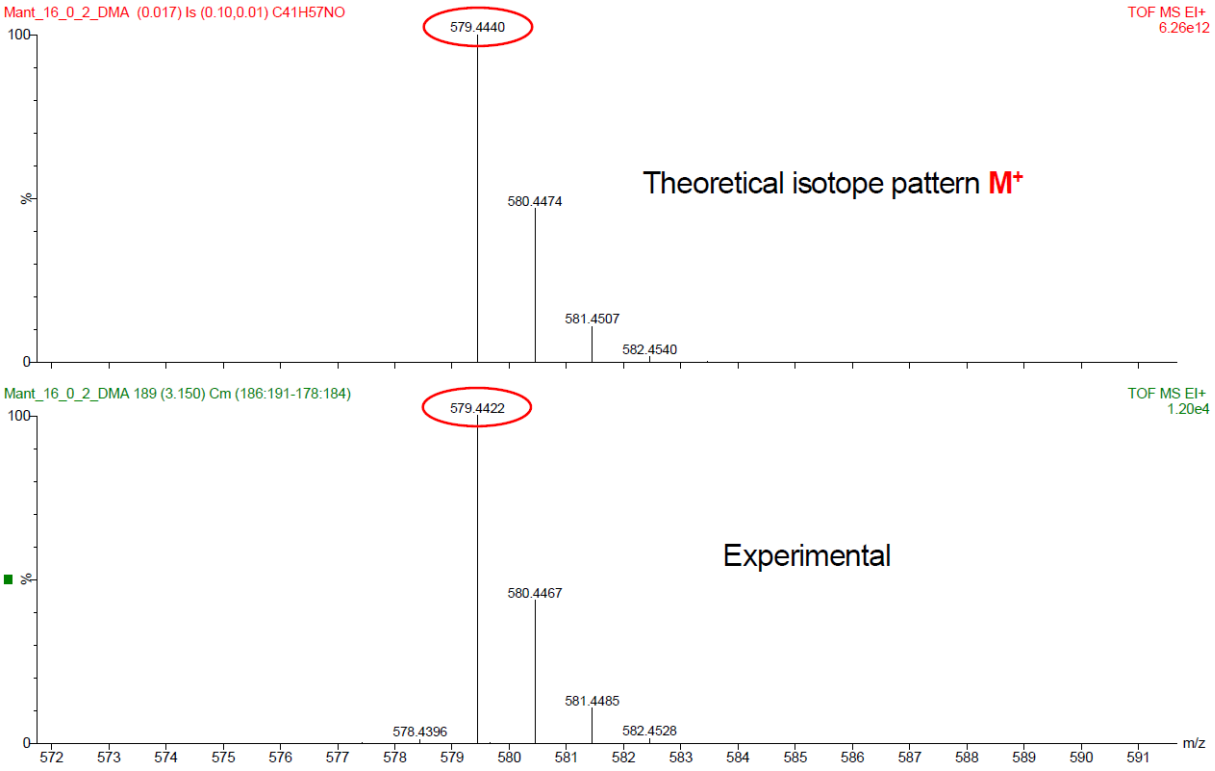

(k) Mass spectrum of Mant-16-O-2-DMA

Figure A1. ^{1}H, ^{13}C-NMR and mass spectra of Mant-*n*-O-2-DMA compounds.

A3. Absorption and fluorescence spectra of inter-systems and Mant-*n*-O-2-DMA compounds

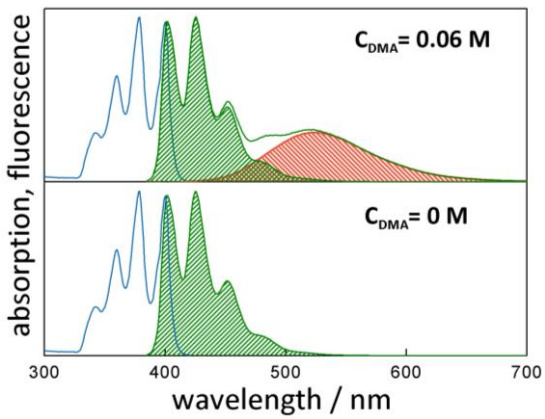

(a) DMAnt/DMA

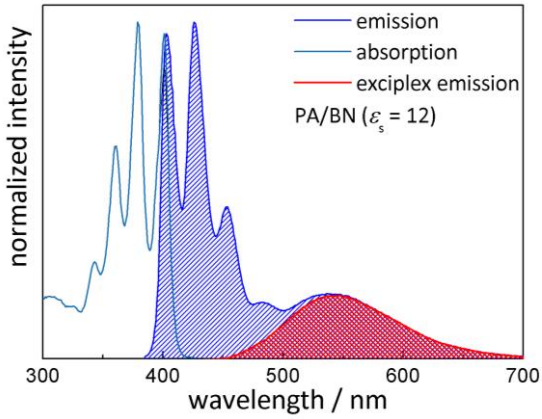

(d) Mant-6-O-2-DMA

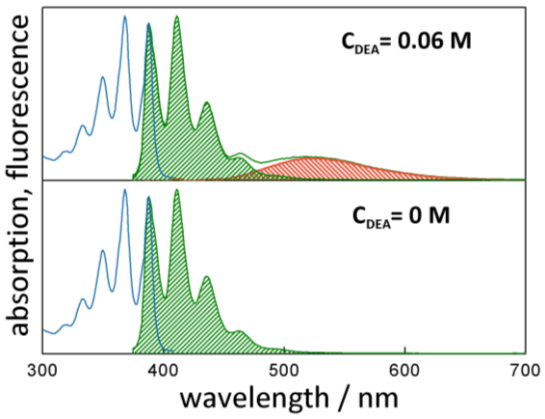

(b) MAnt/DEA

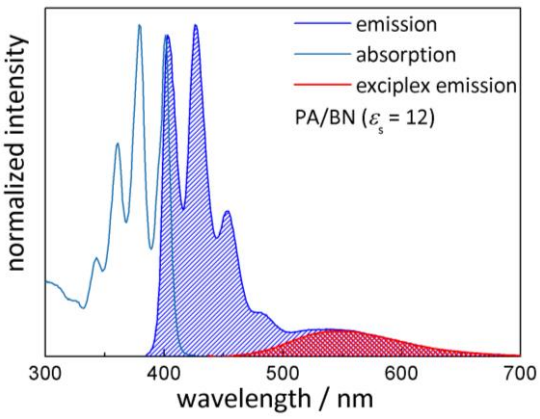

(e) Mant-8-O-2-DMA

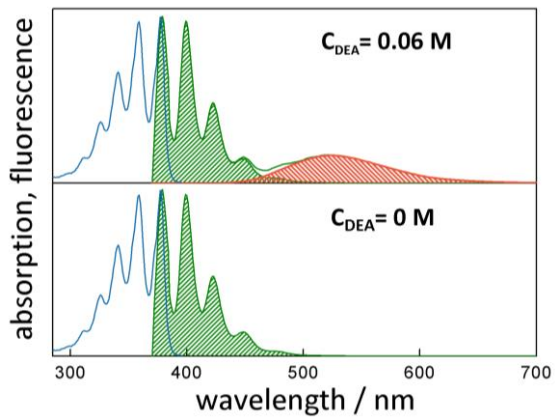

(c) Ant/DEA

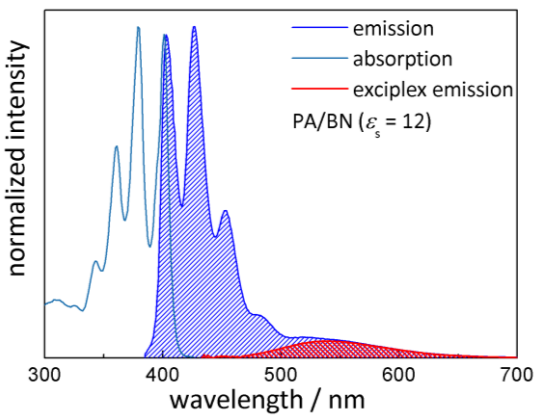

(f) Mant-16-O-2-DMA

Figure A2. Absorption and fluorescence spectra of inter-systems and Mant-*n*-O-2-DMA compounds in propyl acetate/butyronitrile mixture at ε_s = 12.

A4. Time-resolved magnetic field effects of the exciplexes of inter-systems and Mant-*n*-O-2-DMA compounds

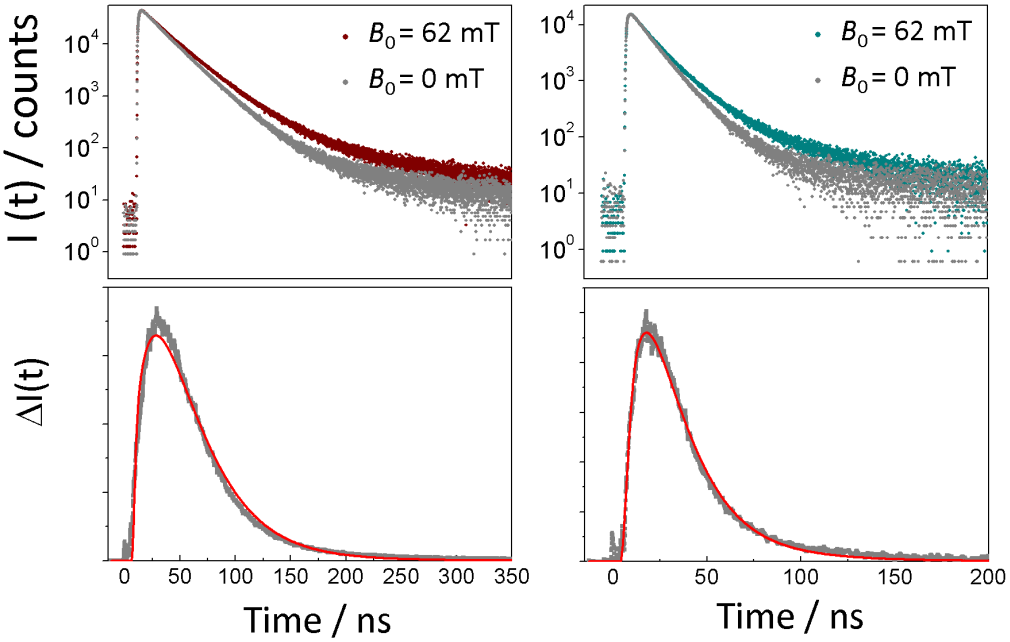

Figure A3. From right to left of upper panels: The exciplex emission decays of the DMAnt (2.10^{-5} M)/DMA (0.06 M) and MAnt (2.10^{-5} M)/DEA (0.06 M) in the absence and presence of an external magnetic field, respectively. Lower panels: Time-resolved magnetic field effects of the exciplexes extracted from the experimental data (gray scatters) and simulations (red lines). Propyl acetate/butyronitrile mixture at ε_s = 18 used as a solvent.

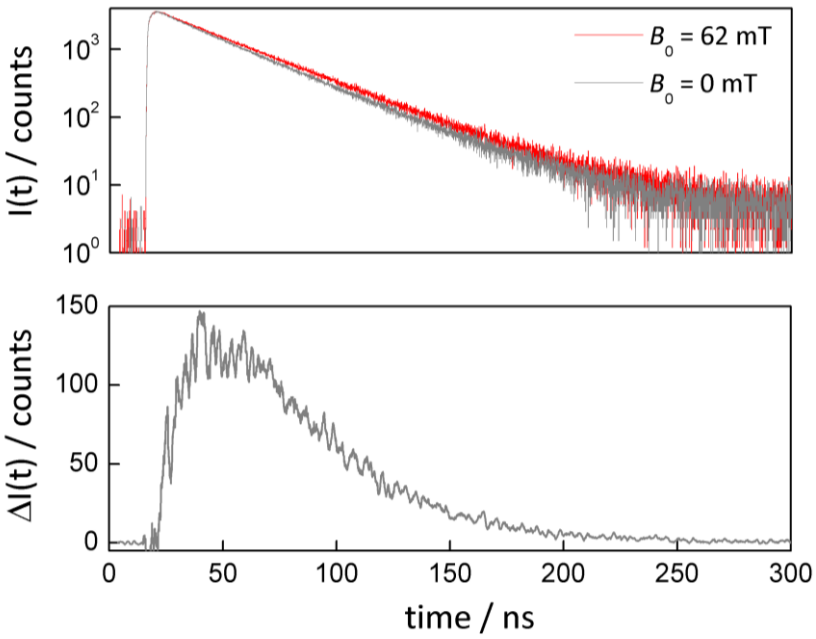

(a) Mant-8-O-2-DMA exciplex

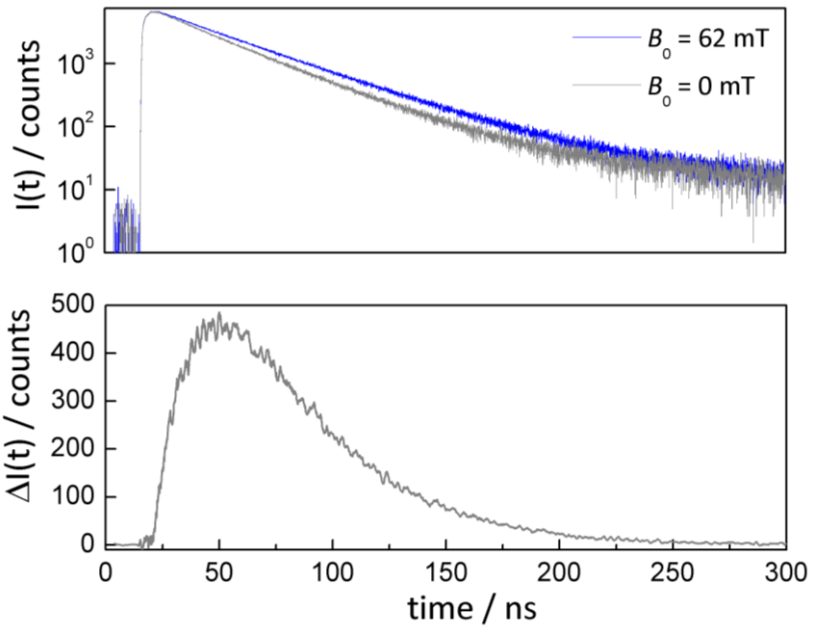

(b) Mant-10-O-2-DMA exciplex

Figure A4. Upper panels of (a) and (b): The exciplex emission decays of the Mant-8-O-2-DMA (2.10^{-5} M) and Mant-10-O-2-DMA (2.10^{-5} M) in the absence and presence of an external magnetic field, respectively. Lower panels of (a) and (b): Time-resolved magnetic field effects of the exciplexes extracted from the experimental data (gray lines). Neat butyronitrile (ε_s = 24.7) used as a solvent.

A5. Formulation of the exciplex dissociation quantum yield, ϕ_d

The exciplex lifetime is a function of static dielectric constant, ε_s:

$$\tau_E(\varepsilon_s) = \frac{1}{k_r + k_{nr} + k_d(\varepsilon_s)} \tag{A.1}$$

Here k_r, k_{nr} are the rate constants of the radiative and non-radiative exciplex decays, respectively. k_d gives the exciplex dissociation rate constant.

At $\varepsilon_s = 6$, under the assumption that there is no exciplex dissociation, i.e., $k_d = 0$.

Introducing $k_d = 0$ in eq. (A.1) yields

$$k_r + k_{nr} = \frac{1}{\tau_E(\varepsilon_s = 6)} = const \tag{A.2}$$

From eq. (A.1) and eq. (A.2), we can calculate k_d through:

$$k_d(\varepsilon_s) = \frac{1}{\tau_E(\varepsilon_s)} - \frac{1}{\tau_E(\varepsilon_s = 6)} \tag{A.3}$$

The exciplex dissociation quantum yield is defined by:

$$\phi_d(\varepsilon_s) = \frac{k_d(\varepsilon_s)}{k_d(\varepsilon_s) + k_r + k_{nr}} \tag{A.4}$$

Introducing eq. (A.3) in eq. (A.4) yields

$$\phi_d(\varepsilon_s) = k_d(\varepsilon_s).\tau_E(\varepsilon_s) \tag{A.5}$$

ACRONYMS

Solvents

ACN : acetonitrile
BN : butyronitrile
EtCN : propionitrile
PA : propyl acetate

Substances

Ant : anthracence
DEA : *N*,*N*-diethylaniline
DMA : *N*,*N*-dimethylaniline
DMAnt : 9,10-dimethylanthracene
DMAPE : 2-[(4-dimethylamino)phenyl]ethanol
MAnt : 9-methylanthracene
1,6-DBH : 1,6-dibromohexane
1,8-DBO : 1,8-dibromooctane
1,10-DBD : 1,10-dibromodecane
1,16-HDDO : 1,16-hexadecanediol
1,16-DBHD : 1,16- dibromohexadecane
Mant-6-Br : 1-bromo-6-[9-(10-methyl)anthryl]hexane
Mant-8-Br : 1-bromo-8-[9-(10-methyl)anthryl]octane
Mant-10-Br : 1-bromo-10-[9-(10-methyl)anthryl]decane
Mant-16-Br : 1-bromo-16-[9-(10-methyl)anthryl]hexadecane
Mant-6-O-2-DMA : 2-[4-(dimethylamino)phenyl]ethyl 6-[9-(10-methyl)anthryl]hexyl ether
Mant-8-O-2-DMA : 2-[4-(dimethylamino)phenyl]ethyl 8-[9-(10-methyl)anthryl]octyl ether
Mant-10-O-2-DMA : 2-[4-(dimethylamino)phenyl]ethyl 10-[9-(10-methyl)anthryl]decyl ether
Mant-16-O-2-DMA : 2-[4-(dimethylamino)phenyl]ethyl 16-[9-(10-methyl)anthryl]hexadecyl ether

Others

A : acceptor

D : donor

ET : electron transfer

GS : ground state

HFI : hyperfine interaction

LE : locally excited

LIP : loose ion pair

MFE : magnetic field effect

PET : photo-induced electron transfer

P : product

R : reactant

RIP : radical ion pair

S : singlet

SRIP : singlet radical ion pair

SS : steady-state

T : triplet

TCSPC : time-correlated single photon-counting

TR : time-resolved

TR-MFE : time-resolved magnetic field effect

REFERENCES

[1] R. A. Marcus, *J. Chem. Phys.*, 1956, **24**, 966-978.

[2] R. A. Marcus, *J. Chem. Phys.*, 1957, **26**, 867-871.

[3] R. A. Marcus and N. Sutin, *Biochim. Biophys. Acta BBA - Rev. Bioenerg.*, 1985, **811**, 265–322.

[4] P. Siders and R. A. Marcus, *J. Am. Chem. Soc.*, 1981, **103**, 748–752.

[5] O. F. Mohammed, K. Adamczyk, N. Banerji, J. Dreyer, B. Lang, E. T. J. Nibbering, and E. Vauthey, *Angew. Chem. Int. Ed.*, 2008, **47**, 9044–9048.

[6] T. Inada, K. Kikuchi, Y. Takahashi, H. Ikeda, and T. Miyashi, *J. Phys. Chem. A*, 2002, **106**, 4345–4349.

[7] K. Kikuchi, T. Niwa, Y. Takahashi, H. Ikeda, T. Miyashi, and M. Hoshi, *Chem. Phys. Lett.*, 1990, **173**, 421–424.

[8] K. Kikuchi, *J. Photochem. Photobiol. Chem.*, 1992, **65**, 149–156.

[9] H. Miyasaka, S. Ojima, and N. Mataga, *J. Phys. Chem.*, 1989, **93**, 3380–3382.

[10] M. Koch, R. Letrun, and E. Vauthey, *J. Am. Chem. Soc.*, 2014, **136**, 4066–4074.

[11] Man Him Hui and W. R. Ware, *J. Am. Chem. Soc.*, 1976, **98**, 4718–4727.

[12] P. Van Haver, N. Helsen, S. Depaemelaere, M. Van der Auweraer, and F. C. De Schryver, *J. Am. Chem. Soc.*, 1991, **113**, 6849–6857.

[13] H. Leonhardt and A. Weller, *Ber. Bunsen-Ges. Phys. Chem.*, 1963, **76**, 791-795.

[14] S. Murata and M. Tachiya, *J. Phys. Chem. A*, 2007, **111**, 9240–9248.

[15] N. Mataga, *Pure Appl. Chem.*, 1984, **56**, 1255–1268.

[16] E. Vauthey, *J. Photochem. Photobiol. Chem.*, 2006, **179**, 1–12.

[17] V. S. Gladkikh, A. I. Burshtein, H. L. Tavernier, and M. D. Fayer, *J. Phys. Chem. A*, 2002, **106**, 6982–6990.

[18] S. Murata and M. Tachiya, *J. Phys. Chem.*, 1996, **100**, 4064–4070.

[19] P.-A. Muller, C. Högemann, X. Allonas, P. Jacques, and E. Vauthey, *Chem. Phys. Lett.*, 2000, **326**, 321–327.

[20] A. Rosspeintner, D. R. Kattnig, G. Angulo, S. Landgraf, G. Grampp, and A. Cuetos, *Chem. - Eur. J.*, 2007, **13**, 6474–6483.

[21] A. Rosspeintner, D. R. Kattnig, G. Angulo, S. Landgraf, and G. Grampp, *Chem. - Eur. J.*, 2008, **14**, 6213–6221.

[22] J. Zhou, R. P. Shah, B. R. Findley, and C. L. Braun, *J. Phys. Chem. A*, 2002, **106**, 12–20.

[23] I. R. Gould, R. H. Young, L. J. Mueller, and S. Farid, *J. Am. Chem. Soc.*, 1994, **116**, 8176–8187.

[24] K. Kikuchi, Y. Takahashi, M. Hoshi, T. Niwa, T. Katagiri, and T. Miyashi, *J. Phys. Chem.*, 1991, **95**, 2378–2381.

[25] T. Sengupta, S. Dutta Choudhury, and S. Basu, *J. Am. Chem. Soc.*, 2004, **126**, 10589–10593.

[26] K. B. Henbest, P. Kukura, C. T. Rodgers, P. J. Hore, and C. R. Timmel, *J. Am. Chem. Soc.*, 2004, **126**, 8102–8103.

[27] C. T. Rodgers, S. A. Norman, K. B. Henbest, C. R. Timmel, and P. J. Hore, *J. Am. Chem. Soc.*, 2007, **129**, 6746–6755.

[28] M. Justinek, G. Grampp, S. Landgraf, P. J. Hore, and N. N. Lukzen, *J. Am. Chem. Soc.*, 2004, **126**, 5635–5646.

[29] N. N. Lukzen, D. R. Kattnig, and G. Grampp, *Chem. Phys. Lett.*, 2005, **413**, 118–122.

[30] K. Pal, G. Grampp, and D. R. Kattnig, *ChemPhysChem*, 2013, **14**, 3389–3399.

[31] K. Pal, D. R. Kattnig, G. Grampp, and S. Landgraf, *Phys. Chem. Chem. Phys.*, 2012, **14**, 3155-3161.

[32] S. Aich and S. Basu, *J. Phys. Chem. A*, 1998, **102**, 722–729.

[33] U. Werner and H. Staerk, *J. Phys. Chem.*, 1995, **99**, 248–254.

[34] D. R. Kattnig, A. Rosspeintner, and G. Grampp, *Angew. Chem. Int. Ed.*, 2008, **47**, 960–962.

[35] D. R. Kattnig, A. Rosspeintner, and G. Grampp, *Phys. Chem. Chem. Phys.*, 2011, **13**, 3446-3460.

[36] S. Richert, A. Rosspeintner, S. Landgraf, G. Grampp, E. Vauthey, and D. R. Kattnig, *J. Am. Chem. Soc.*, 2013, **135**, 15144–15152.

[37] S. Basu, D. N. Nath, M. Chowdhury, *Chem. Phys. Lett.*, 1989, **161**, 449-454.

[38] D. N. Nath, S. Basu, and M. Chowdhury, *J. Chem. Phys.*, 1989, **91**, 5857-5859.

[39] A. Weller, H. Staerk, and R. Treichel, *Faraday Discuss. Chem. Soc.*, 1984, **78**, 271-278.

[40] M. K. Crawford, Y. Wang and K. B. Eisenthal, *Chem. Phys. Lett.*, 1981, **79**, 529-533.

[41] Y. Wang, M. C. Crawford, and K. B. Eisenthal, *J. Am. Chem. Soc.*, 1982, **104**, 5874–5878.

[42] X.-J. Luo, G. S. Beddard, G. Porter, R. S. Davidson, and T. D. Whelan, *J. Chem. Soc. Faraday Trans. 1 Phys. Chem. Condens. Phases*, 1982, **78**, 3467-3476.

[43] H. Cao, K. Miyata, T. Tamura, Y. Fujiwara, A. Katsuki, C.-H. Tung, and Y. Tanimoto, *J. Phys. Chem. A*, 1997, **101**, 407–411.

[44] Y. Tanimoto, N. Okada, M. Itoh, K. Iwai, K. Sugioka, F. Takemura, R.i Nakagaki, and S. Nagakura, *Chem. Phys. Lett*, 1987, **136**, 42-74.

[45] H. Cao, Y. Fujiwara, T. Haino, Y. Fukazawa, C-H. Tung, and Y. Tanimoto, *Bull. Chem. Soc. Jpn*, 1996, **69**, 2801-2813.

[46] S. Arrhenius, *Zeit. physikal. Chem*, 1889, **4**, 226–48.

[47] H. M. Rosenstock, M. B. Wallenstein, A. L. Wahrhaftig, H. Eyring, *Proc. Natl. Acad. Sci. U. S. A*, 1952, **38**, 667–78.

[48] J. C. Giddings, H. Eyring, H, *J. Chem. Phys*, 1954, **22**, 538–42.

[49] D. G. Truhlar, B. C. Garrett, and S. J. Klippenstein, *J. Phys. Chem.*, 1996, **100**, 12771–12800.

[50] N. Sutin, *Acc. Chem. Res*, 1982, **15**, 275–282.

[51] K. J. Laidler, *Chemical Kinetics*. 3rd ed; Prentice Hall, 1987; Vol. 3rd, p 531.

[52] A. Mansha, PhD thesis, Graz University of Technology, 2009.

[53] T. X. Nguyen, PhD thesis, Graz University of Technology, 2011.

[54] A. Rosspeintner, PhD thesis, Graz University of Technology, 2008.

[55] G. J. Kavarnos, *Fundamentals of Photoinduced Electron Transfer*; VCH Publishers: New York, NY, 1993.

[56] R. A. Marcus, *J. Chem. Phys.*, 1965, **43**, 679-701.

[57] R. A. Marcus, *J. Chem. Phys.*, 1956, **24**, 979-989.

[58] G. L. Closs, L. T. Calcaterra, N. J. Green, K. W. Penfield, and J. R. Miller, *J. Phys. Chem.*, 1986, **90**, 3673–3683.

[59] E. Vauthey, *J. Phys. Chem. A*, 2001, **105**, 340–348.

[60] M. R. Wasielewski, M. P. Niemczyk, W. A. Svec, and E. B. Pewitt, *J. Am. Chem. Soc.*, 1985, **107**, 1080–1082.

[61] N. Mataga, Y. Kanda, and T. Okada, *J. Phys. Chem.*, 1986, **90**, 3880–3882.

[62] R. A. Marcus, *Disc. Faraday Soc*, 1960, **29**, 21-31.

[63] M. Justinek, PhD thesis, Graz University of Technology, 2003.

[64] H. Hayashi, *Introduction to dynamic spin chemistry: magnetic field effects on chemical and biochemical reactions*, World Scientific, River Edge, N.J, 2004.

[65] H. Staerk, W. Kühnle, R. Treichel, A. Weller, *Chem. Phys. Lett*. 1985, **118**, 19-24.

[66] J. R. Lakowicz, *Principles of fluorescence spectroscopy*, Springer, New York, 3rd ed., 2006.

[67] M. Montalti and S. L. Murov, Eds., *Handbook of photochemistry*, CRC/Taylor & Francis, Boca Raton, 3rd ed., 2006.

[68] D. Mosnaim, D.C. Nonhebel, J.A. Russell, *Tetrahedron*, 1969, **25**, 3485-3492.

[69] S. Franceschi, V. Andreu, N. de Viguerie, M. Riviere, A. Lattes, and A. Moisand, *New J. Chem.*, 1998, **22**, 225–231.

[70] J. A. Riddick, *Organic solvents: physical properties and methods of purification*, Wiley, New York, 4th ed., 1986.

[71] M. G. Kuzmin, I. V. Soboleva, and E. V. Dolotova, *J. Phys. Chem. A*, 2007, **111**, 206–215.

[72] J. Bolton, A. Carrington, A. McLachlan, *Mol. Phys*, 1962, **5**, 31-41.

[73] F. Gerson, W. Huber, *Electron Spin Resonance Spectroscopy for Organic Radicals*, 1st ed.; Wiley-VCH, 2001.

[74] V. R. Gorelik, E. G. Bagryanskaya, N. N. Lukzen, I. V. Koptyug, V. V. Perov, and R. Z. Sagdeev, *J. Phys. Chem.*, 1996, **100**, 5800–5807.

[75] S. F. Swallen, K. Weidemaier, and M. D. Fayer, *J. Chem. Phys.*, 1996, **104**, 2976.

[76] U. E. Steiner and T. Ulrich, *Chem. Rev.*, 1989, **89**, 51–147.

[77] P. Suppan, *J. Chem. Soc. Faraday Trans. 1 Phys. Chem. Condens. Phases*, 1987, **83**, 495-509.

[78] P. Suppan, *J. Photochem. Photobiol. A*, 1990, **50**, 293-330.

[79] Y. Tanimoto, K. Hasegawa, N. Okada, M. Itoh, K. Iwai, K. Sugioka, F. Takemura, R. Nakagaki, and S. Nagakura, *J. Phys. Chem.*, 1989, **93**, 3586–3594.

[80] H. Lee, N. Yang, and A. E. Cohen, *Nano Lett.*, 2011, **11**, 5367–5372.

[81] Y. Tanimoto, M. Takashima, and M. Itoh, *Bull. Chem. Soc. Jpn.*, 1989, **62**, 3923-3931.

[82] A. Weller, F. Nolting, and H. Staerk, *Chem. Phys. Lett.*, 1983, **96**, 24–27.

[83] A. I. Shushin, *Chem. Phys. Lett.*, 1991, **181**, 274–278.

[84] J. B. Birks in Photophysics of Aromatic Molecules (Ed.: J. B. Birks),Wiley-Interscience, London, 1970 (Wiley Monographs in Chemical Physics).

[85] N. K. Petrov, A. Wiessner, T. Fiebig, and H. Staerk, *Chem. Phys. Lett.*, 1995, **241**, 127–132.

[86] N. K. Petrov, *High Energy Chem.*, 2006, **40**, 22–34.

[87] R. A. Marcus, *Annu. Rev. Phys. Chem.*, 1964, **15**, 155–196.

[88] N. Sutin, *J. Photochem.*, 1979, **10**, 19–40.